UNIVERSITÀ DEGLI STUDI DI MILANO

DOTTORATO IN SCIENZE MATEMATICHE

DIPARTIMENTO DI MATEMATICA “FEDERIGO ENRIQUES”

CORSO DI DOTTORATO IN MATEMATICA XXIX CICLO

TESI DI DOTTORATO DI RICERCA

THE FIRST 3D MODEL OF THE OLFACTORY BULB: A STUDY ON ODOR LEARNING AND REPRESENTATION

MAT/08

PHD CANDIDATE
FRANCESCO CAVARRETTA

ADVISOR
PROF. GIOVANNI NALDI

COORDINATOR
PROF. VIERI MASTROPIETRO

A.A. 2016/17

Dedicated to my parents,
Gaspare and Maria Carmela

Li guai dintra a la pignata, li sapi sulu la cucchiara chi l'arrimina.

I guai dentro a una pentola, li conosce soltanto la paletta che li agita.

Troubles of a boiling pot are only known by the spoon which stirs them

Ancient sicilian proverb

Acknowledgements

In this part, I would like to thank some people. First, I am very grateful to Jesus for everything has happened during this period, and especially for healing my father. I would like to thank my parents, Gaspare and Maria Carmela, who continously have encouraged me throughout my life; thanks to my brother and his wife, Isidoro and Rosaria, together with my screaming niece, Alice, for asking for a gift everytime I had a Skype call with her. Thanks to my oldest friend, frate Mariano Russo, who prayed for me and my family at the Holy Land. Thanks to don Francesco Contadini who is watching me from the heaven. Thanks to Ciro Lomonte, who has been a true friend during a very crucial moment of my life.

Thanks to my wonderful friends at the University of Milan: Matteo Burzoni, Lara Charawi, Alberto Cogliati, Roberta Dalceri, Luca Magri, whose great smiles are not easy to forget though the long distance that now separates us. Thanks to such an old friend, Luca Torrisi, who makes me laugh by recounting many funny facts. Thanks to my girlfriend, Poornima Herath, who helped me so much and happily with editing.

It is also worth mentioning my time in Palermo. Thanks to everybody I met in the Residenza Segesta, and all my professors of the Universit degli Studi di Palermo. Thanks to Dr. Michele Migliore, who has been advising me since the time of my bachelor degree. Thanks to the Shepherd's lab crew; thanks to prof. Gordon M. Shepherd who illuminated us through his advise, and Dr. Michael Hines who has

advised the development of the olfactory bulb model. Finally, but not to be forgotten, special thanks are deserved to prof. Giovanni Naldi who is so open mind to let me visiting Yale for such a long time.

Abstract

How the olfactory bulb processes odor input cannot be easily addressed using standard experimental techniques, therefore we have developed a large scale model of olfactory bulb, using realistic three-dimensional inputs, cell morphologies of mitral and granule cells, and connectivity. The model makes experimentally testable prediction, providing a powerful framework for investigating the olfactory bulb computations, such as the odor learning and representation.

By the odor learning, the olfactory bulb organizes itself in synaptic columnar clusters related to individual glomeruli, called glomerular units. Using our 3D model, we identify the mechanisms for forming one or more glomerular units in response to a given odor, how and to what extent the glomerular units interfere or interact with each other during learning.

Together, we have analyzed how the olfactory bulb processes inputs from olfactory receptor neurons activated by natural odors. This is realized through two computational tiers: the glomerular layer at the site of input, and the granule cell level at the site of output to the olfactory cortex. We suggest that the postulated functions of glomerular circuits have as their primary role transforming a complex and disorganized input into a contrast-enhanced and normalized representation, but cannot provide for synchronization of the distributed glomerular outputs. By contrast, at the granule cell layer, the dendrodendritic interactions mediate temporal decorrelation, which we show is dependent on the preceding contrast enhancement by the

glomerular layer. The results provide the first insights into the successive operations in the olfactory bulb, and demonstrate the significance of the modular organization around glomeruli. This layered organization is especially important for natural odor inputs, because they activate many overlapping glomeruli.

Abstract

Le attuali tecniche sperimentali non permettono di studiare come il bulbo olfattivo processa gli odori, quindi ne abbiamo sviluppato un modello tridimensionale su larga scala. Questi riproduce in maniera realistica gli stimoli dovuti alla presenza di odori naturali, le morfologie di cellule mitrali e granulari, insieme alla loro connettivit. Il nostro modello ritorna predizioni che sono sperimentalmente verificabili, fornendo un potente strumento per lo studio delle computazioni del bulbo olfattivo, quali ad esempio l'apprendimento e la rappresentazione degli odori. Con l'apprendimento di un odore, il bulbo olfattivo si auto-organizza in gruppi di colonne, ciascuna in corrispondenza di un singolo glomerulo o unit glomerulare. Usando il nostro modello, abbiamo identificato i meccanismi su cui si basa la formazione di una o pi colonne/unit glomerulari in seguito alla presentazione di un odore. In aggiunta, abbiamo esaminato come le interazioni fra unit glomerulari durante l'apprendimento possono influenzare la configurazione finale delle colonne. In seguito, abbiamo studiato come il bulbo olfattivo elabora gli ingressi provenienti dai recettori olfattivi attivati dagli odori naturali. Questo avviene su due livelli computazionali: lo strato glomerulare al livello di input, e lo strato delle cellule granulari al livello di output verso la corteccia olfattiva. Ci suggerisce che le funzioni postulate nei circuiti glomerulari hanno come ruolo primario la trasformazione di un input complesso e disorganizzato in una rappresentazione dove i livelli di attivazione sono normalizzati, e il loro contrasto intensificato. Tuttavia loutput del livello glomeru-

lare non pu sincronizzare lattivit dei glomerulari. Pertanto, a livello delle cellule granulari, le interazioni dendrodendritiche inducono una decorrelazione temporale dei pattern rappresentativi dei vari odori, a sua volta dipendente da quella precedentemente realizzata nel livello glomerulare. Questi risultati forniscono importanti indizi riguardanti la computazione/rappresentazione del bulbo olfattivo, dimostrando l'importanza della sua auto-organizzazione modulare in unit glomerulari. La sua organizzazione a strati particolarmente importante per la rappresentazione degli odori naturali, dal momento che le aree da essi attivate sulla superficie del bubo sono sovrapposte.

List of Contributors

- Francesco Cavarretta
  Universita degli Studi di Milano, Milano, Italy e-mail: francescocavarretta@hotmail.it
- prof. Giovanni Naldi
  Universita degli Studi di Milano, Milano, Italy e-mail: giovanni.naldi@unimi.it
- prof. Gordon Shepherd
  Yale Department of Neuroscience, New Haven, CT, USA e-mail: gordon.shepherd@yale.edu
- Dr. Michele Migliore
  Consiglio Nazionale delle Ricerche, Palermo, Italy e-mail: michele.migliore@cnr.it

Contents

Acronyms

AOB	Anterior olfactory bulb
CE	Constrast Enhancement
dSAC	Deep short axon cell
EPL	External plexiform layer
eTC	External tufted cell
GC	Granule cell
GCL	Granule cell layer
GL	Glomerular layer
GU	Glomerular Unit
IPL	Internal plexiform layer
iTC	Interior tufted cell
LOT	Lateral olfactory tract
MC	Mitral cell
MCL	Mitral cell body layer
MOB	Main olfactory bulb
M/T	Mitral and tufted cell
mTC	Middle tufted cell
OB	Olfactory bulb
OC	Olfactory cortex
ODE	Ordinary Differential Equation

OE	Olfactory epithelium
ON	Olfactory nerve
ORN	Olfactory receptor neuron
PG	Periglomerular cell
PRV	pseudorabies virus
SA	Short axon cell
SVZ	Subventricular zone
TC	Tufted cell
VNO	Vomeronasal organ

Introduction

The olfactory bulb is a small self-contained neural system that realizes several important mechanisms for odor discrimination. It is located between the olfactory epithelium and the olfactory cortex, which respectively implement the outermost and innermost computational tiers of the odor signal pathway.

The odor signal pathway is therefore straightforward, so as the internal organization of the olfactory bulb, which nevertheless does not perform a naive computation. Bear in mind that the dynamics underlying a single neuron functioning are highly non-linear, then extremely difficult to understand, so they make even more intricate to investigate an entire neural system. This is true even in the olfactory bulb, of which computation is orchestrated by millions of tiny interneurons that interconnect its computational units (i.e. glomerular unit). In fact, the available models of olfactory bulb are not able to explain how it works, thus its coding mechanism remain still poorly understood. On the one hand, the current models appear to be too abstract in explaining the olfactory bulb behavior, and ignore many fundamental physiological mechanisms that are instead explored in experimental works. On the other hand, a number of technical limitations in carrying out experimental investigations makes it difficult to study the basic cellular mechanisms of odor recognition. A theoretical model fully constrained to experimental findings will be increasingly helpful to override the typical technical issues of experimental protocols, since it could be analyzed instead of the real system. The realistic neuron simulation fullfills

this goal, whereby the returned numerical results perfectly match the real behaviour of nervous systems.

The NEURON simulation environment [24] is the most popular and advanced engine for realistic neuron simulation. Here, neuron morphology are reproduced with the full dendritic tree in a virtual 3D space, with its real spatial extent and arborization, whereas the passive and active membrane properties are simulated by solving the Hodgkin-Huxley model [5]. The Hodgkin-Huxley model in particular reproduces the real action potential, together its propagation through the dendritic tree. Thus, taking into account its characteristics, we have built a 3D realistic large scale model of the olfactory bulb [38] based on NEURON. This itself is the first model of its genre, which has been used to carry out all predictions shown in the present thesis.

The thesis is organized as follows:

- Chapter 1: a description of the anatomy of olfactory bulb, especially of its structure, connectivity, and neuron populations;
- Chapter 2: a short discussion around the experimental findings showing the olfactory bulb is organized in columnar computational units;
- Chapter 3: a description of the basic electrophysiological and modelistic concepts that form the basis for realistic neuron simulation;
- Chapter 4: a description of the first realistic large scale 3D model of the olfactory bulb;
- Chapter 5: the first study performed by our 3D model of olfactory bulb, in which we have investigated the relation between column formation and odor learning;
- Chapter 6: a study about the reciprocal inter-glomerular interaction, so as the firing pattern that such interaction sculpts on mitral cells;
- Chapter 7: the analysis of the olfactory bulb computation, which aimed to understand the role of the glomerular and granule cell layers.

We thus aimed to understand how the olfactory bulb works, and the organizational patterns that are behind its functioning. These may be used to perform futher comparative studies across other brain areas. In addition, since the olfactory bulb is

one of the oldest region out of the nervous system, understanding its internal organization may be also helpful to unravel the evolutionary logic that stands behind the nervous system.

However, understanding the olfactory bulb may not remain confined to a biological domain, the mechanisms used by the olfactory bulb, to efficiently discriminate and categorize odors, are modeled and understood, they could be exploited in the industrial and ITC fields to design, for example, new and more efficient algorithms for data mining and clustering, to propose new neural networks. Whereas a robotic olfactory bulb could be implemented, with industrial applications to develop sensors for ”natural” odors or prostheses for individuals that have lost the smell sensibility.

Part I

The anatomy of the olfactory bulb

Chapter 1

The anatomy of the olfactory bulb

In this chapter, we introduce the basics of the olfactory bulb organization, describing its structure, neuron populations, and connectivity. Most of the content in this chapter is summarized from *"The Synaptic Organization of the Brain"* (G.M. Shepherd, [4]), enriched with some recent experimental findings.

In case the reader is well acquainted of olfactory bulb, we reccommend to skip reading this chapter.

1.1 The structure

The OB is a small self-contained neural system located inside the braincase (Fig. 1.1A). It performs several important functions for odor discrimination. The OB receives input and sends output through two different bundles of axons; they are the ON and the LOT, respectively. The ON is a fasciculation of ORNs axons, while the LOT is the axonal tree that belongs to M/Ts.

The ORNs are randomly scattered on the OE surface, where they are directly in touch with the external environment. On one hand, each ORN performs a transduction of odor molecules into action potentials. Thus, ORN activities carry out the first odor representation within the olfactory system, likely as a firing rate code. On the other hand, the OC constitutes the last computational tier of the olfactory system, whereby one operates the odor recognition. This is the main task of the olfactory

system. Taking into account the position of the OB in the odor signal pathway, it can be seen as a gate between OE and OC.

There are two identical OBs, each belongs to an individual brain hemisphere. The shape of each OB can be approximated by ellipsoid of 2-3 mm in axis, where neurons are arranged in several layers (Fig. 1.1B). These layers are the GL (150 μm thick, Fig. 1.1B, blue layer), the EPL (400 μm thick, Fig. 1.1B, red layer), and the GCL (400 μm thick, Fig. 1.1B, green layer), from the outermost to the innermost. Here, the largest neuron populations are MCs, TCs, and GCs; MCs and TCs lie on EPL whereas GCs occupy the GCL space (Fig. 1.1B).

Moreover, the OB concerns two subparts that are the MOB and the AOB. Both have basically the same connectivity and neuron populations, whereas only difference between MOB and AOB concerns a few minor details in the translaminar connectivity. The MOB and AOB receive input from the OE and the VNO, respectively, thus they are sensitive to different odor types. Particularly, the AOB is mostly pheromone-sensitive, while the MOB is responsive to a wider variety of odor molecules. In addition, their own principal neurons project to different cortical regions that are the OC and the amygdala, respectively. However, such a difference between AOB and MOB is not precisely determinable. For example, pheromone-sensitive glomeruli have been discovered on the MOB surface, of which M/Ts project to the amygdala.

In this thesis, we have only been investigating the MOB. This has been interesting since the MOB makes a larger contribution to the higher level functions related to the odor recognition.

1.2 The connectivity

The olfactory system is structured in three computational tiers that are the OE, the OB, and the OC (Fig. 1.2). The odor information goes through these three tiers,

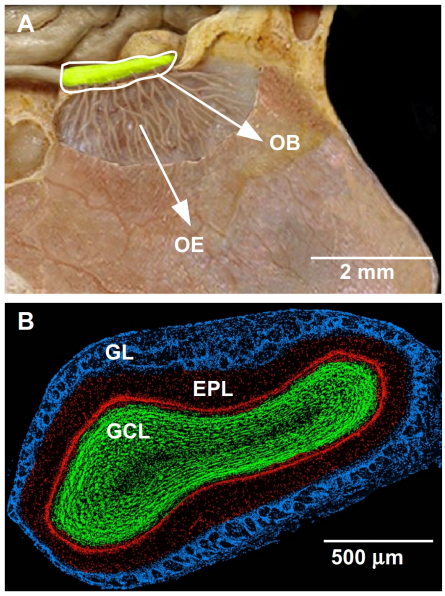

Fig. 1.1 (A) The position of the olfactory olfactory and (B) the coronal view of the main olfactory bulb.

propagating thus from the outermost to the innermost ones. Accordingly, even the odor learning may occur through these three tiers in the same order.

The OE is randomly endowed by ORNs. Each ORN owns a single odor receptor, which binds with specific subtypes of odor molecules. The binding evokes the ORN response in form of tonic firing, of which rate is graded with concentration of odor. Therefore, ORNs are in different subtypes, each is sensitive to specific subgroups of odor molecules (i.e. odor phenotype). Those ORN axons which belong to a given odor phenotype convey into a spherical structure of neuropil, called glomerulus.

All glomeruli form the outermost layer of the OB, in which it is conveyed the excitatory input produced by the ORNs. Within the glomerulus, the ORN axons release glutamate on tuft dendrites of PG and M/T, activating AMPA and NMDA receptors on their membrane. At the same time, glomeruli are surrounded by PGs. These neurons mediate GABAergic inhibition on M/T tuft dendrites. The PGs, together with superficial-axon and external tufted cells constitute the juxtglomerular circuit, where the PGs are the output. The juxtglomerular circuit modulates the ex-

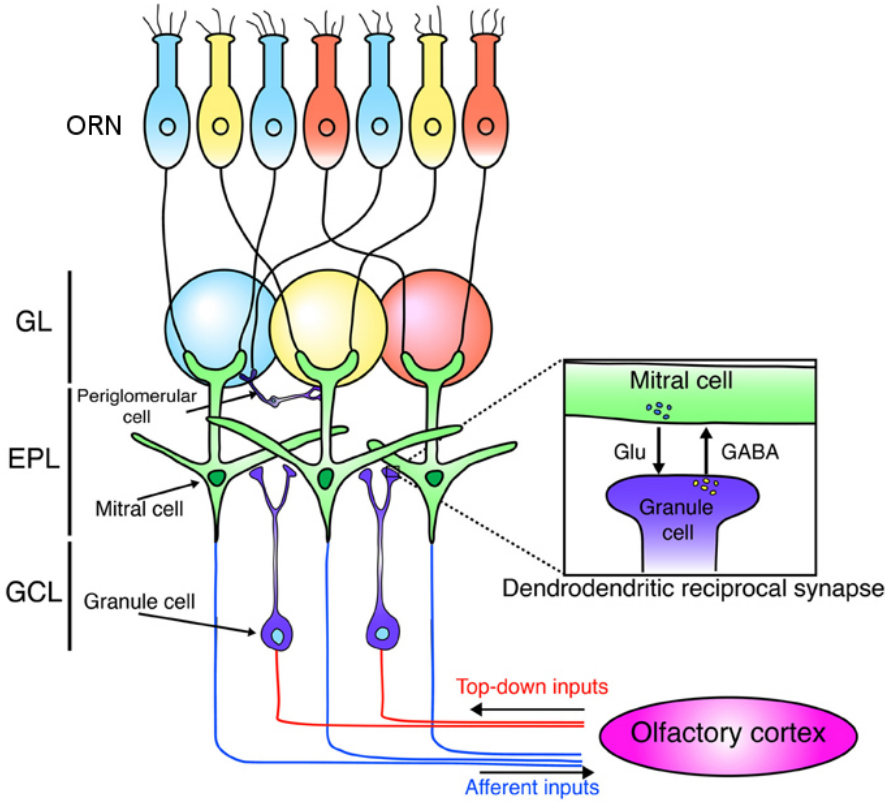

Fig. 1.2 Neurons and connectivity of the olfactory bulb.

citatory activities induced by ORNs. Without PGs, the M/T activity would merely driven by ORNs.

Subsequently, the excitation resulting within a glomerulus grades the intensity of M/T response. The M/T apical dendrites traverse the EPL, where they neither bifurcate nor receive any synaptic afference. Thus, M/T apical dendrites basically pass the excitation odor representation occurring in the GL to the M/T cell bodies.

Several lateral dendrites arise from the M/T bodies, ramifying in 6-7 levels inside the EPL. Here, they make a larg a large number of reciprocal dendrodendritic synapses (Fig. 1.2, inset) with tiny interneurons, called GCs. The M/T-to-GC synapse release glutamate, activating AMPA and NMDA receptors on the GC tuft dendrite, whereas GCs releases $GABA_B$ on M/T lateral dendrite as feedback re-

sponse. Such a peculiar type of synapse occurs robustly across EPL. The reciprocal synapses are in fact 80% of total, whereas the remaining 20% are due to inhibitory synapses between dSACs and GCs.

The M/Ts in turn produce the output of the OB, which is sent to the OC through the M/T axonal projections. The inhibition plays the most relevant role in orchestrating the overall activity of the OB. Therefore, the GCs finely sculpt the OB output by rhythmic inhibition released on the M/T dendrites.

Those action potentials that are fired by an M/T, after backpropagating through its lateral dendrites, evoke the GC responses which in turn inhibit all M/Ts to which they are connected. By this mechanism, M/Ts that belong to different glomeruli can inhibit each other (i.e. lateral inhibition).

The inhibition induced by the GCs can be decomposed in two components that self and lateral -inhibitions. First one is induced from a glomerulus on itself through its own GCs. Second one is instead due to the activity of surrounding glomeruli, which is thus transmitted through shared subsets of GCs. Both self and lateral -inhibition have been reproduced by realistic computer simulations; these results are shown in the last chapters.

1.3 The Neuron Populations

1.3.1 The Olfactory Receptor Neurons

The ORNs form a morphologically homogeneous population that randomly endows the OE surface. This makes the outermost level of the olfactory system that thus interacts with the external environment.

Each ORN is a small and simple neuron formed by a soma, a single thin apical dendrite, and an axon. The soma is 10 μm in diameter, both apical dendrite and axon arise from it, and their diameter taper and range between 0.1 and 0.4 μm. The axon perforates the OE, terminating into a glomerulus, where it makes synapse

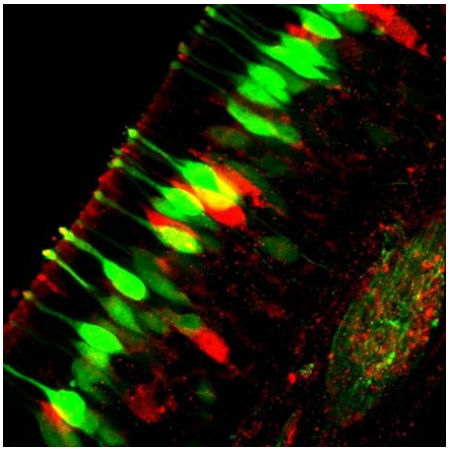

Fig. 1.3 Olfactory receptor neurons of mouse, colored by different odor markers, one for each odor phenotype.

with either M/T or PG. Inversely, the apical dendrite projects into a knob situated in the OE, which holds a metabotropic ligand gate channel (i.e. odor receptor) on its terminal that can bind with only a subtype of odor molecules. The binding triggers the ORN response that occurs therefore selectively. The odor phenotypes are coded into 1,000 different types by a large multigene family and are coded [110], therefore ORNs express the most diversified phenotype out of the nervous system.

Despite of the phenotype, ORNs are arranged on OE randomly, though all axons of the same phenotype converge exclusively into two glomeruli in the medial and lateral OB. Yet, it is not clear whether and how both glomeruli are related to each other in odor coding, but experimental findings suggest that they may realize a temporal code reliable for the odor concentration through reciprocal interactions [112].

Moreover, ORNs undergo to neurogenesis, so that each is periodically replaced by basal cell located in the OE. After the basal cell becomes a mature ORN, this tightly keeps the same odor phenotype and glomerular target of replaced ORN.

Such high dynamicity, the strict specificity in response, and the highly variegated phenotype, make ORNs the unique case out of the nervous system.

1.3.2 Glomeruli

The glomeruli are spherical neuropils of 30-50 μm in diameter and sharp borders. They form the outermost layer of the OB. Every glomerulus collects exclusively the ORN axons expressing a single odor phenotype, which make excitatory synapses with tuft dendrites of M/T and PG.

1.3.3 Periglomerular cells

The PGs are located in the GL, where they surround the glomeruli.

A PG is formed by a soma, a few short dendrites, and a single axon. The soma is 6-8 μm in diameter, from which arise both axon and dendrites. The dendrites arborize within one or more glomeruli, depending on the PG subtype, where they extend 50-100 μm. The axon projects laterally as far as 5 glomeruli. Some PGs appear to be axonless, but such absence is suspected to be due to a fail in the staining method, rather than a real lack.

PGs are still inclosed in much uncertainty. For example, it is not know in how many different subtypes the PG can be classified. Very peculiarly, although the GABA is deemed to be inhibitory, it can have an excitatory effect on PGs [116].

1.3.4 Mitral cells

MCs and TCs work in tandem to carry out the second order representation of odor. They form two parallel distinct signal pathways.

An MC is formed by a soma, a single apical dendrite, several lateral dendrites, and a huge axonal tree. The cell body is 15-30 μm in diameter. The apical dendrite traverses the EPL, terminating within a glomerulus, where it branches in 6-7 levels of tuft dendrites. The tuft dendrites form a tangle that is 30-150 μm in diameter, which is extended through the most part of the glomerulus. The tuft dendrites re-

ceive synapses from ORNs and PGs, which are excitatory (AMPA and NMDA) and inhibitory ($GABA_B$), respectively. The apical dendrite is 300-500 μm in length and 2-10 μm in diameter; it does not bifurcate or make any synapse on its way crossing the EPL. Therefore, the apical dendrite merely passes to the soma the excitation resulting in tuft dendrites.

The MC has a large lateral dendritic tree that is extended further than 1,000 μ. The lateral dendrites sparingly bifurcat in the EPL; their diameter tapers from 6 to 1 μm. In turn, MCs can be in two subtypes on the basis of the lateral dendrites depth. MC of first type has lateral dendrites that extend deeper than seconde type.

The lateral dendrites form wide dendritic fields that connect to GCs by reciprocal synapses. Those overlapping portion of dendritic fields that belongs to different glomeruli can connect to common GCs. The number of common GCs in turn grades the strength of the inter-glomerular interactions, such as the lateral inhibition. The lateral interaction sculpts the overall activity of the OB, driving the odor representation; this is finally sent to the OC through the M/T axons.

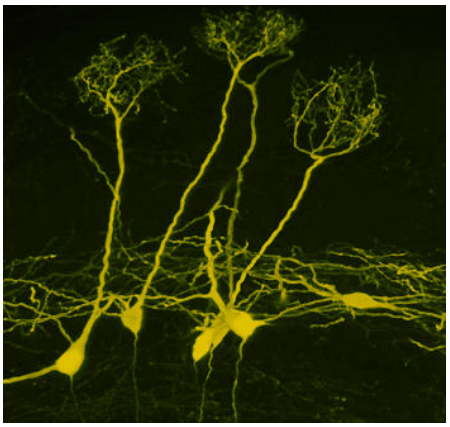

Fig. 1.4 Mitral cells observed in rats.

1.3.5 Tufted cells

Similar to MC, a TC is formed by a soma, a single apical dendrite, several lateral dendrites, and an axonal tree. The cell body is 15-20 μm in diameter. The apical dendrite traversea the EPL, terminating within a glomerulus, where it branches in several tuft dendrites; these form a tangle that is 200-300 μm in width. The lateral dendrites extend 300-600 μm. The axons ramify in many collateral branches within the GCL, while they penetrate only the OT and AON in the OC. Differently, the MCs innervate the overall OC [76].

According to the laminar position, TC can be classified in three subtypes that are the eTC, mTC, and iTC. The eTC are located in the GL. The iTC body are very deep in the EPL, so their lateral dendrites overlap with those of the MC_{II}. The mTC stands between the eTCs and iTCs. However, on the basis of the electrophysiological properties, the TCs can be classified into only two groups: one including eTCs only, another formed by both iTCs and mTCs.

The eTCs lateral dendrites extend within the GL, together with those ones of the superficial-short axon cell [8]. Experimental findings suggest that both glomeruli expressing the same odor phenotype (see par. 1.3.1) are reciprocally connected through the eTC axons [111], realizing an intrabulbar associative subsystem for the odor concentration coding[112].

1.3.6 Granule cells

The GCs are tiny inter-neurons that form a large population in the GCL. They share the GCL space with a sparse population of dSACs [113]. The dSAC axons innervate the GC on the perimsomatic region and the primary dendrites [114].

A GC is a tiny axonless neuron with a simple morphology. It has a body of 6-8 μm in diameter, from which arise spare short basal dendrites and a single primary dendrite. The primary dendrite penetrates into the EPL, where it branches in sev-

eral tuft dendrites, spreading laterally 50-200 μm. The tuft dendrites are plenty of synaptic spines that make reciprocal synapses with M/T lateral dendrites.

The GC cell bodies are grouped in horizontal clusters (i.e. islets), of which depth is deemed to reflect the age. The GCs undergo periodically to neurogenesis. The new borned GCs migrate from the SVZ toward more superficial islets, replacing the older GCs which in turn shift up to more superficial islets.

GC can be classified in three types, on the basis of the body depth and the primary dendrite extent (G_I, G_{II}, and G_{III}). The G_{III} has body that is located more superficially, so as its primary dendrite. Likely, G_{III} makes synapses with TCs. Differently, the G_{II} body and primary dendrite are located deeper, making synapses with MCs. Finally, the G_I body is located at any depth of GCL, whereas its primary dendrite is extended through the full depth of EPL. Then, G_I is capable of making synapse with both MCs and TCs [59].

1.3.7 Cell populations

The OB is constituted by 2,000 glomeruli, $50 \cdot 10^6$ ORNs, 50,000 MCs, 100,000 TCs, and 3,000,000 GCs. About $25 \cdot 10^3$ ORNs, 20-50 MCs, 40-100 TCs converge on each glomerulus.

1.4 The olfactory cortex

The OC is deemed to work as associative memory [48]; it performs the final stage of the odor processing. In Fig. 1.5 is shown the different subzones of the OC that are the OT, the AOC, and the PC. The PC is in turn subdivided in two subunits that are the anterior (aPC) and the posterior pyriform cortex (pPC). The entire OC receives the odor information filtered through the OB.

The M/Ts are the primary input source of the OC. Here, the M/T axons spread tangentially, creating a vast innervation of it. The M/T axons are thus massively in-

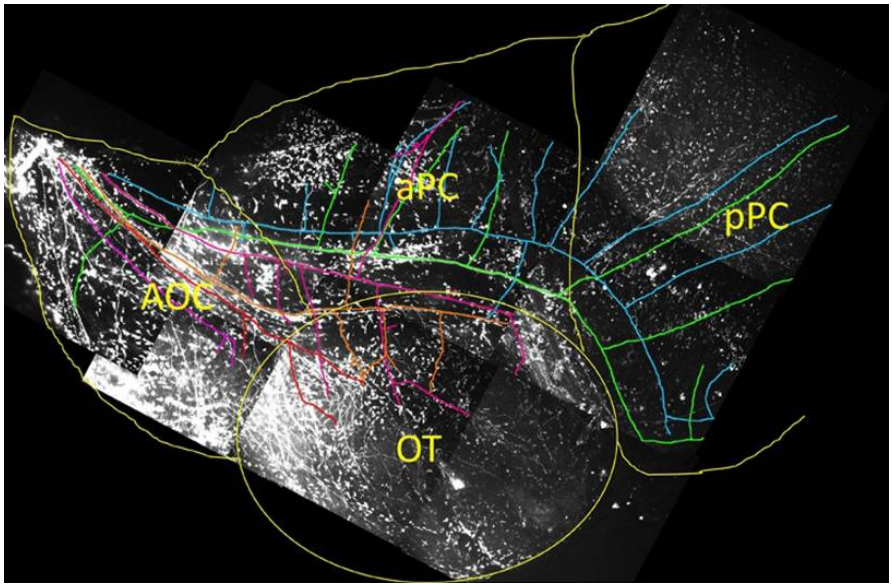

Fig. 1.5 The olfactory cortex and its subregions (adapted from [108]).

termingled in the OC [106], where none of the structural features of the OB columnar organization [29, 106, 58] is reflected in the arrangement of the M/T axonal targets. Moreover, the TCs and the MCs form two parallel pathways that project to different regions of the OC. Particularly, the TCs innervates only the OT and the AON, whereas the MCs innervates all subregions. Therefore, although TCs and MCs form two separate pathways, their outputs may be combined in the OT and the AON. However, the way they perform such task remains still unclear.

The OC also connects to other brain regions that are involved in a wide variety of functions. Fig. 1.6 shows a schematic representation of the connectivity between the OC and the rest of the brain. The OC connects to the amygdala and the enthorinal cortex through its posterior part, while it projects to the hypothalamus. Moreover, even different regions of the OC connect among themselves, while they project back to the OB, innervating all of its layers. The functional role of these projections is still unclear, but experimental findings suggest that they may drive the oscillatory activity of the OB. The PC receives axons belonging to the AON, while it projects to both the amygdala and the enthorinal cortex. The PC has a laminar organization

similar to the palecortex [4]. The AON is in turn surrounded by the neocortex, the prefrontal cortex, the PC, and the OT. It thus occupies a central position that facilitates to it interacting with other cortical regions. Although the OC connects to many brain regions, the most part of its synaptic afferences belong to the OB. The OB then mostly drives the OC activity. Therefore, so many different brain regions connecting to the OC give insight into the importance of the sense of smell, and how it can be influential in our lives. These regions are indeed reliable for many different functions. In particular, the enthorinal cortex is involved in associative memory tasks, the prefrontal cortex in mediating complex discriminative tasks related to behavioral response, the OT in rewarded decision making, the hypothalamus in regulating endocrine functions, the amygdala in driving emotional and visceral response such as aggressivity, fear, and sexual attractions. Therefore, the OB is directly or indirectly involved in many different brain functions that are not necessarily related to the odor recognition.

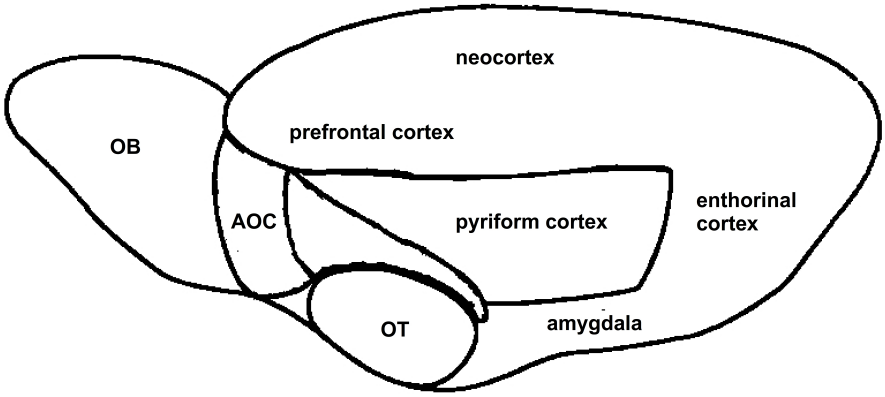

Fig. 1.6 The olfactory cortex surrounded by other cortical areas (adapted from [4]).

Moreover, the OB seems to be a cross between conscious and uncoscious processing. For example, even though pheromone-sensitive glomeruli are mostly present in the AOB, someones are on the MOB [109, 118]. They seem to respond to rewarded odors [117], projecting to the amygdala [118]. This creates an unclear cross between the MOB and AOB circuits, then a loop formed by LOT and cortical

back projections. Therefore, we can conclude that the MOB somewhat combines conscious and unconscious processing.

Chapter 2

The columnar organization of the olfactory bulb

The connectivity of the OB was examined by infecting PRV. The examination revealed that the OB is organized in many columnar computational units, called GUs. Each GU is formed by a set of neurons related to a single glomerulus, in which the GC column is the key-site for inter-glomerular interaction. The GC column has been a core concept in our research project. It has been studied and reproduced by realistic simulations, proving its reliability in all computations performed by the OB, such as the odor representation.

2.1 The experimental setup

PRV injections were performed into the OB in order to probe the OB circuitry. A representative experiment consisted of multiple local injections into either the GL or the PC.

When injections are performed into GL, the diameter of the injection site was $\approx 300\ \mu m$, covering 4-8 glomeruli. The infection worked in two steps. First, the infection propagates to the M/Ts belonging to the infected glomerulus. Second, once the PRV infection propagated into the M/Ts lateral dendrites, it passed through the most potentiated reciprocal synapses, so infecting the GCs.

When injections are performed into PC, the diameter of the injection site was $\approx 500\ \mu m$, covering all cortical layers. The infection thus spreaded retrogradely from

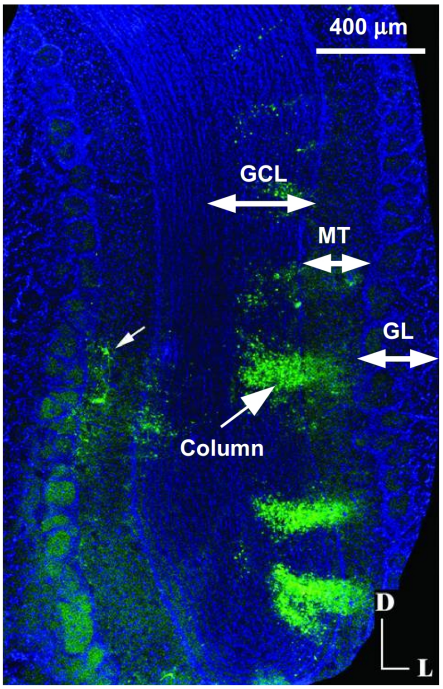

Fig. 2.1 A section of the ipsilateral bulb posterior to the injection site [58].

the cortical neurons to the M/Ts through the M/T axons. Afterward, the PRV passed from M/Ts to GCs through the most potentiated reciprocal synapses.

2.2 The evidence of the columnar organization

After injecting PRV into the GL, it was observed that the neurons were not randomly labeled (Fig. 2.1). They were indeed grouped in clusters (i.e. column) of 40-50 μm in diameter, oriented perpendicularly to the GCL boundaries. In 95% of cases, the GC columns were extended through the full depth of the GCL, each was centered beneath a single glomerulus. Taken together, these evidences suggested that GC column is in anatomical relation with individual glomerulus. Moreover, an accurate visual inspection revealed that the M/Ts were also infected upon every GC column. Therefore, not only the GCs, but all neurons that are functionally related to a single

glomerulus formed a computational unit that is anatomically columnar; this is called GU.

2.3 The inter-glomerular connectivity

Thereafter, the PRV was in two different markers: red and green. The infected neurons appeared in red, green, and yellow. In particular, yellow neurons were co-infected (co-labeled) with both red and green markers.

The injections were performed into GL sites in order to determine the degree of convergence or segregation in the lateral connectivity between M/Ts and GC columns. The injection sites were separated by at least 500 μm to minimize the chance of co-infection with both markers in M/Ts. Subsequently, a columnar labeling was apparent in the GCL (Fig. 2.2 A). All columns held only a few yellow GCs, or none, suggesting a high degree of segregation in the OB connectivity. Note that the co-labeled GCs were indicative of the amount of convergent M/T lateral dendrites on a GC column. Therefore, M/T lateral dendrites formed sparse, and segregated connections within GC column.

Then, it was determined the significance of the co-labeled GCs. First, by stechiological counts, it was estimated the percentage of neurons in every labeling color. Second, it was tested whether the convergence was more or less than expected. We compared the observed GC co-labeling against the assumption that the convergence is stochastic. For example, under this assumption, if 10% of M/Ts were in red, and 10% were in green, the expected yellow GCs should be 1% of total.

Fig. 2.3A shows the expected GC co-labeling with the stochastic connectivity model. The abscissa and ordinate represent the percentage of red and green M/T cells, respectively; the color scale shows the expected percentage of yellow GC cells. Fig. 2.3B compares the experimental convergence (points) against the expected one. Each point is representative of a real GC column; its color changes with the percent

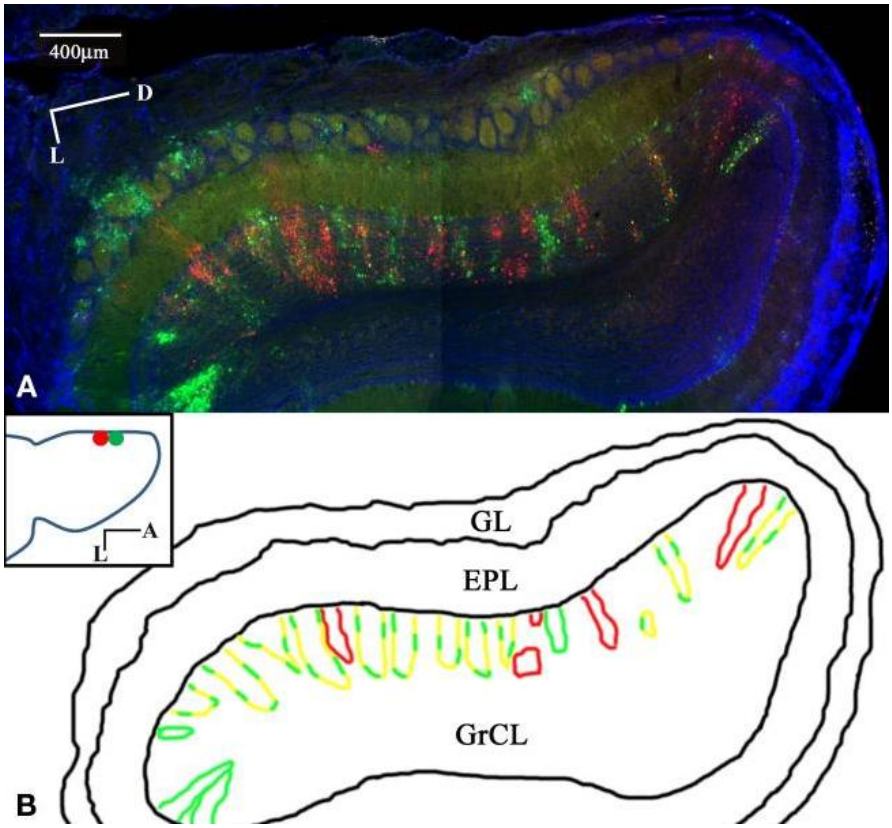

Fig. 2.2 Sparse, segregated labeling in GCL columns after GL injections [29].

of co-labeled GCs. The heaviest percent of co-labeled GCs within a column was 7% lower than expected, suggesting that the convergence is non-stochastic and sparse.

2.4 The intra-glomerular connectivity

Another key question is how the 20-50 M/Ts within a GU connect to GCs. They may connect to a common set of GCs, or connect to disjoint subsets of GCs.

PRV injections were performed in the APC in order to probe the connectivity within a GU (Fig. 2.4). Again, red and green GCs appeared, without any yellows, suggesting that the M/Ts of the same GU connect to disjoint subsets of GCs.

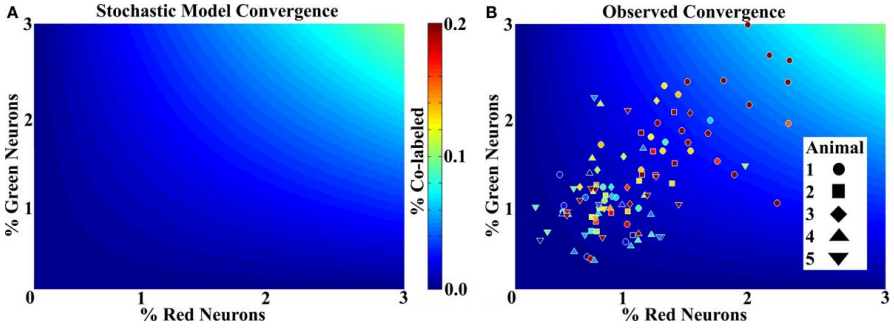

Fig. 2.3 Labeling shows non-stochastic convergence [29].

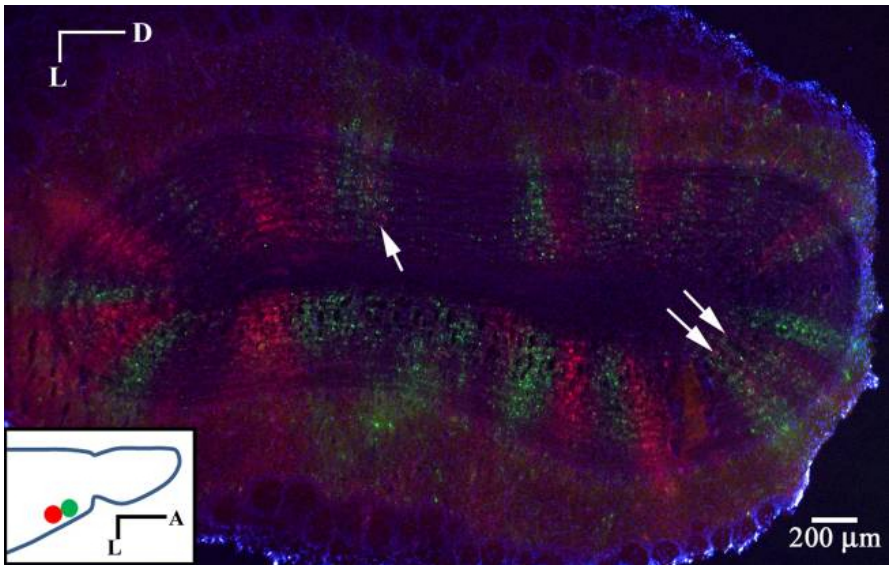

Fig. 2.4 Segregated labeling from injections in piriform cortex [29].

2.5 Discussion

All of these experimental findings addressed the connectivity within OB. They suggests that the OB is organized in GUs that are anatomically columnar (Fig. 2.1). In particular, the GC column may exert a key-role in inter-glomerular communication. GUs connect to each other through sparse and segregated subsets of GCs (Fig. 2.2), whereas no intra-glomerular interaction occurs via GCs (Fig. 2.4). In light of the experimental results, intra and inter -glomerular connectivity is schematically

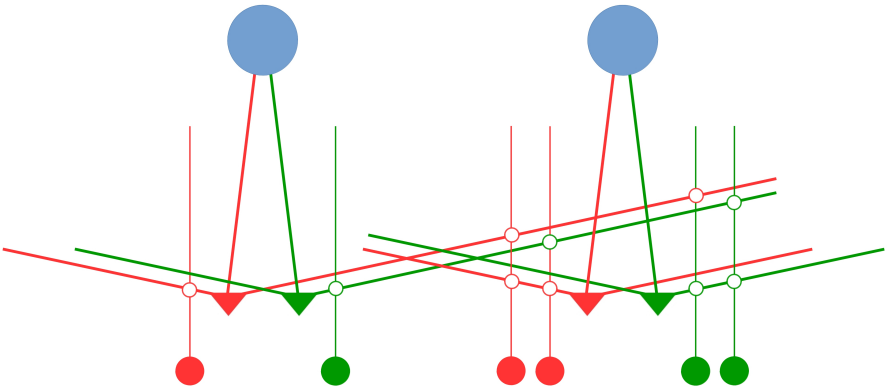

Fig. 2.5 Intra- and inter-glomerular unit connectivity [105].

shown in Fig. 2.5. A GC is limited in its own synaptic connections to its own M/T within a GU (left), but can connect to dendrites from any M/T belonging to other GUs (right).

The GC columns enable the lateral inhibition between GUs, as suggested by previous model [62]- Taking into account the long extent of the MC lateral dendrites [103, 104], the lateral inhibition might occur between glomeruli that are very far apart.

Another model predicted that the GC column formation may rely on the odor learning process [80], while GC column can be more or less demarcated depending on the intensity of the glomerular response [62]. Therefore, a GC column can be formed beneath only those glomeruli that are strongly activated during learning, and their location might therefore reflect the odor identity and intensity, so as the representation operated by the GL [105].

The structure of the GC column itself gives insight into the MCs and TCs connectivity with the GL. We know that all MCs are inhibited by the PGs, which let them firing and hushing all together within the same GU, when they receive strong and weak inputs, respectively. Thus, when the MCs are firing lead to the GC column formation [80]. TCs and MCs connect to different subpopulations of GCs that are superficial and deep GCs, respectively; hence, their activities might drive the formation of the top and bottom halves of GC column, respectively. If TCs and MCs are

both inhibited by the PGs, they should be either firing or hushing together within the same GU. Therefore, both top and bottom halves of GC column within the same GU are formed together when both MCs and TCs are firing in response to a strong input. If TCs are not connected with the GL, they are not inhibited by the PGs, so they could substantially fire even if the MCs belonging to the same GU are silent. Thus, TCs may form half GC column extended only in the superficial half of the GCL more often than observed, contradicting the fact that 95% of GC columns are extended through the full depth of GCL. Therefore, both MCs and TCs are connected with the GL circuitry in the same way.

Part II

The basic principles of the realistic neuron simulation

Chapter 3

Neuroscience modeling by realistic simulations

The membrane potential is the physical variable within the nervous system that owns three important properties:

- it can operate at high speeds;
- it can be enrich by a large repertoire of computational primitives to implement linear and nonlinear high-gain operations;
- it is able to represent sensory input pattern accurately.

The membrane potential controls a big variety of nonlinear gates, called *ionic channels*, providing the basis for implementing nonlinear operations. These channels transduce sensory input into a train of brief and rapid electric pulses, called action potential, which changes the voltage membrane, so leading to the neurotransmitter release.

A simple and elegant fashion to describe the electrical properties of neuron membrane consists of the characteristic membrane circuit. Every small segment of membrane is approximated to a single point compartment; then, many compartments are connected to represent a full dendrite or axon.

To a characteristic membrane circuit corresponds an equation set, by which one can describe active and passive properties. In multi-compartimental simulations, an equation set is associated to a single segment of membrane. This is the approach used in realistic simulation environments such as NEURON [24].

NEURON is a powerful simulation environment that allows to simulate all neuron membrane behaviours so far observed. It also realizes the software and mathematical primitives of our 3D model of the OB (see in the next chapter).

3.1 The passive properties of the neuron membrane

3.1.1 Voltage membrane

The membrane potential (V_m) is defined as the difference between intracellular (V_i) and extracellular (V_e) potentials:

$$V_m(t) = V_i(t) - V_e(t) \tag{3.1}$$

where t stands for time. At rest, the membrane has a negative potential V_{rest} (i.e. *resting potential*) that ranges between -30 and -90 mV. The resting potential results of the combined effects between two independent mechanisms, they are the intrinsic membrane permeability and the membrane-bound pumps. These mechanisms induce two distinct perpetual ion flows across the membrane, so that the net ionic current is zero. This leads to a dynamic electro-chemical equilibrium that characterizes the value of V_{rest}. In particular, the intrinsic membrane permeability alone would induce a membrane potential that obeys to the Nernst's law. At the same time, the membrane-bound pumps upkeep the ions gradient by actively transporting sodium and potassium ions across the membrane, driving the membrane potential. Maintaining this equilibrium requires a strong energy expenditure, it was indeed estimated that the membrane-bound pumps spend half of the total metabolic energy consumed by mammalian brain.

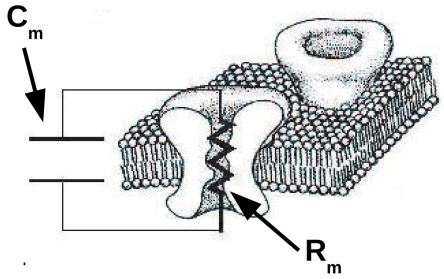

Fig. 3.1 The passive neuronal membrane [1].

The capacitance

The neuron membrane is made by two layers of phospholipid molecules that form a thin insulating layer, isolating the cell from the external space. The high resistivity of the lipids prevents passages of charge across the membrane, thus the electric properties of the membrane can be described by a capacitance. The capacitance C_m is a measure of how much charge Q needs to be distributed across the membrane to set the potential V_m up to a certain value (Fig. 3.1).

$$Q(t) = C_m \cdot V_m(t) \tag{3.2}$$

the capacitance is usually specified in terms of the *specific membrane capacitance*, in units of microfarads per square centimeter of membrane area ($\frac{\mu F}{cm^2}$).

The current flow corresponding to a variation of the voltage membrane across the capacitance is obtained by differentiating the eq. 3.2 with respect to time

$$I_C(t) = C_m \frac{dV_m(t)}{dt} \tag{3.3}$$

Therefore, the membrane capacitance imposes a constraint on how rapidly V_m can change in response to this current, so that the larger the capacitance, the slower the voltage change.

The Resistance

The membrane is endowed by a large variety of proteins (Fig. 3.1), which subserve an enormous range of specific cellular functions, including ionic channels, pumps, and receptors. They act as gates in the phospholipid barrier through which ions can be selectively transferred from one side to the other.

In particular, ionic channel can be described as a current flow by a simple resistance, called *membrane resistance*. The membrane resistance is usually specified in terms of the *specific membrane resistance* (R_m), in resistance times unit area ($\Omega \cdot cm^2$).

The ions flow induces a current (I_c), of which characteristic equation is

$$\frac{dV_m(t)}{dt} = R_m \cdot I_c(t) \tag{3.4}$$

The membrane circuit

From an electrical point of view, a single compartment approximates a small membrane segment to an RC circuit. When a segment is assumed to be so small, the differences of electrical potential across the membrane are neglected. Therefore, such a cell piece is considered to be *isopotential*.

The dynamics of this circuit is mathematically described by applying *Kirchhoff's law*. The current flowing across the capacitance is given by the eq. 3.3, whereas the current through the resistance is

$$I_R = \frac{V_m - V_{\text{rest}}}{R} \tag{3.5}$$

Because of the conservation low of currents, the capacitive and resistive currents must be equal to an external one

$$C_m \frac{dV_m(t)}{dt} + \frac{V_m(t) - V_{rest}}{R_m} = I_{\text{inj}}(t)$$

where $\tau = R_m C_m$ with units of $\Omega \cdot F = sec$. We can rewrite this as

$$\tau_m \frac{dV_m(t)}{dt} + V_m(t) - V_{rest} = R_m \cdot I_{\text{inj}}(t) \tag{3.6}$$

This equation is known as the *membrane equation* and is a first order ordinary differential equation.

An important detail is the sign of the external current. By convention, an outward current, which is a positive charge flowing from inside the neuron to the outside, is represented as a positive current. An outward current, which is delivered through an intracellular electrode, makes the inside of the cell more positive; the physiologists then use to say that the cell is depolarized. Conversely, an inward directed current supplied by the same electrode is plotted by convention in the negative direction; this makes the inside an external source but is generated by a membrane conductance.

3.2 Modeling of elongated neuron process: the cable equation

At this stage, one wants to extend the membrane model to represent a full dendrite or axon. This comes as a series of discrete compartments, as expressed by the eq. 3.6, connected by an axial resistance R_i (Fig. 3.2). In light of the Ohm's law, the characteristic equation is

$$V_i(t,x) - V_i(t,x+\Delta x) = R_i \cdot I_i(t,x)$$

when $\Delta x \to 0$, and with $V_m = V_i$, it can be rewritten as

$$\frac{dV_m(t,x)}{dx} = -r_i \cdot I_i(t,x) \tag{3.7}$$

In this scheme, we have two currents flowing through a neuronal tissue, the $i_m(x,t)$ that crosses the membrane at location x, and the $I_i(x,t)$ that propagates along the axial direction.

It is noteworthy the dominant fraction of current inside a neuronal process flows along the axial direction, while only a very small amount flows across the mem-

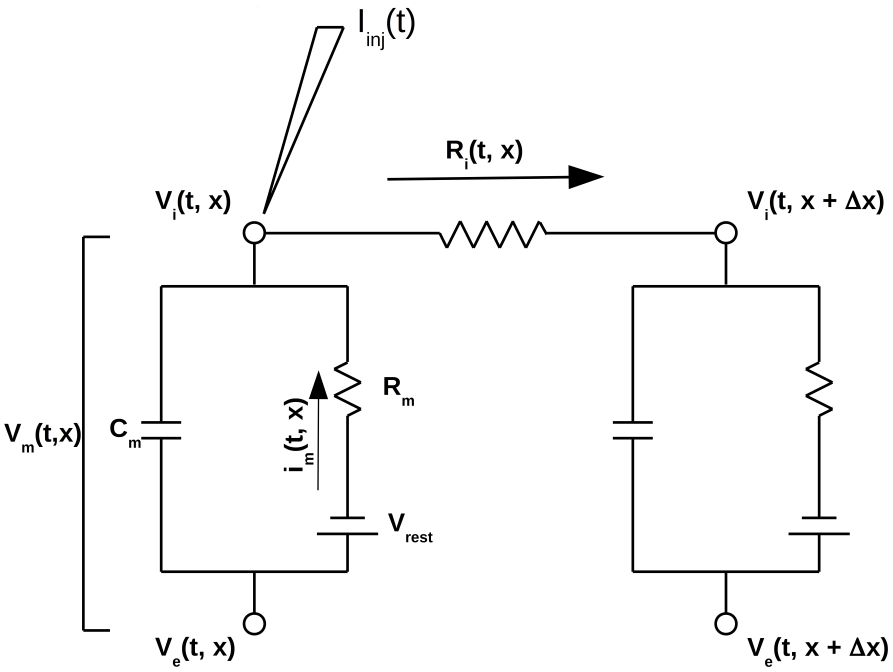

Fig. 3.2 Neuron membrane and axial resistance.

brane. This is due to both geometrial and electrical properties of the membrane cable.

3.3 The action potential

Neurons generate series of brief voltage pulses in response to an input that is sufficiently strong. These pulses, called *action potentials* (Fig. 3.3), propagate at constant velocity and amplitude. The ionic mechanisms underlying the initiation and propagation of action potential were elucidated in the squid axon by Hodgkin and Huxley in Cambridge (1952)[5].

Hodgkin and Huxley dissected the membrane current into two components. The total membrane current is thus the sum of the ionic current and the capacitive current:

$$I_m(t) = I_{ionic}(t) + C_m \frac{dV(t)}{dt}$$

The action potential involves two independent voltage-dependent ionic conductances, a sodium conductance G_{Na} and a potassium conductance G_K. Hence, the total ionic current flowing is the sum of a sodium current and a potassium current:

$$I_{ionic} = I_{Na} + I_K$$

The individual ionic currents $I_*(t)$ are linearly related to the membrane potential:

$$I_* = G_*(V_m(t))(V_m(t) - E_*)$$

where the ionic reversal potential E_* is given by Nerst's law for the appropriate ionic species (Fig. 3.4).

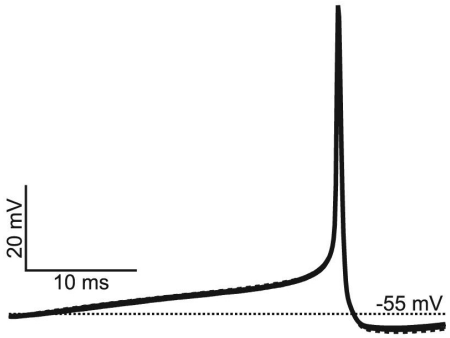

Fig. 3.3 Example of action potential [2].

3.3.1 The potassium K_{DR} current

In the Hogdkin and Huxley model, the equation of the potassium current is

$$I_{K_{DR}} = \overline{G_{K_{DR}}} \cdot n(V_m(t))^4 \cdot (V_m - E_K) \tag{3.8}$$

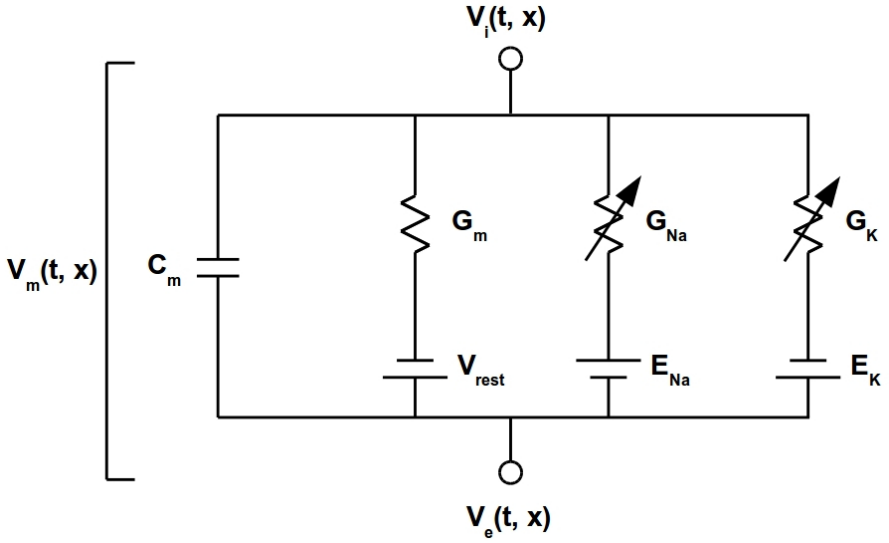

Fig. 3.4 The extension of the characteristic membrane circuit including the active membrane properties.

where $\overline{G_K}$ is the maximal conductance of channel and E_K is the reversal potential; $n(V_m(t))$ describes the state of a fictional *activation particle* and is dimensionless number ranging between 0 and 1; I_K as outward current is always positive (for $V_m \geq E_K$). We assume that the probability of finding one activation particle in its *permissive* state is n, while it can be in its *nonpermissive* state with probability $1-n$. Thus the transition from a state to the other is governed by first-order kinetics:

$$\text{n} \underset{\alpha_n}{\overset{\beta_n}{\rightleftharpoons}} \text{1-n}$$

where α_n and β_n are voltage-dependent rate (1/sec), specifying how many transitions occur in a time unit. In light of the mass model law, this scheme corresponds to a first-order differential equation:

$$\frac{dn}{dt} = \alpha_n(V)(1-n) - \beta_n(V)n \tag{3.9}$$

The eq. 3.9 can be simplified, rewriting it in term of a voltage-dependent time constant $\tau_n(V)$ and a steady-state value $n_\infty(V)$ with

$$\frac{dn}{dt} = \frac{n_\infty - n}{\tau_n} \tag{3.10}$$

where

$$\tau_n = \frac{1}{\alpha_n + \beta_n} \tag{3.11}$$

and

$$n_\infty = \frac{\alpha_n}{\alpha_n + \beta_n} \tag{3.12}$$

While τ_n has a bell-shaped dependency, n_∞ is a monotonically increasing function of V_m (Fig. 3.5). The curve relating the steady-state potassium conductance to the membrane potential is an even steeper function, given the fourth-power relationship between G_K and n.

3.3.2 The sodium current

The dynamics of the sodium channel are more complex. Hodgkin and Huxley assumed the existence of two particles in the sodium channel that are the *activation particle m* and the *inactivation particle h*. The characteristic equation of the sodium currenti is

$$I_{Na} = \overline{G_{Na}} \cdot m\left(V_m\left(t\right)\right)^3 \cdot h\left(V_m\left(t\right)\right) \cdot \left(V_m - E_{Na}\right) \tag{3.13}$$

where G_{Na} is the maximal sodium conductance, E_{Na} is the sodium reversal potential, m and h are dimensionless numbers, with $0 \leq m,h \geq 1$. By convention the sodium current is negative throughout the physiological voltage range (for $V < E_{\mathrm{Na}}$).

The amplitude of the sodium current is contingent of four hypothetical gating particles making independent first-order transitions between an open and a closed state.

$$\frac{dm}{dt} = \alpha_m\left(V\right)\left(1 - m\right) - \beta_m\left(V\right)n \tag{3.14}$$

and

$$\frac{dh}{dt} = \alpha_h(V)(1-h) - \beta_h(V)n \tag{3.15}$$

Similar to the potassium channel, both τ_m and τ_h are bell-shaped curves, but with a tenfold difference in duration (Fig. 3.5). While m_∞ s a monotonically increasing function of V, as expected of an activation variable, h_∞ decreases with increasing membrane depolarization, the defining feature of an inactivating particle. Without inactivation, the sodium conductance would remain at its maximum value in response to a depolarizing voltage step. For voltages below or close to the resting potential, the activation variable m is close to zero while at positive potentials the inactivation variable h is almost zero.

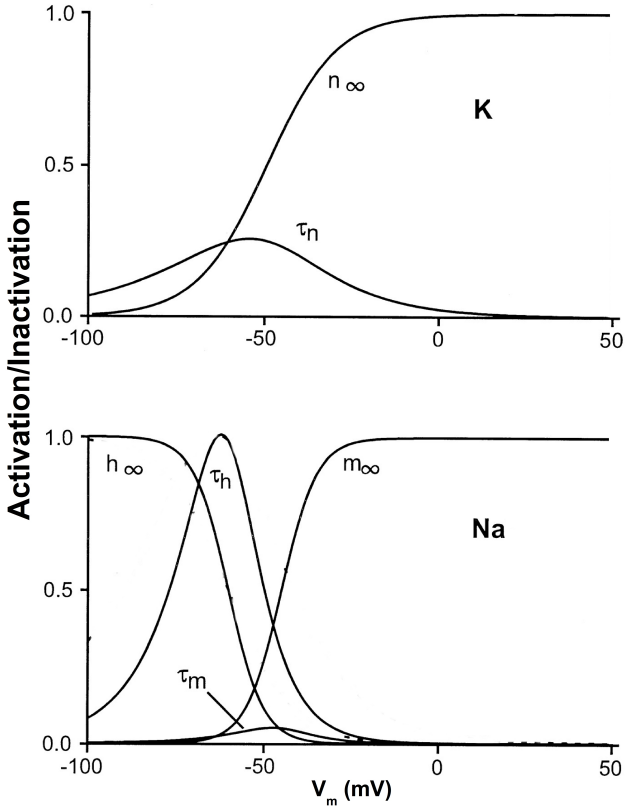

Fig. 3.5 Sodium and potassium time constants and activation/inactivation curves [3].

3.3.3 The K_A current

The K_A is another potassium current that act in smaller time scale than the delay rectifier current. The dynamics of the K_A conductance are similar to the sodium one. This current is not included in the original version of the Hodgkin and Huxley model but its characteristic equation reflects the same kinetic scheme. The channel is formed by a single *activation particle m* and a single *inactivation particle h*:

$$I_{K_A} = \overline{G_{K_A}} \cdot m(V_m(t)) \cdot h(V_m(t)) \cdot (V_m - E_K) \tag{3.16}$$

where G_{K_A} is the maximal conductance, E_K is the potassium reversal potential. m and h are dimensionless numbers, with $0 \leq m,h \geq 1$.

Similar to the other channels described above, both τ_m and τ_h are bell-shaped curves, while m_∞ is a monotonically increasing function of V, h_∞ decreases with increasing membrane depolarization, similar to sodium channel.

The sigmoid of activation particle is shifted few millivolts less than K_{DR} and Na particles. Thus the K_A modulates the action potential, delaying its onset, and decreasing its peak value. The overall effect is the induction of a faster hyperpolarization. Paradoxically, although the K_A current reduces the input resistance, it speeds up the overall dynamic of action potential, so increasing the maximum firing rate.

3.4 Generation of action potential

In the Hodgkin and Huxley model [5], all currents flowing across the membrane are described by a single equation:

$$\begin{aligned} C_m \frac{dV_m(t)}{dt} &= G_m(V_{rest} - V_m(t)) + \\ \overline{G_{Na}} m^3 h(E_{Na} - V_m) + \overline{G_K} n^4 (E_K - V_m) &+ \\ I_{inj}(t) & \end{aligned} \tag{3.17}$$

where I_{inj} is the current that is injected via an intracellular electrode, or induced by the activation of synaptic receptor. The eq. 3.17 is a nonlinear differential equation that constitute the core of our simulations environment. This equation allows to simulate the initiation and propagation of action potentials, together with the synaptic activation.

The neuronal membrane responds in either of two ways to brief depolarizing pulse; if its amplitude move the V_m below the threshold, the membrane returns to the resting potential after slightly depolarizing. Differently, a stronger pulse that let the V_m crossing the threshold, triggers the action potential. An important features of action potential regards its shape, which is not affected by the stimulus.

The depolarization increases both the sodium (m) and potassium (n) activations, and decreases the sodium inactivation (h). Because the time constant of the sodium activation particle (τ_m), its activation is more than one order of magnitude faster than the potassium activation particle (τ_n) and the potassium inactivation particle (τ_h) at these voltages. We can consider the latter two to be stationary when the sodium conductance G_{Na} increases.

3.4.1 The membrane response to a strong stimulus

When the current pulse is strong enough to overcome the threshold, the depolarization due to the voltage-independent membrane components reaches a point where the amount of I_{Na} generated exceeds the amount of I_K. The membrane voltage thus undergoes a runaway reaction: the additional I_{Na} depolarizes the membrane, further increasing m, which increases I_{Na}, causing further membrane depolarization. Thus the inrushing sodium moves the membrane potential within a fraction of a millisecond to 0 mV and beyond. In the absence of sodium inactivation and potassium activation, this positive feedback would continue until the membrane would come to rest at E_{Na}. After a delay both the slower sodium inactivation h as well as the potassium activation n will turn on. Sodium inactivation acts to directly decrease

the amount of sodium conductance available, while the activation of the potassium conductance tends to try to bring the membrane potential toward E_K by increasing I_K. Thus both processes cause the membrane potential to dip down from its peak. Since I_K persists longer at small amplitudes, the membrane potential is depressed to below its resting levels. During this period, it is more difficult to initiate an action potential than before; the membrane remains in a *refractory state*. The neuron persists in this state until the inactivation h is not discharged and the potassium activation is not closed again. At these low potentials, the system finally returns to its initial configuration as V_m approaches the resting potential.

The ionic channels involved in generating action potential consume large amount of energy, in form of ATP. In particular, the sodium channel needs threefold more the energy consumed by the potassium channel, and such a quantity of energy increases as the overlap over time between the opening curves of these channels. In fact, under this condition, the depolarizing effect of the sodium is somewhat reduced by the potassium inrush, which occurs at the same time instant. Thus more sodium is finally needed to generate a full action potential. Therefore, to optimize the ATP consumption, mammal neurons own potassium and sodium channels of which curves do not overlap during action potential [107].

3.5 The synapses

A fast communication between two neurons occurs through specialized microscopical sites called synapses. The synapse is the functional unit whereby the brain connectivity is realized, then several important mechanisms such as the memory and the brain computations.

Synapse can be in two different types, they are the *electrical (i.e. gap junctions)* and *chemical synapses*. The gap junction is the one structurally simplest, it is formed by a neurite tissue that works likewise a passive cable. The electrical synapse is less common than the chemical one. The chemical synapse consists of a *presynaptic (ax-*

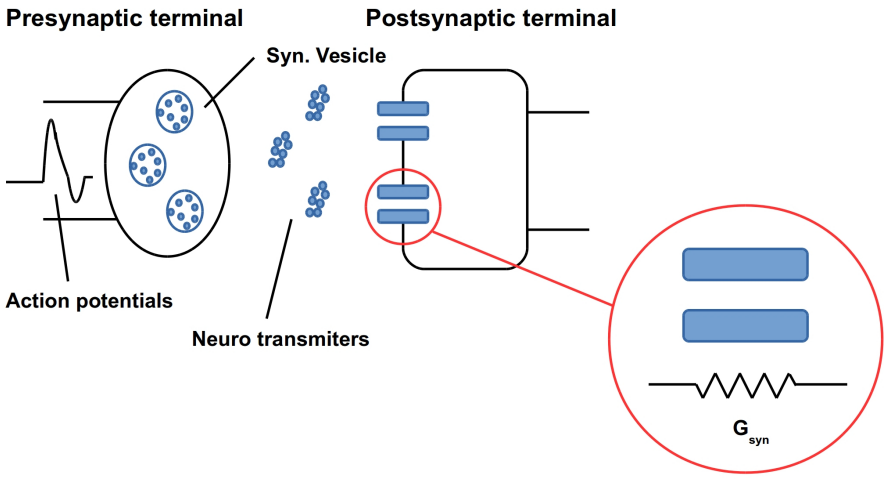

Fig. 3.6 A generic schematic representation of chemical synapse.

onal) terminal and a *postsynaptic terminal* that is usually located on dendrite (Fig. 3.6). The area of contact between pre and post -synaptic terminal has a diameter of 0.5-1.0 μm, whereas the terminal is only slightly larger.

The presynaptic terminal holds the neurotransmitters, which are packed in many small vesicles. When an action potential invade the presynaptic terminal, it causes an inrush of calcium ions via voltage-dependent calcium channels. They cause to release the synaptic vesicle through a complex chain of metabolic reactions called exocytosis. The neurotransmiters thereby diffuses through the synaptic cleft where is uptaken by a postsynaptic receptor. Upon its activation, the receptor causes a rapid and transient change in the membrane potential (Fig. 3.6, left part).

The receptor can work by two different action mechanisms. A *ionotropic receptor* is directly coupled to a ionic channel, which opens and permits certain types of ions to cross the postsynaptic membrane. Its action is rapid and transient. Ionotropic receptors are the most part of synapses present in the OB, such as the reciprocal synapse between M/Ts and GCs. On the other hand, binding of neurotransmitter to *metabotropic receptor* triggers a complex cascade of biochemical reactions inside the postsynaptic cell, based on molecules termed *second messengers*. It acts in hun-

dred milliseconds. Finally, the overall process leads to opening some ionic channels or modulate kinetic or conformation thereof.

From the anatomical point of view, synapse can be classified according to the morphology into two classes, *Gray type I* and *Gray type II* synapses. Type I synpases (i.e. asymmetrical synapses) have been found to be excitatory, whereas Type II synapses (i.e. symmetric synapses) act in a inhibitory manner. Typical inhibitory receptors are the GABA A and B, whereas the AMPA and NMDA are excitatory. All these receptors bind with different type of neurotransmitters. Particularly, the GABA receptors bind with GABA and glycine, while the AMPA and the NMDA bind with glutamate and aspartate. With the activation of an excitatory synapse is excitatory, the postsynaptic membrane potential depolarizes; this is also referred as *excitatory postsynaptic potential* (i.e EPSP). Conversely, with the activation of inhibitory synapse, the postsynaptic membrane is hyperpolarized; this is usually called *inhibitory postsynaptic potential* (i.e IPSP). To excitatory and inhibitory postsynaptic potentials correspond excitatory (EPSC) and inhibitory postsynaptic currents (IPSC), respectively, induced by the activation of the ionic channels associated to receptor. The instensity of a postsynaptic current I_{syn} is

$$I_{syn} = G_{syn}(t)\,(V_m(t) - E_{syn}) \tag{3.18}$$

where G_{syn} depends on time and describes the time course of the postsynaptic current, and it is related to the opening fraction of channel; E_{syn} is the reversal potential of channel, and depends on the specifity of ion species that flow through, its value is in accord to the Nerst's law. The E_{syn} term thoroughly characterizes the excitatory and inhibitory behavior of synapse, which is in turn related to the cases $E_{syn} < V_{rest}$ and $E_{syn} > V_{rest}$, respectively; the value of E_{syn} is 0 mV at NMDA and AMPA receptors, and -80 mV at GABA ones.

3.5.1 The plasticity rule

The *synaptic weight* (w) is a scalar variable that describes the synaptic strength in term of the peak of postsynaptic potential. Since the time course of postsynaptic current is driven by the term G_{syn} (eq. 3.18), it is immediate to assume

$$G_{syn} \propto w$$

The synaptic weight is moreover indicative of its internal state s in which the synapse itself stands, which in turn depends on the past activities of neuron. It is noteworthy the whole synaptic transmission, then neurotransmitter release and uptake, are stochastic phoenomena, therefore, they can be seen from a probabilistic point of view. The synaptic weight is

$$w = n \cdot p \cdot q(t)$$

where w is the synaptic weight, n is the number of presynaptic vesicles, p is the probability of presynaptic release, q is a variable that describes the postsynaptic response which itself is a function of time.

The synaptic weight is not stationary and can change with the neuron activity. This phoenomena is also referred as *synaptic plasticity*. There are diverse synaptic plasticity protocols. The synaptic plasticity can be in two different form: the *short* and the *long -term plasticity*, according to how long the change of weight lasts. The synaptic weight can either increase, or decrease, or being stationary as function of the stimulus. A synaptic weight increment is called *potentation*, while its decrement is called *depression*.

Because of the small dimension of the synapses, they are not easy to be experimentally analyzed. Hence, the mechanisms underlying the synaptic potentiation and depression are not fully understood. Conjectures involving the presynaptic terminal assume the potentiation/depression may change the number of vesicles n, or the release probability p. Less usually, it is assumed that changes may involve the postsynaptic receptor represented by the term q.

However, despite of these assumptions, the synaptic plasticity can be described by the fluctuation of the synaptic state Δs. In particular, in our 3D model we have implemented the non-hebbian synapses, in which Δs depends only on the interspike interval:

$$\Delta s = \begin{cases} +1 & \text{if the interspike interval is} > 33 \text{ ms} \\ -1 & \text{if the interspike interval is} > 250 \text{ and } \leq 33 \text{ ms} \\ 0 & \text{otherwise} \end{cases}$$

The maximum value of synaptic state is $s_{\max}$, so that $s_{\max} = s_{1/2}$. The state s changes as

$$s = \begin{cases} s + \Delta s & \text{if } s < s_{\max} \text{ and } \Delta s = +1 \text{ or } s > 0 \text{ and } \Delta s = -1 \\ s & \text{otherwise} \end{cases}$$

Finally, the synaptic weight is

$$w(s) = \frac{1}{1 + \exp\left(\frac{s - s_{1/2}}{c}\right)}$$

where the synaptic weight w is function of the state s through a sigmoidal law, c is is the sigmoid slope, $s_{1/2}$ is the center of sigmoid and characterizes how many spikes at potentiation frequency are needed to achieve the maximum synaptic weight with $s = 0$ as initial condition.

Chapter 4

A model of nonlinear cable equations for neurons with the full dendritic tree

4.1 A brief introduction to the common experimental procedures

In their experiments, Hodgkin and Huxley used *space and voltage clamp* to characterize the local dynamic of a section of squid axon.

From a geometric point of view, a squid axon can be seen as a long cylindrical tube encased in a double-layered lipidic membrane and filled by axoplasm. Such a membrane acts as insulator, whereas the axoplasm exhibits resistive properties. Variations of the transmembrane voltage are thus due to the current that flows longitudinally through the axoplasm.

An important feature of the neuron membrane is its permeability to ion species. This is fundamental properties to generate action potentials. The permability is measured in *specific ionic permeability per unit area* as a function of the transmembrane voltage. The current flowing through the axoplasm induces fluctuations in the transmembrane voltage, so making difficult measuring the permeability to specific ions.

In order to eliminate these longitudinal fluctuations of the membrane potential, one can insert a wire that acts as a terminal of the internal voltage inside the membrane section. This wire must traverses the whole section and must be oriented along the longitudinal axis. Under this condition, the transmembrane voltage is approximately constant. This method is called *space-clamp*.

Instead, the *voltage clamp* is based on a negative feedback amplifier that keep the membrane voltage at a fixed value. There are two major advantages in using this method:

- the input resistance of the amplifier is high, so that setting the membrane voltage up to a constant value is easy
- the output resistance is low, so the output membrane potential remains stable even in presence of fluctuations within the section

4.2 The generation of the action potential

Here, we show an extended version of the Hogdkin and Huxley model [5] of the action potential generation, including the distributions of the ionic channels throughout an axonal or dendritic section. We assume the action potential propagation is a function of the distance x, which is measured along the axial direction (Fig. 4.1). The section is approximated as a thin cylinder with radius a. We assume that, within the cylinder, the cytoplasm works as a ionic medium with conductive properties, called *core conductor*. Even outside the cylinder, there is another type of ionic medium with conductive properties and without any resistive property.

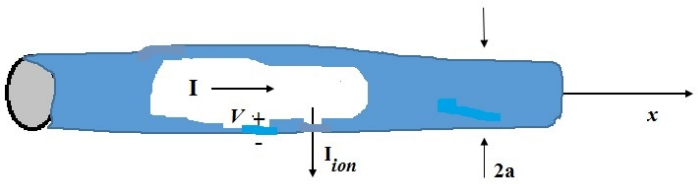

Fig. 4.1 Sketch of axonal section modeled as a thin cylinder with radius a.

Here, we define several variables that are used in the equations below:

$$R_i = \pi a^2 r_i$$

$$R_m = 2\pi a r_m$$

$$C_m = \frac{c_m}{2\pi a}$$

where

- r_i is the axial resistance of the core conductor, measured in Ω/cm
- R_i is the specific intercellular resistance, measured in $\Omega \cdot cm$
- r_m is the specific membrane resistance, measured in $\Omega \cdot cm$
- R_m is the membrane resistance, measured in $\Omega \cdot cm^3$
- c_m is the specific membrane capacitance, measured in F/cm
- C_m is the membrane capacitance, measured in F/cm^3
- x is the distance along the axis of the core conductor, usually measure in μm
- V_i the internal voltage of the core conductor, measured in mV

We assume the current flows in the same direction along which x increases. Given V_i as a function of x and t, because of the Ohm's law, we obtain

$$\frac{\partial V_i}{\partial x} = -I_i r_i$$

and

$$\frac{\partial^2 V_i}{\partial x^2} = -r_i \frac{\partial I_i}{\partial x} \tag{4.1}$$

where I_i is the intracellular current.

The eq. 4.1 allows to find the relation between intracellular (I_i) and transmembrane (I_m) currents within the section. If the transmembrane current crosses the membrane outward (or inward) over a small length Δx, the I_i decreases (or increases) over Δx (Fig. 4.2).

Given I_1 and I_2 crossing the section at x_1 and x_2, respectively, because of the conservation law of current, we obtain

$$I_2 - I_1 = -I_m \Delta x$$

with the limit $\Delta x \to 0^+$, we obtain

$$\frac{\partial I_i}{\partial x} = -I_m \tag{4.2}$$

By combining the eq. 4.2 with the Ohm's law, we obtain

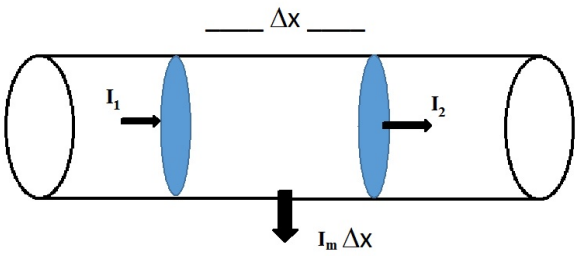

Fig. 4.2 Decrease/increase of I_i as the current I_m.

$$\frac{\partial^2 V_i}{\partial x^2} = r_i I_m \tag{4.3}$$

We remind that the transmembrane voltage is $V = V_i - V_e$, where V_i and V_e are the internal and external voltages, respectively. V, V_i, and V_e are functions of x and t. I_m is modeled by using a characteristic $R-C$ circuit of neuron membrane, so the membrane is approximated by many identical characteristic $R-C$ circuits (chapter 3 for a more detailed explaination).

Because of the Kirchoff's laws, we obtain

$$I_m = c_m \frac{\partial V}{\partial t} + \frac{V_i - V_e}{r_m} \tag{4.4}$$

By combining the eq. 4.4 with the eq. 4.3, we finally obtain

$$\frac{r_m}{r_i}\frac{\partial^2 V}{\partial x^2} = r_m c_m \frac{\partial V}{\partial t} + V \tag{4.5}$$

where

$$\tau_m = r_m c_m$$

and

$$\lambda = \sqrt{\frac{r_m}{r_i}}$$

We thus rewrite the eq. 4.5 as

$$\tau_m \frac{\partial V}{\partial t} = \lambda^2 \frac{\partial^2 V}{\partial x^2} - V \tag{4.6}$$

This is called *cable equation*.

Next, we consider the specific ionic currents in addition to the eq. 4.5, obtaining

$$I_m = C_m \frac{\partial V}{\partial t} + I_K + I_{Na}$$

so that

$$C_m \frac{\partial V}{\partial t} + \frac{a}{2R_i} \frac{\partial^2 V}{\partial x^2} - g_K(V,t)(V - E_K) - g_{Na}(V,t)(V - E_{Na}) \tag{4.7}$$

where g_K and g_{Na} are the potassium and sodium conductances as in the classic Hodgkin-Huxley model. This is the *Hodgkin-Huxley model* with spatial and temporal domain. The variable x ranges in $[0, L]$, with boundary conditions $x = 0$ and $x = L$. At $x = 0$, there is a junction between different sections, and $V(0,t)$ can be equal as $V_s(t)$ (i.e. Dirichlet boundary condition). At $x = L$, if the resistance is so high that can be approximated as infinite, the amount of the axial current is negligible. Since the axial current is the voltage derivative along x, the last bounday condition can be rewritten as

$$\frac{\partial V}{\partial x}(L,t) = 0$$

which is know as *zero-slope or von Neumann boundary condition*, and it implies a sealed-end terminal. This is the most common assumption in modeling the neurite terminals.

There is another boundary condition, under which one assumes the cutted neurite terminal is open (short-circuit). The intracellular voltage at the termination thus coincides with the extracellular potential, then the effective potential is zero ($V(L,t) = 0$).

Remark. The cable equation (linear or non-linear) can be inferred from the Kirchoff's law from a multi-compartmental model of action potential. In this model, the flow balance among compartments is zero at limit when the compartment size tends to zero. Conversely, the multi-compartmental model can be seen as a finite differences approximation of the cable equation.

4.3 Analysis of the Hodgkin-Huxley model in the spatio-temporal domain

We introduce a generalization of the *Hodgkin-Huxley model* by including the equations of different types of ionic channels:

$$\begin{cases} \tau \frac{\partial u}{\partial t} = \lambda^2 \frac{\partial u}{\partial x^2} - u - \sum_{j=1}^{N} \bar{g}_j m_j^{s_j} h_j^{q_j} (u - E_j) + J(t) \\ \frac{\partial m_j}{\partial t} = \alpha_j(u)(1 - m_j) - \beta_j(u) m_j \\ \frac{\partial h_j}{\partial t} = a_j(u)(1 - h_j) - b_j(u) h_j \end{cases} \tag{4.8}$$

where $x \in [0, L]$ is the longitudinal distance along the neurite (without branching), t is the time, $u(x,t)$ is the membrane voltage with $N > 1$ ion species, $\bar{g}_j$ is the conductance peak of the $j-$th ionic channel with Nernst potential E_j, $m_j(x,t)$ and $h_j(x,t)$ are dimensionless variables describing activation and inactivation of the jth channel, s_j and q_j are their respective numbers, α_j, β_j, a_j, and b_j are rate functions that are nonnegative bounded smoothed functions so that $0 \leq m_{j0}, h_{j0} \leq 1$, and $J(t)$ is a generic external current. The initial conditions are $u(x,0) = u_0(x)$, $u(0,t) = V_0$, $\frac{\partial u}{\partial x}(L,t) = 0$, $m_j(x,0) = m_{j0}(x)$, and $h_j(x,0) = h_{j0}(x)$.

We want to show that the Hogdkin-Huxley model is well-posed in terms of Hadamard.

Taking into account the results shown in Lamberti [139] and Mascagni [140, 141], we split the first equation in of the eqs. 4.8 into the non-linear cable equation

$$\tau \frac{\partial u}{\partial t} = \lambda^2 \frac{\partial u}{\partial x^2} - B(m,h)u + D(m,h,t) + J(t), \tag{4.9}$$

where

$$B(m,h) = 1 + \sum_{j=1}^{N} \bar{g}_j m_j^{s_j} h_j^{q_j}$$

and

$$D(m,h,t) = \sum_{j=1}^{N} \bar{g}_j m_j^{s_j} h_j^{q_j} E_j$$

Next, the eq. 4.9 is rewritten in a more abstract format by using a variational setting (see e.g [135, 143]). We thus consider the following functions of the space (see the format in [135])

$$H = L^2(0,L)$$

$$V = \{\, u \in H^1(0,L),\ u(0) = V_0 \,\},$$

where H^1 is a Sobolev space.

We then search for a solution (u,m,h), so that

$$u \in L^2(0,T;V) \cap H^1(0,T;H) \text{ and } m_j,\ h_j \in H^1(0,T;H)$$

Note that the rate functions $\alpha_j,\ \beta_j,\ a_j,\ b_j$ and are $H-$valued functions.

Without lossing in generality, hereafter, we analyse m_j, but the same analysis can be extended to h_j. By assuming $m_0 \in H$ so that $0 \leq m_0 \leq 1$, we obtain

$$m'(t) = \alpha(v)(1-m) - \beta(v)m \tag{4.10}$$

where $m(0) = m_0$, v is a function in $L^2(0,T;H)$ over the domain $(x,t) \in [0,L] \times [0,T]$ with $T > 0$, while $\alpha,\ \beta$ are $H-$valued integrable nonnegative functions.

We then define the following functions

$$A(t) = \int_0^t \alpha(v)ds$$

$$B(t) = \int_0^t \beta(v)ds$$

Therefore, the only solution m_v of eq. 4.10 is

$$m_v(t) = e^{-(A(t)+B(t))}\left[m_0 + \int_0^t e^{(A(s)+B(s))}\alpha(v)ds\right]$$

Since $\alpha, \beta \geq 0$, we have

$$0 \leq \int_0^t e^{(A(s)+B(s))}\alpha(v)ds \leq \int_0^t e^{(A(s)+B(s))}(\alpha(v)+\beta(v))ds = e^{(A(t)+B(t))} - 1,$$

and

$$0 \leq m_v(t) \leq e^{-(A(t)+B(t))}\left[m_0 + e^{(A(t)+B(t))} - 1\right] = 1 - (1-m_0)e^{-(A(t)+B(t))}.$$

where $0 \leq m(t) \leq 1 \ \forall t$. The **uniqueness of the solution** is thus proved.

Moreover, if $|v(t,x)| \leq K$, with (t,x) ranging in $[0,T] \times [0,L]$, we have $0 \leq \alpha(v), \beta(v) \leq C_K$. After several naive computations, we obtain

$$\|m_{v_1}(t) - m_{v_2}(t)\|_H \leq L_K \int_0^t \|v_1(s) - v_2(s)\|_H ds \ + \|m_{0,1} - m_{0,2}\|_H$$

where L_K is constant, v_1 and v_2 are two distinct functions with initial conditions $m_{0,1}$ and $m_{0,2}$, respectively.

We then define two functions

$$b_v(t) = B(m_v(t), h_v(t))$$

$$d_v(t) = D(m_v(t), h_v(t))$$

so that

$$b_v \geq 0$$

$$|b_v + d_v| \leq M_K$$

$$|b_v(t+h) - b_v(t)| + |d_v(t+h) - d_v(t)| \leq N_k|h|$$

For two different functions v_1 and v_2, and their sets of initial conditions $(m^1_{j,0}, h^1_{j,0})$ and $(m^2_{j,0}, h^2_{j,0})$, we find the following estimation

$$\|b_{v_1}(t) - b_{v_2}(t)\|_H + \|d_{v_1}(t) - d_{v_2}(t)\|_H \leq C\left(L_k \int_0^t \|v_1(s) - v_2(s)\|_H ds\right) + \sum_{j=1}^{N} (\|m^1_{j,0} - m^2_{j,0}\| + \|h^1_{j,0} - h^2_{j,0}\|)$$

where C is constant. We then rewrite the eq. 4.9 as

$$\tau \frac{\partial u}{\partial t} = \lambda^2 \frac{\partial u}{\partial x^2} - b_v u + d_v + J(t) \tag{4.11}$$

The **continous dependence on the data** is thus proved.

In order to prove the local existence of the equation system (4.8), where $W = L^2(0,T;V) \cap H^1(0,T;H)$, we assume that the operator $Q : W \to W$ is defined as

follows: for a function $v \in W$, we firstly find the solution (m_v, h_v) of the gating equation. We then find b_v and d_v, together with the solution $\bar{v} \in W$ of the linear equation (4.11) that is $\bar{v} = Q(v)$. It is possible to find a time T so that the operator Q is a contractive function, so its fixed point is a local solution of the nonlinear problem. In order to find a global solution, we extend the local solution by a simple way, as in the case of a set of ordinary differential equations. The **the existence of the solution** is thus proved.

Finally, taking into account all these findings, we conclude that **the problem is well-posed in terms of Hadamard**.

4.4 A mathematical model for soma and neurites

As noted by Rall [142], there is not a unique way to model the dendrites. There are indeed many different ways, each addressing different aspects of the same problem. Each modeling approach may be hence useful under specific assumptions and circumstances but not under others. This certainly regards the passive cable models, which have been developed to investigate the roles of dendritic branching, tapering, and spines, and passive voltage spreading throughout the neuron.

Likewise in Evans (2000) [138], we consider a nonlinear version of the *Rall's single cylinder model*. This provides the basis to approximate a dendritic tree to a multi-cylinder morphology, if the dendritic tree is simmetric (see e.g. [144]). Fig. 4.3 shows this transformation.

The voltage spread throughout the ith neurite as described by the following nonlinear cable equation

$$\tau_i \frac{\partial u_i}{\partial t} = \lambda^2 \frac{\partial^2 u_i}{\partial x^2} - u_i - \sum_{j=1}^{N_i} \bar{g}_{ij} m_{ij}^{s_{ij}} h_{ij}^{q_{ij}} (u - E_{ij}) + J_i(t), \, in \, (0, L_i) \times (0, T) \quad (4.12)$$

where $M \geq 1$ is the number of neurites connected to the cell body, L_i is the length of the equivalent cylinder with $i = 1, 2, \ldots, M$, taking an arbitrary time $T > 0$ and with $u_i : (0, L_i) \times (0, T) \to \mathbb{R}$. The initial conditions are $u_i(x, 0) = u_{i,0}$, $x \in (0, L_i)$, $i =$

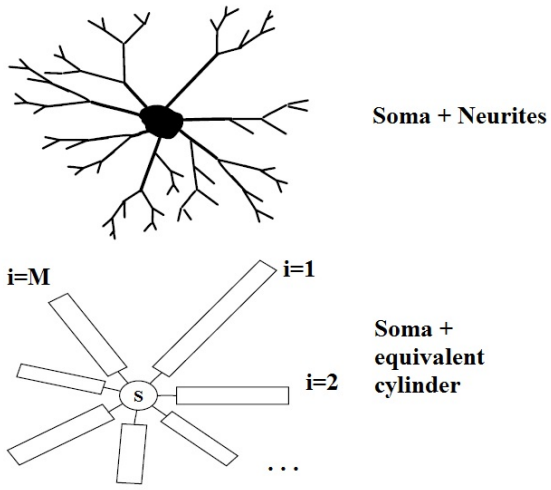

Fig. 4.3 Transformation made in the development of model of branching complexity. Under certain symmetry assumptions each dendritic tree can be represented by an equivalent cylinder giving the equivalent multi cylinder model.

$1,...,M$. We thus assume a neurite to be as a one-dimensional continuum entity in $[0,L_i]$, where the junction point between the cell body and a dendrite is at $x = 0$, while the dendritic terminal is at $x = L_i$ and has free end. Moreover, as all dendrites are connected to the soma, the following $M-1$ boundary conditions have to be satisfied

$$u_1(0,t) = u_2(0,t) = \ldots = u_M(0,t), t \in (0,T).$$

Because of the Kirchoff' law, at $x = 0$, we have the following conservative equation, u_s describing the somatic voltage

$$u_s + \tau_s \frac{du_s}{dt} - \sum_{i=1}^{M} a_i \frac{\partial u_i}{\partial x}(0,t) = R_s I_s(t), t \in (0,T)$$

where a_i are positive constants fixed a-priori and related to the conductance of neurites, $I_s(t)$ is a current injected into the soma.

It remains to define all conditions for the dendritic free ends. We then assume the homogeneous Neumann conditions

$$\frac{\partial u_i}{\partial x}(L_i,t) = 0, t \in (0,T),\ i = 1,...,M$$

Each cable equation is coupled with an equation set of gating variables

$$\begin{aligned} &\tfrac{\partial m_{ij}}{\partial t} = \alpha_{ij}(u)(1-m_{ij}) - \beta_{ij}(u)m_{ij},\ m_{ij}(x,0) = m_{ij0}(x); \\ &\tfrac{\partial h_{ij}}{\partial t} = a_{ij}(u)(1-h_{ij}) - b_{ij}(u)h_{ij},\ h_{ij}(x,0) = h_{ij0}(x). \end{aligned} \tag{4.13}$$

The analysis of the linearized case for multi-cylinder model was developed in [136] and [137], in which one assumes that u_s does not variate. One could proceed likewise in the single nonlinear cable equation, introducing the space functions

$$\mathbf{H} := \mathbf{L^2}(\mathbf{0},\mathbf{L_1}) \times \ldots \times \mathbf{L^2}(\mathbf{0},\mathbf{L_M})$$

$$\mathbf{V} := \{\mathbf{u} = (\mathbf{u_1},...,\mathbf{u_M})\ :\ \mathbf{u_i} \in \mathbf{H^1}(\mathbf{o},\mathbf{L_i}),\ \mathbf{u_i}(\mathbf{0}) = \mathbf{u_j}(\mathbf{0})\ \textbf{for}\ \ \mathbf{i},\mathbf{j} = \mathbf{1},...,\mathbf{M}\}.$$

It is then possible to define an operator

$$Q : H^1(0,T;\mathbf{H}) \cap \mathbf{L^2}(\mathbf{0},\mathbf{T};\mathbf{V}) \to \mathbf{H^1}(\mathbf{0},\mathbf{T};\mathbf{H}) \cap \mathbf{L^2}(\mathbf{0},\mathbf{T};\mathbf{V})$$

similarly to single nonlinear cable equation. However, the linearized case is modeled by a set of M linear parabolic equations that are coupled to one boundary condition.

Remark. In order to make involved the NMDA receptors during synaptic inputs, one can assume a nonlinear relationships between current and patched voltage,

$$\frac{\partial u}{\partial x}(L,t) + g(u(L,t)) = 0, t \in (0,T),$$

where $g : \mathbb{R} \to \mathbb{R}$ is a continuous function, experimentally obtained by voltage clamp.

Part III

The 3D model of the olfactory bulb

Chapter 5

The 3D model of the olfactory bulb

The OB seems to be exquisitely tailored to be reproduced by a large scale 3D model. This is useful to analyze how its spatio-temporal dynamics produce the odor representation with complex natural odors [53]. Thus, we have built up the first 3D realistic large scale model of the OB. This makes experimentally testable predictions on distributed processing of the odor input, introducing a powerful approach of general applicability for investigating the functions of brain microcircuits.

5.1 Starting up the 3D model

We start by illustrating the patterns of glomerular activation in the dorsal surface of the OB that are used in our model. Briefly, Fig. 5.1A (top) illustrates the experimental setup used to record these patterns of glomerular activation. Below is the laminar organization of the OB. Particularly, the glomerular activity levels were recorded by optical intrinsic imaging during the delivery of odor stimuli and clearing with aspiration [53]. This provided the activity levels of 127 glomeruli distributed in the dorsal area, evoked by the presentation of 20 natural odors (Fig. 5.1B). Typical intrinsic optical signal imaging of evoked activity during presentation of coffee and kiwi is shown in Fig. 5.1C. This experimental data was used to simulate the odor input in our model of the OB.

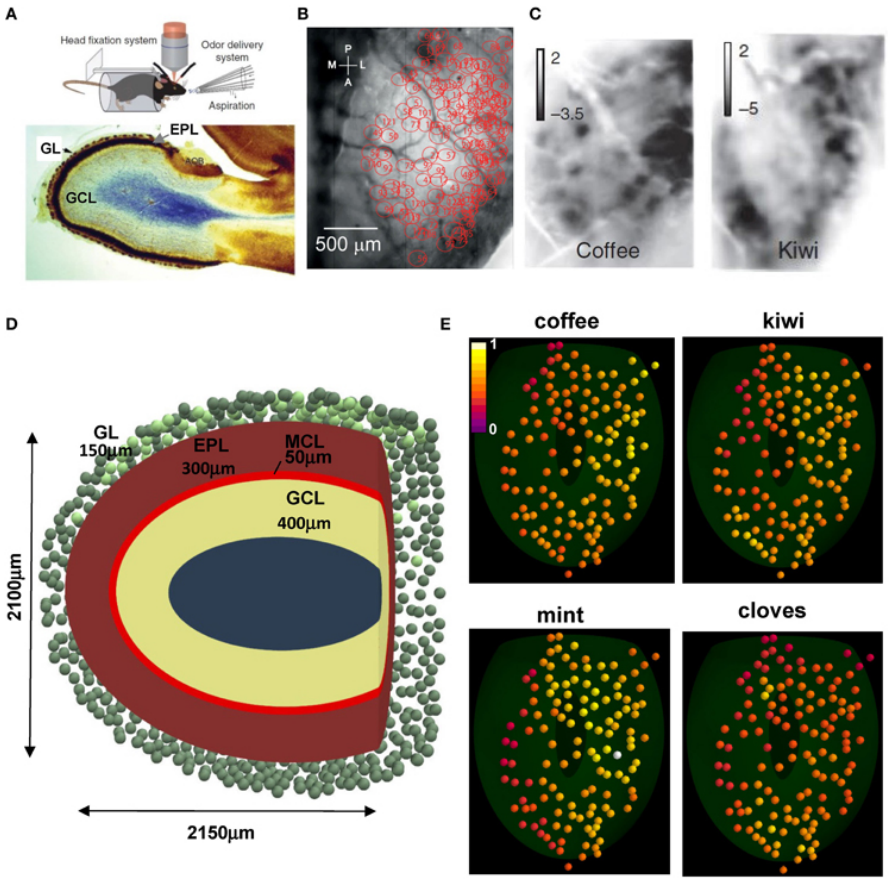

Fig. 5.1 Experimental data of glomerular activation [38].

To relate our model of the glomerular patterns to the deeper MC-GC network, we made a model of the laminar organization as shown in Fig. 5.1B. This shows a tangential sagittal section of the OB model (similar to Fig. 5.1A, bottom), which we built as a truncated ellipsoidal shape of 1050 and 1200 μm semi-axes. This size is consistent with the adult mouse OB (as prof. G. Shepherd observed). To estimate a reasonable distribution of glomeruli, a full set of 1800, 100 μm diameter, glomeruli was initially randomly distributed in a 150 μm thick GL (green spheres); 127 of them, in the dorsal part (Fig. 5.1D, light green spheres on the top) were mapped to those studied experimentally, based on their 2D position (shown in Fig. 5.1B). Their

spatial location on the OB surface implicitly determined the position of the 635 MCs soma (5 per glomerulus) used in our model, which were randomly distributed in the 50 μm thick MCL within an area approximately below ($\pm$ 100 μm diameter) the glomerulus to which they projected their tuft. Unless explicitly noted otherwise, in a typical network approximately 120,000 GC bodies were randomly distributed inside a 400 μm thick GCL. Each projected a single radial dendrite into the 300 μm thick EPL. Approximately 70,000 of them were connected to the MC lateral dendrites. Typical glomerular normalized activation patterns by several different natural odors are shown in Fig. 5.1E. These illustrate several important features of the odor patterns. First, some patterns are quite extensive, as in mint; others are more restricted, as in cloves. Second, the extent of activation ranges from a high to low intensity, as in mint, to a limited range of intensity, as in kiwi. Finally, the specific sites and degrees of activated glomeruli are overlapping but different, consistent with virtually all studies and with the original finding and hypothesis that the different patterns can contribute to discrimination of different odors [99]. This provides a model of the input patterns of glomerular activation that can be applied to any arbitrary pattern. In addition, it sets up the framework for relating any input pattern to the corresponding pattern of activation of the MC-GC network. These data were directly used to drive the MC-GC network activity.

5.2 The algorithm for generating synthetic mitral cells

There are many methods available for generating realistic neurons, but only two are actually used: one is Cuntz's method [67] and other is L-NEURON [121].

By the first method, dendrites are generated as a minimum spanning tree connecting a cloud of points (i.e. carrier point), of which coordinates are randomly generated. The spatial distribution of the carrier points is directly estimated from neuron reconstructions, to ensure that the synthetic neurons have got realistic morphologies. Even though this method is general, it has some shortcomings. First,

estimating the spatial distribution of carrier point requires an intricate resampling of the dendritic trees. Second, in order to achieve a good accuracy, this distribution should be estimated over a large number of neuron reconstructions, whereas we only had 8 MC real reconstructions [76]. Third, the method itself holds a certain degree of empirism in choosing the number of carrier points, which grades the numbers of branches and the total dendrite length of generated neurons [120]; by choosing a wrong number of them, one therefore risks to generate unrealistic neurons, with biased morphological features.

The second method, L-NEURON, was not useful to generate MCs. It indeed required to be extended to let the dendrites growing and curving as the EPL boundary surface. However, adding such functions to L-NEURON would be not convenient, since it could require a long coding.

In light of these reasons, we did not use any of these methods for generating synthetic MCs. Rather, we have preferred to design a new general method based on *random walk*. The full algorithm for generating realistic neurons is described in the Appendix A.

5.2.1 The random walk

In order to generate the lateral dendrites of MC, we developed an extended version of *biased and correlated random walk* [119]. Random walk mimicks the movements of real biological process or system, reproducing growing and branching structures with realistic variability. Particularly, our version of random walk embeds branching and stop growth conditions that are governed from probability distributions. In order to guarantee the realism of the synthetic neurons, we estimated all these distributions from real MC reconstructions, as described in section 5.2.3.

A random walk can be seen as a sequence of steps, each described by spherical coordinates. Given the ith step, its direction is described by two angles, θ_i and ϕ_i, which are the azimutal and the polar angles, respectively. The direction of the $i+1$th

step is then

$$\begin{aligned} \theta_{i+1} &= \tilde{\theta}_i + \Delta\theta \\ \phi_{i+1} &= \tilde{\phi}_i + \Delta\phi \end{aligned} \tag{5.1}$$

where $\Delta\phi$ and $\Delta\theta$ are the random components, and are randomly picked for each step. $\tilde{\theta}_i$ and $\tilde{\phi}_i$ are coordinates of the preferential growth direction, obtained as function of the previous direction by applying the *bias* (see section 5.2.2). Particularly, the bias makes the lateral dendrites curving as the EPL boundary surfaces. It is calculated at each step and depends on the space boundaries and the current spatial position. Moreover, the direction of a given step is correlated with the previous one. The influence of the initial direction fades over a substantial number of steps, because of the combined effects due to the bias and $\Delta\phi$ and $\Delta\theta$.

5.2.2 The bias

The bias controls the growth direction of dendrites, approximating the effect of the membrane enzymes that drives the dendritic growth [122, 123]. The bias therefore needs to be defined in accord to a specific neuron type.

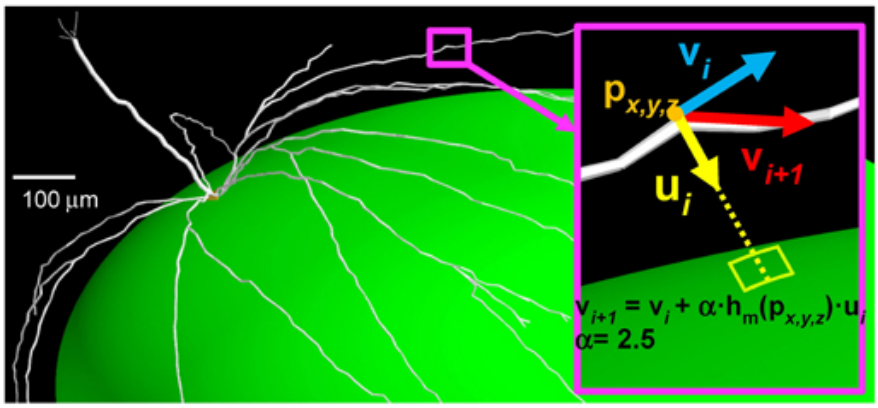

Fig. 5.2 The correction factor applied for lateral dendrites of mitral cell [38].

The bias we have defined for MC lateral dendrites is inspired by the force of gravity (Fig. 5.2). It indeed operates a resistance against the growth direction that is graded with its centrifugal component, and its intensity increases with the distance from the lower boundary surface of EPL. Of course, we use a mathematical formalism to describe the bias.

The distance from the low EPL surface is:

$$h(\overline{p_i}) = \sqrt{\sum_{j=1}^{3} \left(\frac{p_{i,j} - c_{i,j}}{R_j} \right)^2} \tag{5.2}$$

where $\overline{p_i}$ is the position reached at i-th step, $\overline{c}$ is the position of the OB center, R_1, R_2, R_3 are the axis of a hypothetical ellipsoid that approximates the lower boundary surface of EPL. By using the h distance function instead of the euclidean one, the distance is normalized, eliminating the distorsion due to the ellipsoid eccentricity. Obviously, the value of h increases with the distance from the OB center $\overline{c}$. It is higher than 1, equal to 1, and less than 1, when $\overline{p_i}$ is located beyond the EPL upper surface, on the EPL upper surface, and within the ellipsoid surface, respectively.

Given the preferential growth direction $\overline{v_i}$, we consider a hypothetical point $\overline{p_i'}$ obtained by extending the dendrite from $\overline{p_i}$ along $\overline{v_i}$:

$$\overline{p_i'} = \overline{p_i} + L \cdot \overline{v_i}$$

where $\overline{v_i}$ is the ith growth direction (described by spherical coordinates θ_i and ϕ_i as shown in eq. 5.1). The bias is then

$$\overline{b_i} + \begin{cases} \overline{v_i} + \alpha \cdot h(\overline{p_i}) \cdot \overline{u_i} & \text{if } h\left(\overline{p_i'}\right) > h(\overline{p_i}) \\ \overline{0} & \text{otherwise} \end{cases}$$

where L is the step length, α is the bias intensity factor, $\overline{u_i}$ is the bias direction that is perpendicular to the boundary surface. The first condition tests whether the preferential growth direction is centrifugal, while the equation beside describes the gravity-like bias. Finally, the new preferential growth direction is

$$\overline{v_{i+1}} = \overline{v_i} + \overline{b_i}$$

which is described by spherical coordinates $\tilde{\theta}_i$ and $\tilde{\phi}_i$ (eq. 5.1).

5.2.3 Parameter and distributions estimation

In order to carry out the parameters and probability distribution estimation, we have analyzed 8 reconstructed MCs [76]. The raw morphology files were first rotated along their principal axis. To calculate the spatial direction of a dendritic section, the raw data points composing the dendrites were resampled in 20 μm segments, as schematically illustrated in the top left of Fig. 5.3B. Since the spatial orientation of each section was expressed in spherical coordinates (Fig. 5.3B, bottom), the direction of a new dendritic segment was randomized according to the probability distribution function for the relative displacement in the spatial orientation of two consecutive membrane sections, $\Delta\theta$ and $\Delta\phi$ bar graphs in Fig. 5.3B, right. The observed values for $\Delta\phi$ and $\Delta\theta$ were reproduced by the Laplace distributions $pdf(\Delta\phi) = 3.125 \cdot e^{-|\Delta\phi|/0.16}$ and $pdf(\Delta\theta) = 3.57 \cdot e^{-|\Delta\theta|/0.14}$, respectively. Their parameters were found by a maximum likelihood method, and resulted in a statistically significant reproduction of the data. Since the main focus has been on the lateral dendrites, three additional main characteristics were analyzed in detail (schematically indicated in Fig. 5.3A, right): the path lengths, the branch lengths, and the probability for each branch order (defined as the number of bifurcations from the cell body). The observed distributions of these features are shown in Fig. 5.3C. The path and branch length distributions were generated using a Gaussian (μ = 838, σ = 238) and an exponential function (μ=227), respectively, which gave a statistically significant reproduction of the experimental data (χ^2 test, p = 0.269 and p = 0.292, respectively). The probability for each branch order was directly applied during the growth process.

For each synthetic MC, the shape of the soma was randomly chosen from the 8 reconstructions. A random number of (4-9) lateral dendrites arose from the soma

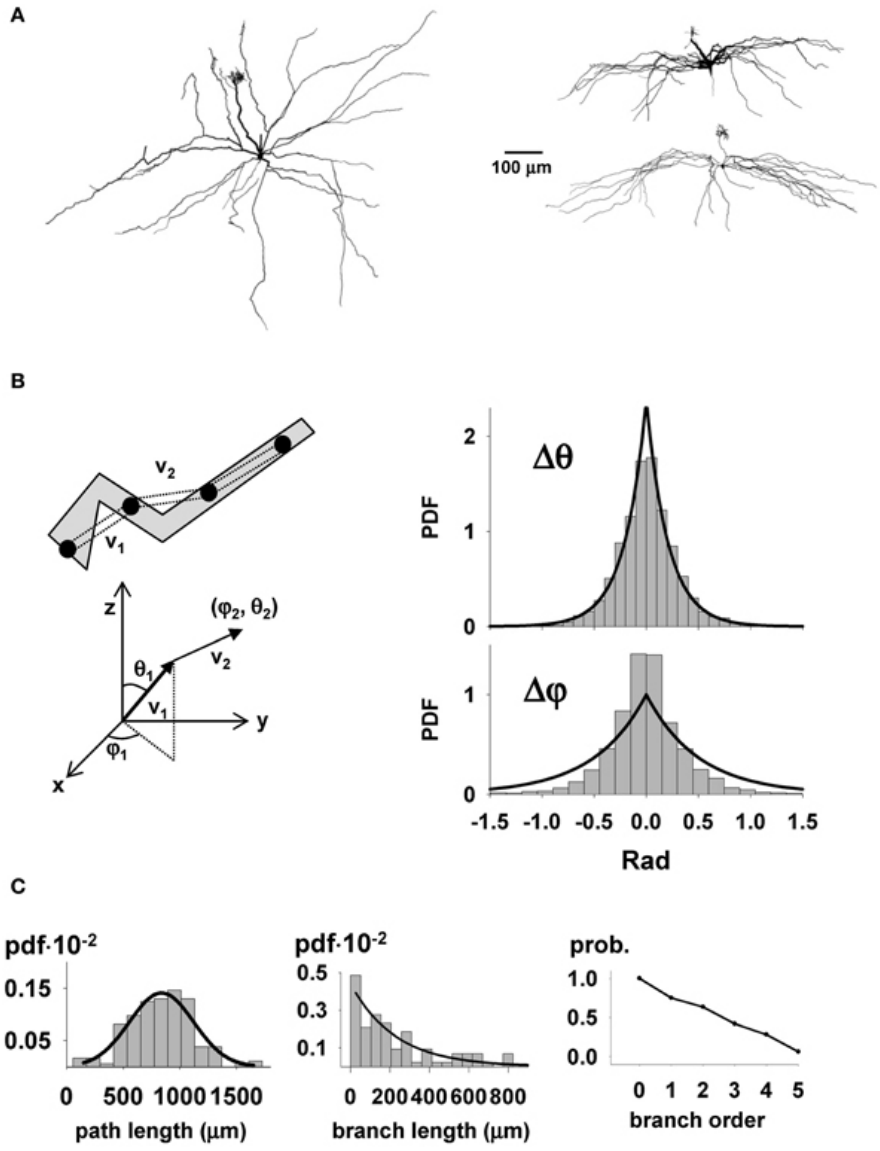

Fig. 5.3 Statistical parameters of full mitral cell 3D reconstructions [38].

with an initial random diameter, D_i, of 3-5 μm, tapering with distance from the soma as $D_i - 2.6 \cdot exp(-0.0013 \cdot d)$ to a minimum of 0.3 μm. For the apical and tuft dendrites, we used data from the reconstructions and the constraints of our laminar model of the OB to set the range of values for diameter and length, which were also

constrained to reproduce several experimental findings on the electrophysiological properties for MCs [64, 69]. Briefly, non-bifurcating apical dendrites were modeled with 4-5 μm diameters and a length in the range of 420-520 μm (depending on the relative glomerulus location). To take into account the tuft morphology, a random number (between 4 and 6) of 0.8 μm diameter dendrites (40-60 μm long) were added at the tip of the apical dendrites.

5.2.4 The realism of the synthetic mitral cells

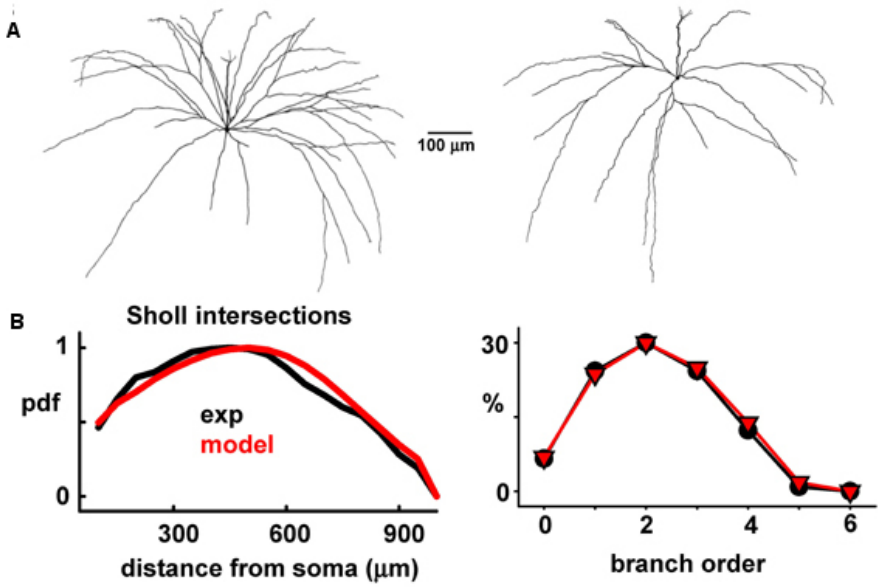

Fig. 5.4 The synthetic mitral cells are statistically indistinguishable from real reconstructions [38].

The final result is shown for two typical cells in Fig. 5.4A. A Sholl plot [89], typically used to compare the statistical properties of dendritic tree extension [67], is arranged to test the quality of the synthetic reconstructions. This type of plot (Fig. 5.4B, left) reports the number of dendrites intersecting with the surface of a sphere centered at the soma, as a function of the sphere radius. An additional

independent test was given by the proportion of dendrites of a given branch order (Fig. 5.4B, right). Both plots show the close correlations between experimental and model morphologies, which were statistically indistinguishable (Wilcoxon Signed Rank test p = 0.229 for the Sholl Plot and p = 0.313 for the branch order).

5.2.5 A possible generalization

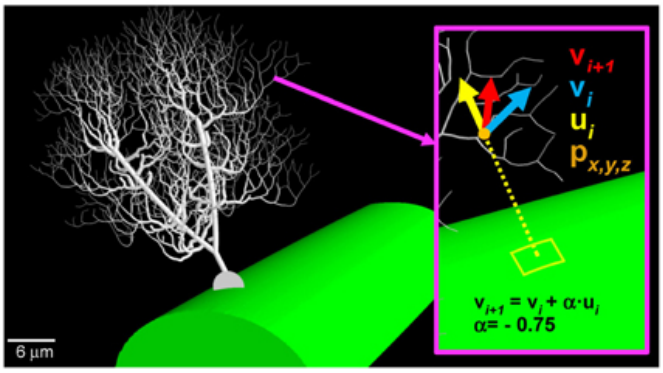

Fig. 5.5 The synthetic purkinje cells generated by the same procedure used to build synthetic mitral cells [38].

This approach thus gave a close approximation of modeled cells to experimental data. This method is completely general. An example of its application to the case of a cerebellar Purkinje cell is shown in Fig. 5.5. In this case, the correction factor for growing the dendrites in the appropriate (molecular) layer was directed vertically, toward the surface (compare u_i in Fig. 5.5 and 5.2).

5.3 The mitral and granule cell membrane properties

In this section we describe the properties of the MCs and GC that form the model network. For MCs, uniform passive properties were used, with Ra = 150 $S \cdot cm$, and

τ_m = 7 ms, in agreement with recent experimental findings [85] at physiological temperature. All passive and active properties, already validated against experimental findings, were taken from our previous model [62]. Briefly, in MCs, Na-, K_A-, and K_{DR}-type conductances were uniformly distributed over the entire dendritic tree. In GC, Na, and K_A channels were distributed throughout whereas K_{DR} was present only in the soma, with resting potential set at -65 mV for all cells.

One important characteristic of the modeled MCs was the total dendritic length of approximately 10,000 μm which determined the extent of interactions with GC. Another feature directly related to the cell excitability was the input resistance, which peaked at approximately 20 MΩ. These characteristics were in accord with experimental findings [13, 75]. Two other important properties for odor processing are the latency of the first spike in response to odor input [77], and the firing rate [47, 90]. This is shown for the model of a typical cell in Fig. 5.6A bottom, for a single simulated sniff as a function of the odor concentration, as measured by the total peak synaptic conductance activated on the MC tuft. As in experiments, as the strength increases, the first spike latency decreases and the peak firing frequency increases. The ranges are in agreement with experimental findings [63, 71].

With regard to GC (Fig. 5.6B, top), the total dendritic length was widely distributed. The GC bodies were distributed within the ellipsoidal GCL, which meant that their radial dendrites vary in length as they rise to the EPL, with a consequent variability in their input resistance. Below is shown the average and peak somatic firing frequency during random activation of 50 MC synapses of increasing weights. In this graph, the peak frequency rises with increasing synaptic input as in the MCs, whereas the average frequency is shown reaching a lower level of firing rate, because the input due to the high level of synaptic firing, and corresponding high level of synaptic currents, saturates the granule cell responses in their dendrites.

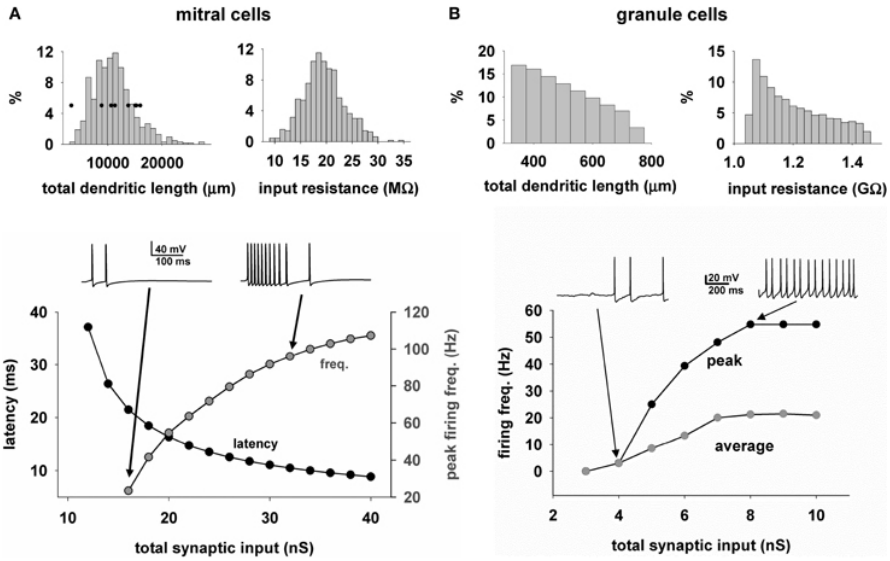

Fig. 5.6 The mitral and granule cell properties [38].

5.4 The mitral and granule cell connectivity

The functioning of the network depends critically on the connectivity between mitral and GC. The key factor providing for the connectivity is the dendrodendritic synapses between the MC lateral dendrites and the spines of the GC in the EPL [87]. The rule that nature uses to establish these synapses during development is unknown. To set up the initial arrangement of the network, we use an algorithm in which we fix the total number of GC in the GCL layer and the average number of synapses for a specific segment of MC lateral dendritic membrane, one synapse for either 2, 10, or 20 μm of length. A schematic illustration of this process is shown in Fig. 5.7A. For each segment of mitral cell dendrite, one granule cell is randomly chosen within a 50 μm rectangular volume inside the GCL (red box in Fig. 5.7A). A spine is then added to the closest granule cell dendritic segment, and a dendrodendritic synapse is formed. As in previous models [40, 62], this synapse contains the same proportion of AMPA and NMDA channels, with the appropriate compartment of MC secondary dendrites containing GABA channels.

The distribution of how many GC would be connected with a given number of mitral cells is shown in the plot in Fig. 5.7A, bottom, for the assumptions of 1 synapse per 2, 10, and 20 μm of lateral dendritic length. It should be stressed this is the connectivity presumably set during development, corresponding to logical connections established between granule and MCs. The actual conductance of each synapse will be dynamically determined by its activity, according to the plasticity rule. Note that for the assumption of 1 synapse per 2 μm length, each granule cell forms on average 2,000 synapses with MCs; with 1 synapse per 20 μm length, the average is 16. This will allow testing simulations covering a wide range of possible connection density.

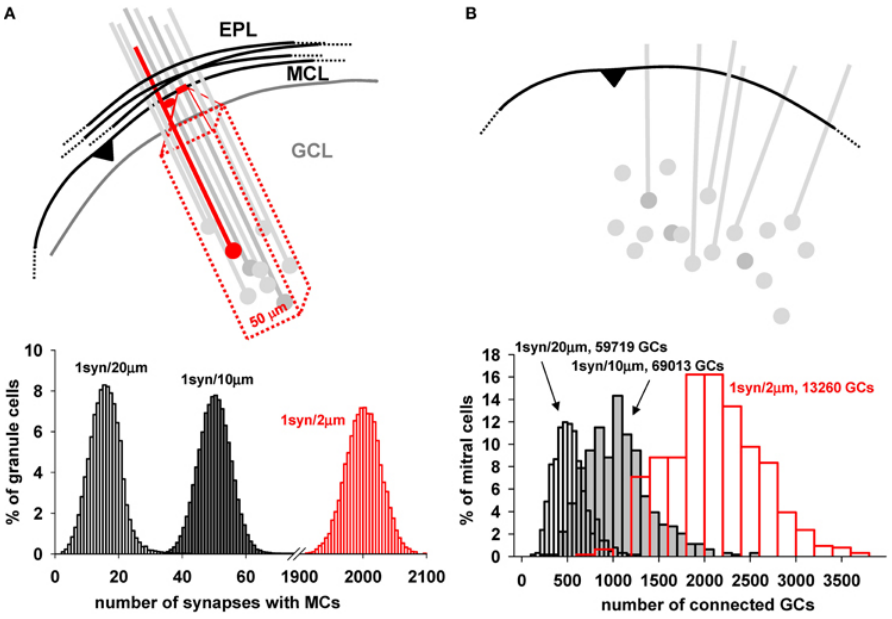

Fig. 5.7 Mitral cell and granule cell connectivity [38].

As a consequence of this connectivity rule, the number of MCs connected to a given number of GC is shown in Fig. 5.7B. Above the diagram shows a single MC with its lateral dendrites, potentially connected to a number of randomly placed GC and their dendrites. Below is plotted the proportion of MCs connected to a

given number of GC, showing that the peak connectivity for a mitral cell could be easily adjusted in such a way to connect, on average, from ≈500 to ≈2000 GC, with a ratio ranging from about 20 to 100 GC per MC. Thus, as can be seen from both plots in A and B, the actual overall density of connectivity can be adjusted in the model, to test presumably corresponding functional consequences. A change in synapse number and connectivity in the EPL during integration of adult-generated GC has been experimentally observed, and suggests that this mechanism can be an important variable for the network operations [92].

5.5 Odor Inputs and Olfactory Receptor Neuron Dose-Response Relations

Information about an odor is contained in the activity of the ORNs, which are organized in functional classes, each expressing a particular receptor [11, 50]. To understand better the input/output operations of the OB, it is thus necessary to have first a physiologically plausible representation of the signal that is delivered to any MC, representing an odor and its concentration. This can be expected to be particularly important for natural odors, which appear to activate many ORN types with a complex spatiotemporal distribution [53]. We start from the experimental findings [12] suggesting that, during a sniff, the axons of a homogeneous population of ORNs converging onto a single glomerulus generate a typical signal with precise temporal pattern dynamics (Figure 5.7A). These axons release glutamate, which excites AMPA and NMDA receptors on the mitral cell dendritic tufts (reviewed in [4]. Importantly, the peak amplitude of this pattern changes with odor identity and concentration, but not its temporal dynamics [130].

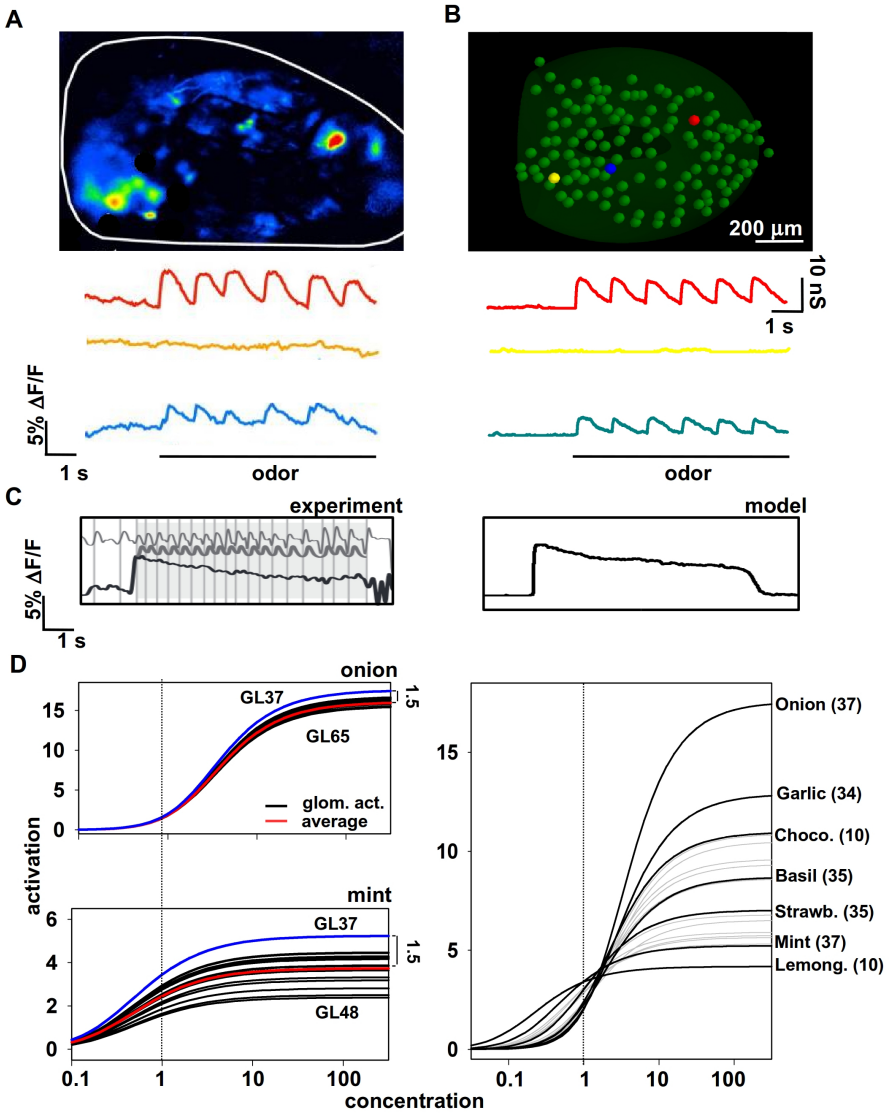

Fig. 5.8 Modeling odor inputs and olfactory receptor neuron activation [105].

5.5.1 Olfactory Receptor Activity

To model the experimentally-observed time course of the excitatory signal conveyed to the dendritic tuft of the MCs, we used a custom modification of the set of ordinary differential equations based on a generic scheme previously used to model synaptic

transmission [15]. In particular, the activation of a homogeneous population of ORN is modeled as

$$S_{ORN}(t) = O(t)(1 - D(t)) \quad t \in [0, T] \tag{5.3}$$

where $O(t)$ and $D(t)$ are the solutions of the following ODEs

$$\begin{cases} \frac{dO}{dt} = K_O(1 - C - O) \\ \frac{dC}{dt} = K_{C_1} C(1 - C) + K_{C_2}(1 - C) \quad t_i \in [0, t_1] \cup ... \cup [t_n, T] \\ \frac{dD}{dt} = K_{D_1} O(1 - D) - K_{D_2} D(1 - O) \end{cases}$$

where t_j is the start time of the j-th sniff. In this scheme, there are three states, open (O), closed (C) and desensitized (D). The O and C states reproduce the rise and decay of the signal during a sniff [12], whereas the D variable implements receptor desensitization which occurs at high sniffing frequency. The initial condition at the beginning of a simulation (i.e. at t=0) are O=0, C=1 and D=0; at each sniff, C is reset to 0. All constants are $K_O = 0.01ms^{-1}$, $K_{C_1} = 0.01ms^{-1}$, $K_{C_2} = 10^{-4}ms^{-1}$, $K_{D_1} = 1.7 \cdot 10^{-4}ms^{-1}$, $K_{D_2} = 0.01ms^{-1}$.

The overall synaptic current [16] generated on the mitral cell tuft dendrites by odor activation was calculated as:

$$I_{syn}(t) = g(t)(V_m(t) - E_{exc}) \quad t \in [0, T] \tag{5.4}$$

where

$$g(t) = \tilde{g} + \overline{g_{max}} \cdot \mathrm{GL}(c) \cdot S_{ORN}(t) \tag{5.5}$$

V_m is the membrane potential, E_{exc} = 0 mV, $\overline{g_{max}}$ the peak conductance, $\mathrm{GL}(c)$ is directly related to the odor identity, concentration, and ORN type (see eq. 5.6, in the next paragraph 5.5.2) and $\tilde{g}$ implements a random (normal) background activity (0 $\pm$ 1 nS) taking into account the physiological fluctuations in olfactory receptor neurons activation. The resulting synaptic conductance time course (eq. 5.3) is shown in Fig. 5.8B for three odor concentrations roughly reproducing the experimentally OB observations shown in Fig. 5.8A. These equations were also able to reproduce typical olfactory receptor neurons response at high sniffing frequency (Fig. 5.8C).

5.5.2 ORN Dose-Response Relations

The equations described above realize a reasonable representation of the synaptic input in a glomerulus in response to an odor at a specific concentration, but we need to represent the responses to an odor as a function of the concentration, i.e., the dose-response curve. We started from the relative ORN activation level for 127 glomeruli (see Fig. 5.1A-C). We have these data for a set of 20 natural odors at one (suprathreshold, but relatively low) concentration [53]. Experimentally, the ORN activity is represented by dose-response curves, which correspond to the peak I_{syn} current generated for each odor concentration. These curves can be expressed as Hill functions, with different parameters for each odor-glomerulus pair. For example, the overall response of the ORNs converging on glomerulus GL_i in the presence of odor U at concentration c, can be expressed as [130]:

$$GL_i(c) = \frac{F_{max}}{1 + \frac{1}{\eta_i^n}\left(1 + \frac{K_i}{c}\right)^n} \quad i = 0, ..., N_G \tag{5.6}$$

where n is the Hill coefficient, F_{max} is the maximal response, η_i is the transduction efficiency for odorant U and $N_G + 1$ is the number of glomeruli. The asymptote of each $GL_i(c)$ is

$$asy_i = \frac{F_{max}}{1 + \frac{1}{\eta_i^n}} \tag{5.7}$$

and the concentration of odor U at half maximun response is $\frac{K_i}{\sqrt[n]{2+\eta_i^n}-1}$.

In order to compare and analyze the response to different odors we need the odor-response curve for each of our odor-glomerulus pair. We started from the relative ORN activation level for 127 glomeruli. We have these data for a set of 20 natural odors at one (suprathreshold, but relatively low) concentration [53]. Since this information is not experimentally available, the next step is thus to implement these curves from suitable assumptions for all the parameters. For example, experimentally, the Hill coefficient, n, is quite variable, in the range $[0.1, 18]$ [128, 130], and F_{max} can be considered to be an intrinsic neuronal property related to the maximum activity that can be generated by any given ORN. For simplicity, in this paper we

fixed their value to 2 and 25, respectively, for all cases. From the raw data [53] we have the GL_i for all of our odor-glomerulus pairs at a single concentration. We call this concentration c_V and assume c_V=1. For η_i (modulating the maximal response at high concentrations) and K_i (related to the concentration at which there is half-maximal activation), there are several experimental findings [128, 130, 55], showing that each odor-glomerulus pair can exhibit an apparently arbitrary combination of these parameters. To derive their values, it would be necessary and sufficient to find two independent equations for each odor-glomerulus pair. We determined these equations as follows. Assuming without loss in generality c_V=1, for each odor U from eq. 5.6 we olfactory bulbtain

$$\rho_i(c) = \frac{F_{max}}{1 + \frac{1}{\eta_i^n}(1+K_i)^n} \quad i = 0, ..., N_G \tag{5.8}$$

Let us define $\rho_{max} = \max_{i=0,...,N_G} \rho_i$. We assume that in all cases the asymptotic value of the response is proportional to the value at c_V, i.e.

$$asy_i = \alpha_U \frac{\rho_i}{\rho_{max}}$$

where

$$\alpha_U = \max_{i=0,...,N_G} \frac{F_{max}}{1 + \frac{1}{\eta_i^n}}$$

is also the asymptotic value of the dose-response curve for the odor-glomerulus pair with the highest input at c_V, i.e., $GL_h(c_V) = \rho_{max}$. To determine α_U we must define a range of possible values of asymptotic response (asy_i) for each glomerular input. From preliminary simulations, we empirically found that the minimum value of asymax to form a column is approximately 1.5 greater than the average value of asy_i. Thus, to ensure that all odors would eventually be able to form a column, if presented at a concentration high enough, we imposed that:

$$asy_{max} = \frac{1}{N_G + 1} \sum_{i=0}^{N_G} \frac{F_{max}}{1 + \frac{1}{\eta_i^n}} = \beta$$

With β = 1.5. After standard algebraic manipulations we olfactory bulbtain that

$$\alpha_U = \frac{\beta}{1 - \frac{1}{N_G+1}\sum_{i=0}^{N_G}\frac{\rho_i}{\rho_{max}}}$$

Finally, we can determine the (positive) η_i and K_i for all odor-glomerulus pairs by solving the system:

$$\begin{cases} \frac{F_{max}}{1+\left(\frac{1+K_i}{\eta_i}\right)} = \rho_i \\ \frac{F_{max}}{1+\frac{1}{\eta_i^n}} = \beta\frac{\rho_i}{\rho_{max} - \frac{1}{N_G+1}\sum_{i=0}^{N_G}\rho_i} \end{cases}$$

With β = 1.5, the above system admits positive solutions for all odors.

Following the procedure described here, we were able to write a set of Hill functions representing the dose-response curves for a given odor. It is important to stress that, to derive these (experimentally unknown) curves for the response of different glomeruli to the same odor, we used the assumption that the relative ratio of their asymptotic value is the same as that at the reference concentration (c_V). This constraint is important because it reproduces the progressive recruitment of glomeruli often observed experimentally for increasing odor concentration [49]. Two typical examples of odors (mint and onion) are shown in Fig. 5.8D (left), and the resulting dose-response curve of the most active glomerulus for each odor is shown in Fig. 5.8D (right). It should be noted that concentration in these plots is reported in arbitrary absolute units. Only the relative overall action is important, measured in terms of the peak synaptic conductance that will be activated in the mitral cell tufts to model an odor presentation. Taken together these results suggest one of the possible approaches to extrapolating missing information about odor inputs using the available data and suitable constraints.

Chapter 6

The column formation and odor learning

The OB is organized in computation units, called GUs, that can interact through the MC-GC circuit. Such interaction may even occur during learning, so conditioning the configuration of the OB network in terms of sparse and segregated GC columns [58, 29].

Understanding the neural basis of odor learning is difficult or impossible in experiments, therefore it can be conveniently explored using our realistic computational model of OB [38]. Here, we have analyzed the synaptic interactions between GUs through the MC-GC circuit. They have been related to the column shape, which has been demonstrated to be affected from interaction between GUs. The interacts can be negative or positive, whereas learning has been demonstrated to be a non-commutative operator.

6.1 The validation of the model

We began by identifying experimental findings as a basis for validating our 3D model of the OB. Single clusters in the OB were obtained from a pseudorabies virus staining pattern after a single injection [58] (Fig. 6.1A, green spots in the GCL), each cluster belonged to a single GU. We assume that these green spots indicate GCs with active synapses on MCs at spatially segregated locations on their lateral dendrites. It has been observed that the number of GCs involved in a column varies

with distance from its center (Fig. 6.1A, bottom), and it was also demonstrated (Fig. 6.1B) that MCs belonging to the same glomerulus form connections with different subsets of GCs [29] and make connections through their lateral dendrites with GCs belonging to different GUs (yellow spots within columns in Fig. 6.1B).

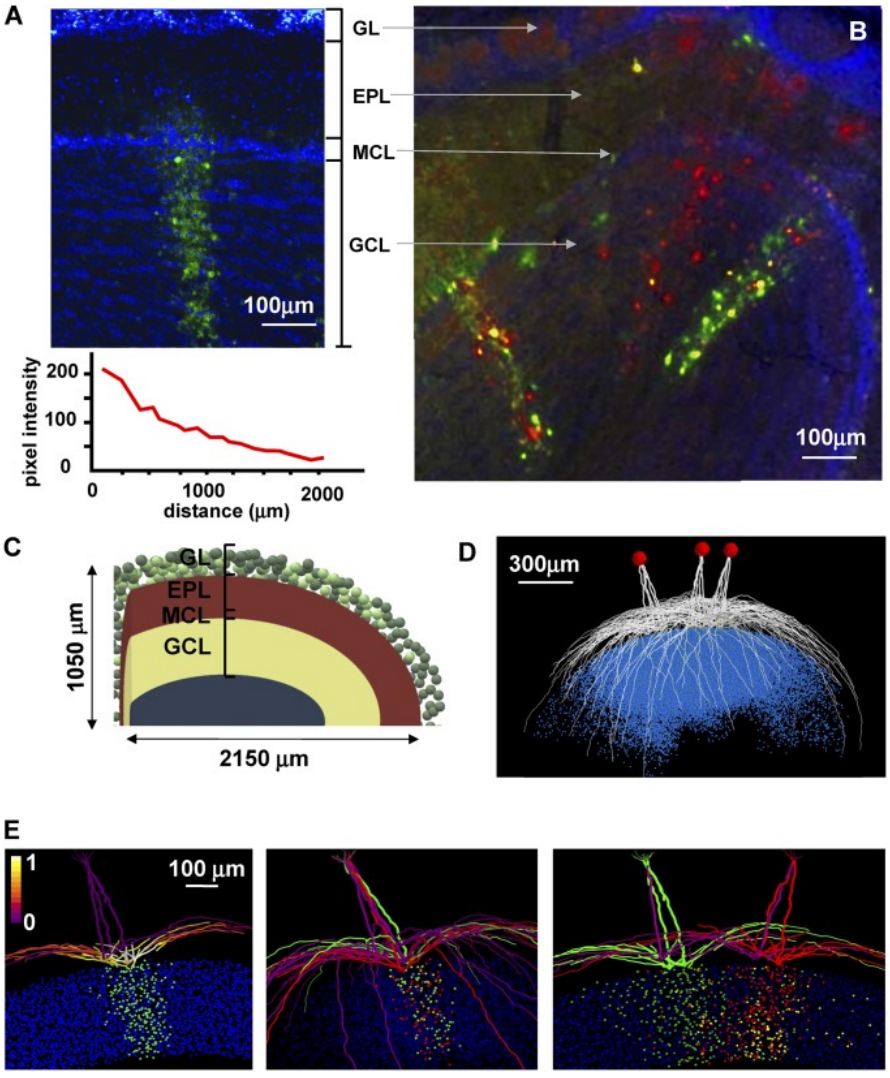

Fig. 6.1 The 3D model can reproduce single- and multicolumn formation, as observed in the experiments. [39].

In order to validate our model against these experimental findings, we ran a simulation in which a relatively strong input was presented to one glomerulus (glomerulus 37) for a simulation time long enough to allow the synaptic weights to reach equilibrium values (7 s). The final weight configuration is shown in Fig. 6.1E, left. To make a clearer comparison with the experimental data (Fig. 6.1A), we visualize the cells contained in a 200-μm-thick section centered on the glomerulus. MC lateral dendrite segments were color-coded for the peak (normalized) inhibitory inputs they receive from GCs. Green-colored points represent GC somas in which at least one synapse was strongly potentiated more than 95% of its peak value. A clear column can be distinguished that is very similar to those observed experimentally (Fig. 6.1A), which also exhibit different widths and cell densities (Fig. 6.1A, bottom plot). If we model a double injection in two of the MCs of the same glomerulus (red and green in Fig. bottom plot of E, middle), we observe that they form connections with different sets of GCs (red and green dots below the glomerulus), according with experimental findings [29]. Finally, a double injection in two different glomeruli (Fig. 6.1E, right), after a simulation activating two neighboring glomeruli, reveals the presence of lateral synaptic connections between MCs, through GCs, belonging to different glomeruli (Fig. 6.1E, right, yellow dots in the GCL), according with experimental findings [29] (Fig. 6.1B). These results therefore show the model can reproduce the basic experimental observations for single- and multiple-column formation.

6.2 Column results of a balance between excitation and inhibition

Previous model predicted the synaptic plasticity is the key mechanism for column formation [80]. This particularly occurs in the dendrodendritic reciprocal synapses connecting MCs and GCs (see chapter 1), where both excitatory and inhibitory synapses incur in potentiation or depression as function of the firing rate

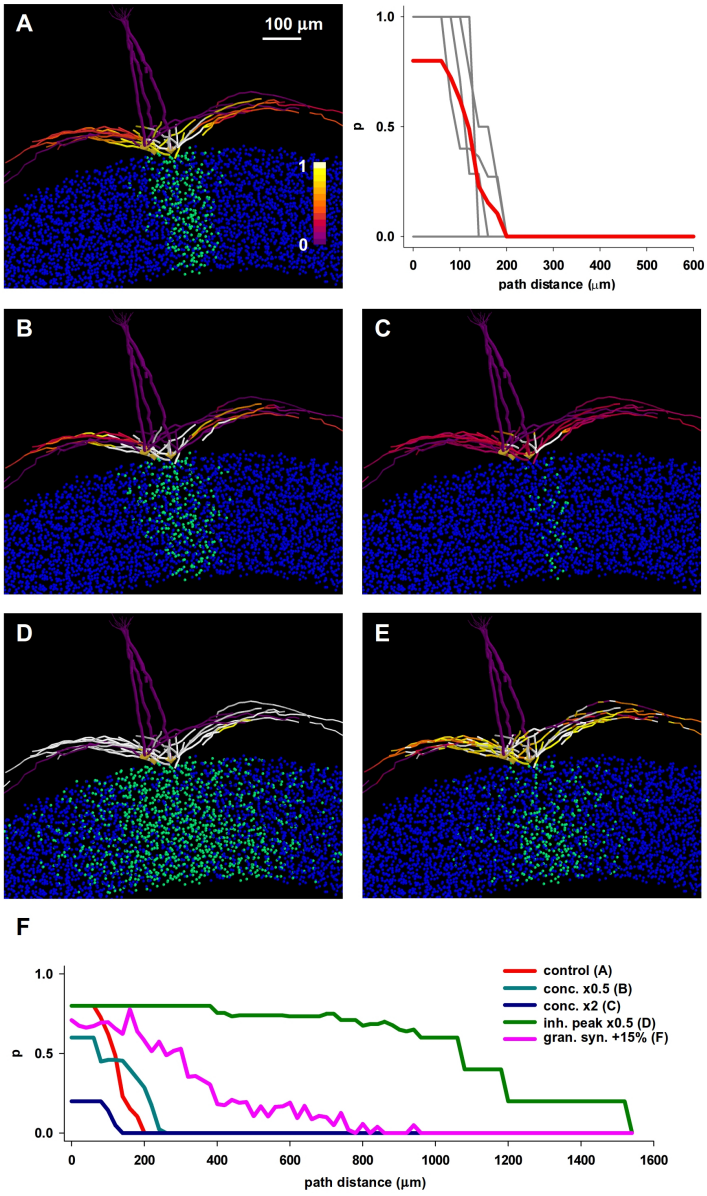

Fig. 6.2 The formation of an isolated column requires a relatively strong input, a large number of GCs, and mitral-granule synapses with a balanced excitation/inhibition ratio [39].

[17, 34, 20, 7]. Odor learning may therefore cause the synaptic plasticity, and so the column formation.

Plasticity in these dendrodendritic synapses may be activated by action potentials backpropagating in the MC lateral dendrites, which thereby evoke the response in the connected GC; the GC in turn inhibits the MC locally as feedback. The backpropagation proceeds from the cell body toward distal lateral dendrites. It can be then blocked by the inhibition due to the GC feedback, especially if the inhibitory synapses are significantly potentiated. Such inhibition then decreases the number of backpropagating action potentials with the distance from the cell body, so decreasing the firing rate in the more distant lateral dendrites. Here, the reciprocal synapses remain hence weakly potentiated. Such dynamic underlies the typical structure of the GC column (Fig. 6.2A, left), where the inhibitory synapses are strongly potentiated in proximity of the cell body, while the more distant ones remain weak (Fig. 6.2A, right). This configuration is assumed as control. Taking into account this dynamic, the GC column results of a balance between inhibition and excitation.

We have therefore investigated how the GC column shape is dependent on this balance. This can be altered by changing the excitatory and inhibitory conductance peaks in the reciprocal synapse, together with the input conveyed on MC tuft dendrites. By reducing the input to half of control (Fig. 6.2B), even the firing rate decreases in the MCs, as well as in the connected GCs. The proximal synapses are therefore less potentiated, so the formed column appears to be spare. Conversely, by increasing the input to double of control (Fig. 6.2C), the firing rate increases in both MCs and GCs. Thus, the GCs respond with such a feedback that overwelmes completely the backpropagation, then the column cannot be formed. By decreasing the inhibitory conductance peak to half of control (Fig. 6.2D), the action potentials overly backpropagate in the MC lateral dendrites, so a major number of distal synapses is potentiated. Hence, the column appears to be wider about double than control. Moreover, if multiple connections were allowed between GC and more MCs within the same glomerulus (Fig. 6.2E), the MCs could laterally inhibit each other, impairing the column formation.

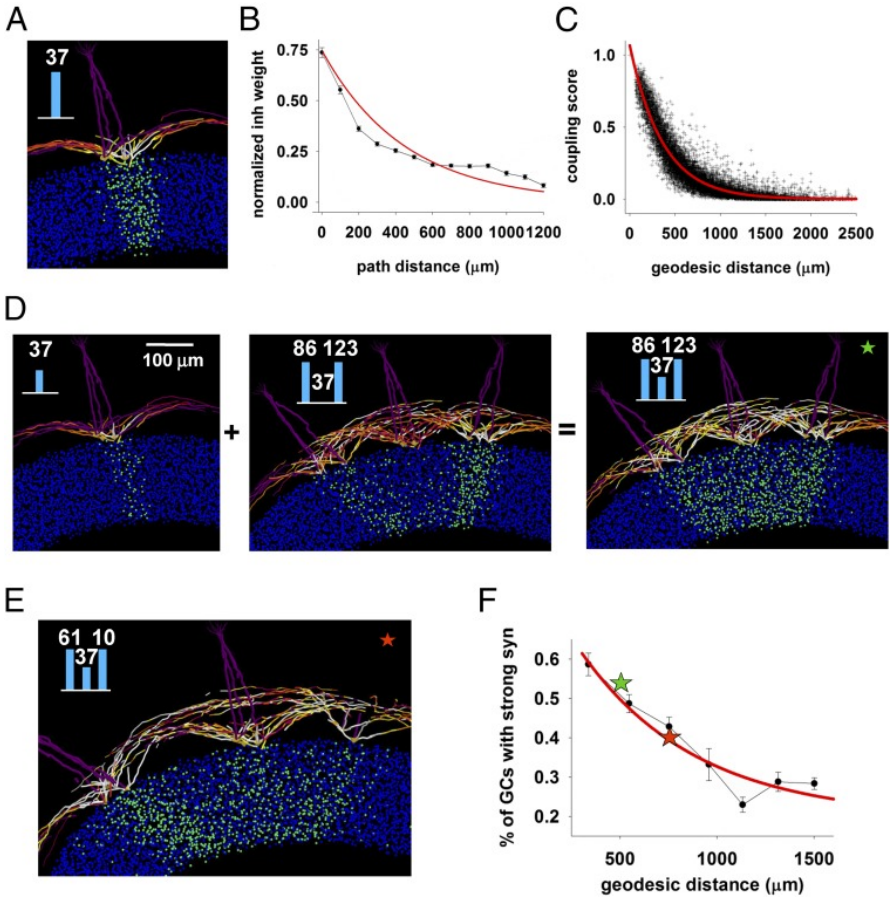

Fig. 6.3 Columns interact in a predictable distance-dependent way [39].

In summary, the column shape is not only susceptible to variation of the ratio between excitation and inhibition, but it also requires the MCs belonging to the same glomerulus connect to disjoint subsets of GCs.

6.3 Glomerular units positively or negatively interact with each other in a distance-dependent way

How do glomeruli affect activity of each other through the inhibition induced through the GC columns? To investigate this issue, we first calculated the distance-dependent inhibition that a typical column (Fig. 6.3A) below a given glomerulus can exert on another column, assuming that this is proportional to the average inhibitory weight. This is shown in (Fig. 6.3B), where we plot the average normalized inhibitory weight of GC synapses versus the distance from the column center. Assuming that all glomeruli have the same type of column associated with them, it is possible to calculate theoretically a coupling score, defined as the extent to which two columns can interact through the GCs that make synapses on MCs belonging to both columns. The score was calculated as the normalized sum of the synaptic weights of the GCs in common found within a 50 μm rectangular box centered beneath each column. The distribution of the coupling score for all of the possible pairs of our 127 experimentally labeled glomeruli is shown in Fig. 6.3C as a function of the geodesic distance between their centers and implies that GCs in common between glomeruli can receive additional input that can act in a positive or negative way for column formation. It can be expected that most of this effect will be caused by the strongest synapses.

To test this hypothesis, we ran two simulations in which glomerulus 37 was weakly stimulated alone (Fig. 6.3D, left) or together (Fig. 6.3D, middle) with two other strongly activated neighboring glomeruli (glomerulus 86 and glomerulus 123). As can be easily seen in Fig. 6.3D, right, the coupling with strongly active neighboring glomeruli promoted the formation of a better column by the weakly activated glomerulus 37. Coactivation of a more distant pair (glomeruli 61 and 10; Fig. 6.3E) resulted in a less pronounced increase of the column below glomerulus 37. We tested this mechanism for different combinations of two glomeruli at different distances from glomerulus 37, and the average (n = 9, $\pm$ SEM) proportion of GCs with strong synapses below glomerulus 37 is shown in Fig. 6.3F.

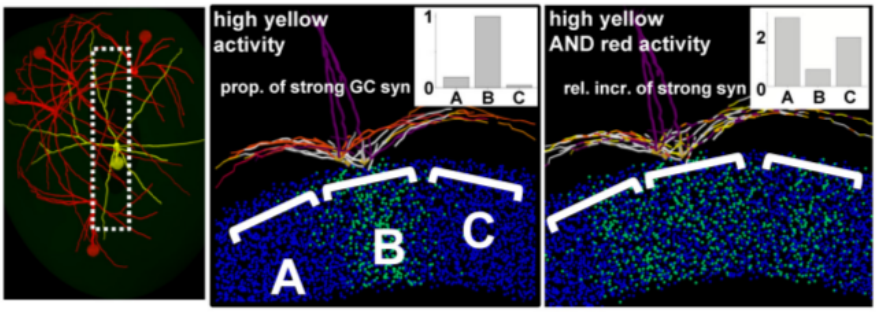

Fig. 6.4 Typical case in which the formation of a column can be hindered by activity in other glomeruli [39].

A typical case in which the formation of a column can be hindered by activity in other glomeruli is shown in Fig. 6.4. We considered how the quantity of strongly potentiated GC synapses under glomerulus 37 (yellow in left panel) was affected by the co-activation with a group of relatively distant glomeruli (red). For a first simulation, the yellow glomerulus was activated alone, and it generated a typical column (middle). The normalized proportion of potentiated synapses in three GCL regions is shown in the inset. Then, in another simulation (right), the four red glomeruli were also strongly activated. Column formation in region B, well-formed when the yellow glomerulus was activated alone, was hindered when activity in the dendrites of the MCs belonging to the red glomeruli tended to form clusters of inhibitory synapses in different parts of the dendritic range of the MCs belonging to the yellow glomerulus.

Taken together, these results suggest that the sparse, distributed, and segregated columns of active GC synapses, as those observed experimentally, can interact in a way that can promote (Fig. 6.3) or hinder (Fig. 6.4) column formation on neighboring weakly activated glomeruli.

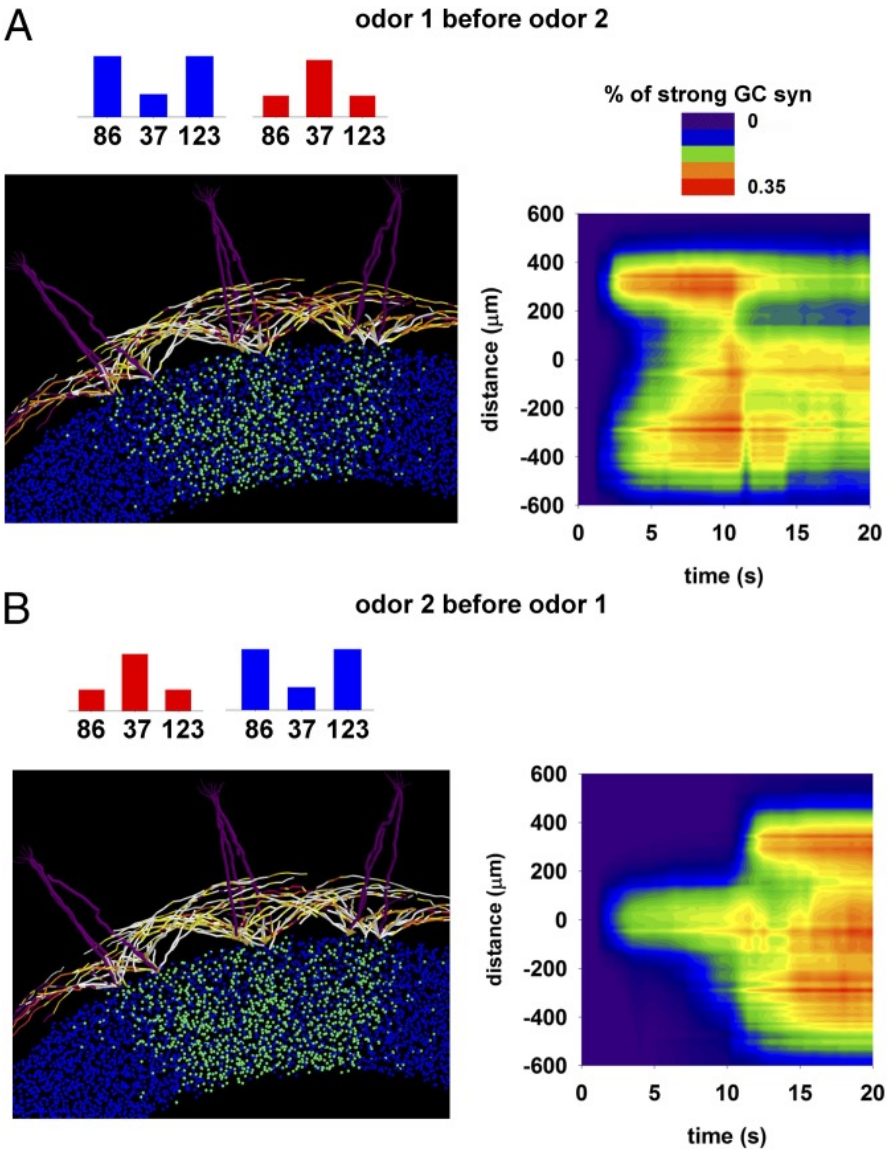

Fig. 6.5 Odor exposure is a noncommutative operation [39].

6.4 Odor exposure is a noncommutative operation

Another crucial point for understanding how OB circuits work is the network reconfiguration in the presence of different inputs. In terms of column operations, this

is equivalent to studying how new inputs may change the size and definition of any given GC column. In Fig. 6.5, we show what happens when the same two odors, activating the same neighboring glomeruli, are presented in a different sequence. This is important because although each individual may be exposed to similar odors during his or her life, the order in which odors are learned will be different. To explore this issue, we simulated the presentation of two odors in a different sequence. The final configuration of potentiated GC synapses in the two cases was significantly different (compare Fig. 6.5 A and B, left), with a different dynamic (Fig. 6.5 A and B, right). As also expected from the previous results, this effect depends on the relative distances between the glomeruli. These results suggest that the process of odor exposure is noncommutative. Each OB at any given stage of its life thus contains a unique representation not only of the past odor learning episodes but also of the order in which they were learned. This is especially true for odors that activate neighboring glomeruli.

6.5 Discussion

This study focused on two main points directly related to the network mechanisms underlying the input/output computational properties of the OB: the dynamic formation, interaction, and computational role of sparse and spatially segregated clusters of GC synapses on MCs, in relation to given glomeruli that we term GUs. The model gives new insight into the neural basis of the experimental findings on variations in a columns size, connectivity, and cell density. This in turn suggests specific theoretical and experimentally testable predictions:

1. Column formation and interaction is a dynamic process that depends in a predictable way on the concurrent activity of different GUs, their respective locations, and past odor inputs in such a way as to promote or hinder column formation on neighboring GUs. This supports and gives a physiological plausible explanation for the hypothesis and the experimental suggestions (reviewed in ref.

15) of the existence of molecular-feature-activated clusters of glomeruli. Column formation can be experimentally tested by examining changes in the activity of the same set of GCs belonging to a glomerulus before and after delivering different stimulation protocols to the glomerulus.

2. Each olfactory bulb at any given stage of its life contains a unique representation not only of the past odor learning episodes but also of the order in which they were learned. In principle, this effect can be experimentally tested by training different animals to the same or different sequences of the same odors, and then analyzing the spatial distribution of the columns formed in their olfactory bulb: individuals trained with the same odor sequence should show fewer differences among column size and distribution.

By previous 2D model of OB, it was predicted the inter-glomerular interactions through GCs are non distance-dependent [81], whereas our 3D model predicts that such interactions are distance-dependent, according to recent experimental findings [57]. The major realism of of our OB model have been crucial in reproducing the real grade of overlap among the lateral dendritic fields related to different glomeruli, which finally leads to a more correct prediction.

Recently, it was investigated the role of the dSACs, they perform a precise local inhibition on GC spine that limit the action potential propagation [31]. Under this condition, a spine is completely isolated, so it works as an independent computational unit. Therefore, dSAC action may block both positive and negative interglomerular interactions (Fig. 6.3 and 6.4) during learning. In addition, the DSACs may avoid the noncommutativity (Fig. 6.5) by selectively inhibiting the GCs that are connected at more distant dendrites from the soma, restoring the same excitation-inhibition balance of control. Taken together, the dSACs may not allow concurrent interglomerular interaction to occur. However, testing these predictions remain still not achievable by the current experimental techniques.

Moreover, dSACs may shift the GC baseline activity [114], perhaps in tandem with the excitatory axon collaterals of TCs [76]. This mechanism would mediate hypo- or hyper- response of GC that impaired the column formation with extremely

low or high excitation intensities (Fig. 6.2). Thus, dSACs may regulate the GC response during learning, eliminating those inter-glomerular interactions which impair the robustness of the column formation process.

Chapter 7

Inter-glomerular coupling through the granule cell columns and the odor coding over time

How do MCs take the input information processed in the GL and encode it for output in the second GC level? The MC activity represents the output from the GU to the OC; its firing rate is often used for this purpose [18]. However, although firing rates contain enough information to recognize an odor [54], during an odor presentation many MCs do not exhibit a significant rate change, especially in awake mice [22]. Another way in which information can be encoded is through the spike temporal distribution within a respiratory cycle [22]. One mechanism that can mediate this type of coding is the synchronization of MCs from different glomeruli [21]. Experimental findings suggest that the GC-to-MC inhibition is organized in sparse and segregated columns [58]; computational findings suggest that they may form a computational unit with their related glomerulus [39]; and in a previous study it was shown how this organization may promote synchronization between MCs belonging to different glomeruli [37].

7.1 Spine relocation in adult-born granule cells

Recently, a new form of synaptic plasticity have been recently observed in the OB, it relies on the *synaptic spine relocation of adult-born GCs* [115]. Whereas synaptic potentiation/depression protocols and the GC neurogenesis have been so far considered the only adaptation mechanisms of the OB. To different plasticity

mechanisms correspond different action time scales. For example, synaptic potentiation/depression operates in few minutes, GC neurogenesis within some days, whereas spine relocation needs just few milliseconds. Therefore, spine relocation would realize a high performance mechanism of synaptic plasticity, allowing fast adaption to rapid environmental changes.

Previous studies on the OB have suggested that the shared inhibition can devise the synchronization between the MCs [21] whereas a significant part of this inhibition is conveyed from the GCs; the reliability of GCs to drive the synchronization was also confirmed from the model of the MC-GC network [37]. Taking into consideration these suggestions, we want figure out how the mature spine migration can affect the synchronization between those MCs belonging from different glomeruli. Therefore, we have used the realistic simulations to unravel how the synchronization changes as the percentage of the migrated spines. All of these simulations have regarded three aligned glomeruli (GL86, GL37, GL123), each one with a formed column below (Fig. 7.1). The migrating spines range from 0 to 6 % of the total ones. This range is constrained to the spatial distribution of the GCs and MCs lateral dendrites, according to experimental observations. Thus, the migrating spines stem out from those GCs that are shared between the GL86 and GL123 with the GL37. For each quantity of migrated spines, we measured the synchronization between the GL37 with either the GL86 or the GL123. The synchronization has been measured as the cross-correlation between the pair of poststimulus time histograms (PSTHs) of the glomeruli that is obtained from 14 spikes trains evoked from the related sniffs (Fig. 7.1, rasters plots) using a time bin of 20 ms (Fig. 7.1, histograms).

Although a visual inspection of both the rasters plot and PSTHs does not reveal any clear difference, the cross-correlation between the glomeruli pair changes gradually as the percentage of spines migrated from the GL86 to the GL123.

Hence, these results suggest that spine migration would be a mechanisms that promotes the quick adaptation of the network to an eventual new input leading to a faster synchronization of the MCs then that obtained by an eventual formation of the new spines. These results also suggested that the relocation of relatively few

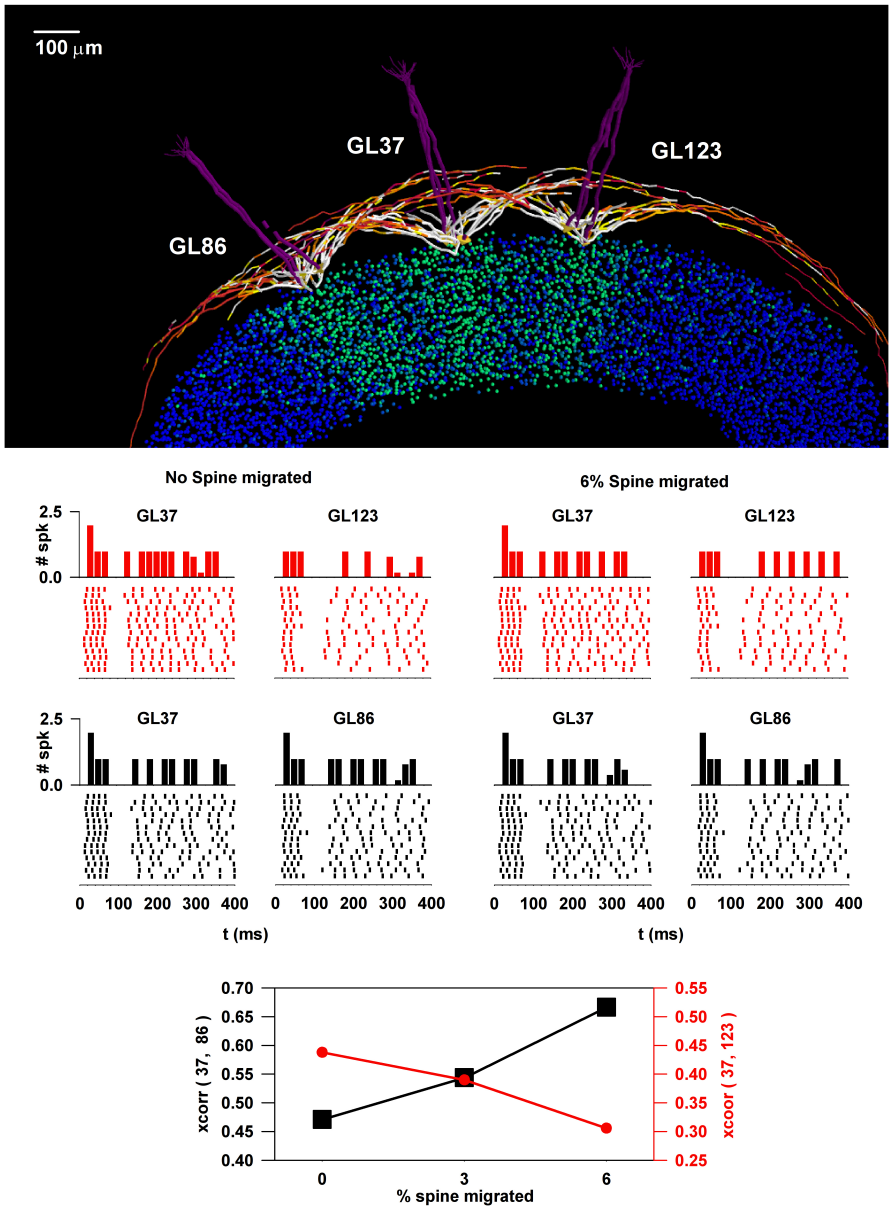

Fig. 7.1 Spine migration promotes a fast cells synchronization [115].

spines in response to a new sensory input can be an effective mechanism for quickly changing the set of synchronized MC, which in turn affects odor information processing.

7.2 The information content carried by correlated spikes

To characterize the information content carried by the synchronous MC spikes, we have analyzed the inter-glomerular synchronization during a sniff and how it is affected by the MC-GC synaptic network configuration.

For this purpose, we needed to evaluate MC spike synchronization from the spike times obtained in any given simulation, and then pool the results for the MCs belonging to a given glomerulus. Thus, we calculated the spike synchronization during a sniff, and how its information content evolved as a function of time under different conditions. Note that, the information content carried out by synchronous spikes can be finally calculated from their probability.

The total simulation time was first divided in bins of equal size, with each bin set to 1 if it contains at least one spike and 0 otherwise (Fig. 7.2A1). Two vectors were formed with two spike trains from any two given MCs connected to distinct glomeruli. A contingency table was then calculated based on the results obtained by exploring the two vectors with a sliding time window (Fig. 7.2A2).

A fundamental step is the choice for the sliding window and the bin size, which must be chosen in such a way to capture the maximum amount of information, in light of the principle of maximum entropy [26], on MC synchronization, similarly as shown in previous works. This can be pursued by considering that without GCs the activity in any two glomerular units will have a higher average joint entropy because the MC spikes are not expected to be correlated. The best combination of time window and bin size is thus that resulting in the maximum reduction of the joint entropy between spike trains obtained with or without GCs; in such manner it is discovered the combination which intercepts the maximum information carried

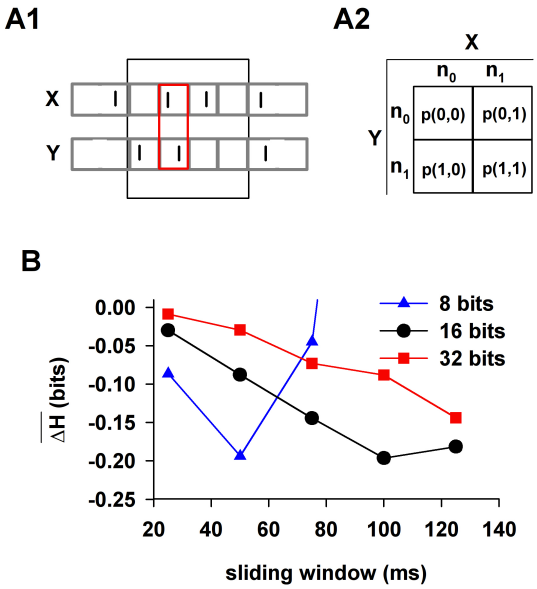

Fig. 7.2 Spikes train analysis used to calculate the information content of synchronized spikes [105].

from the MCs spikes about the stimulus. In general, the joint entropy, i.e. the entropy of a joint probability distribution (represented in our case by the contingency table) is calculated as

$$H(X_t, Y_t) = \sum_{a,b \in 0,1} -p(a,b) \log_2 p(a,b)$$

where X_t and Y_t are the discretized spikes inside a time window centered at t, and $p(a,b)$ is the probability to have a given value for a and b in the contingency table for X_t and Y_t .

The probability that any two MCs generate a spike within the same time bin can be considered as a measure of synchronization. To capture the amount of information from the simulations, we tested sliding windows of 25-125 ms partitioned in 8, 16, or 32 bins, to understand which combination results in the maximum average difference in the joint entropy between simulations with and without GCs. It was found that a 100 ms (16 bin) sliding time window gave the best result (Fig. 7.2B).

The information content during a sniff was estimated by calculating the average difference between the average information on two MCs firing during a sniff, $log_2\left(1/p^i\right)$, and its value at time t, $log_2\left(1/p_t^i\right)$, i.e.

$$\overline{\Delta I} = \frac{1}{s}\sum_{i=1}^{s}\left(log_2\left(1/p^i\right) - log_2\left(1/p_t^i\right)\right)$$

where s is the number of sniffs. Note that, the average information depends on the probability of spike synchronization, which shifts with the average firing rate during a sniff. This is in turn modulated by the combined overall amounts of excitation and inhibition conveying on tuft and lateral dendrites (by the columns), respectively. Therefore, by subtracting the average information, we take out the difference between the cases with and without columns, where the different intensity of inhibition causes then different firing rates.

The control condition was a model with two glomeruli approximately 500 μm apart, each one trained with the same stimulus, in such a way to generate a column (Fig. 7.3A). Note that, given the natural physiological variability of MC morphology, included in our model, the columns are not identical. The information content carried by correlated spikes during a sniff was estimated as eq. 7.2. The average value (from 7 sniffs) under control conditions (i.e. with GCs) is shown in the right panel of Fig.7.3B (black line); it was maximal after approximately 50 ms from the sniff onset. Without GCs (Fig. 7.3B, red line), the information content was significantly lower (Wilcoxon Signed Rank Test, p value < 0.001), suggesting that under this condition no odor information could be propagated to the cortex [21]. Note that negative values of $\overline{\Delta I}$ mean that the spikes in the MCs belonging to different glomeruli are less synchronized than average, thus carrying less information. The implication is that the GCL is able to transform the MC output signal in such a way that a relatively large amount of information is transmitted within the first 100 ms from the sniff onset. This range can be related to the overall time course of the inhibitory signal elicited by MCs during their bursting activity. Considering the additional time needed to form a behavioral response, this result is consistent with the experimental findings showing that odor recognition can occur within 200 ms

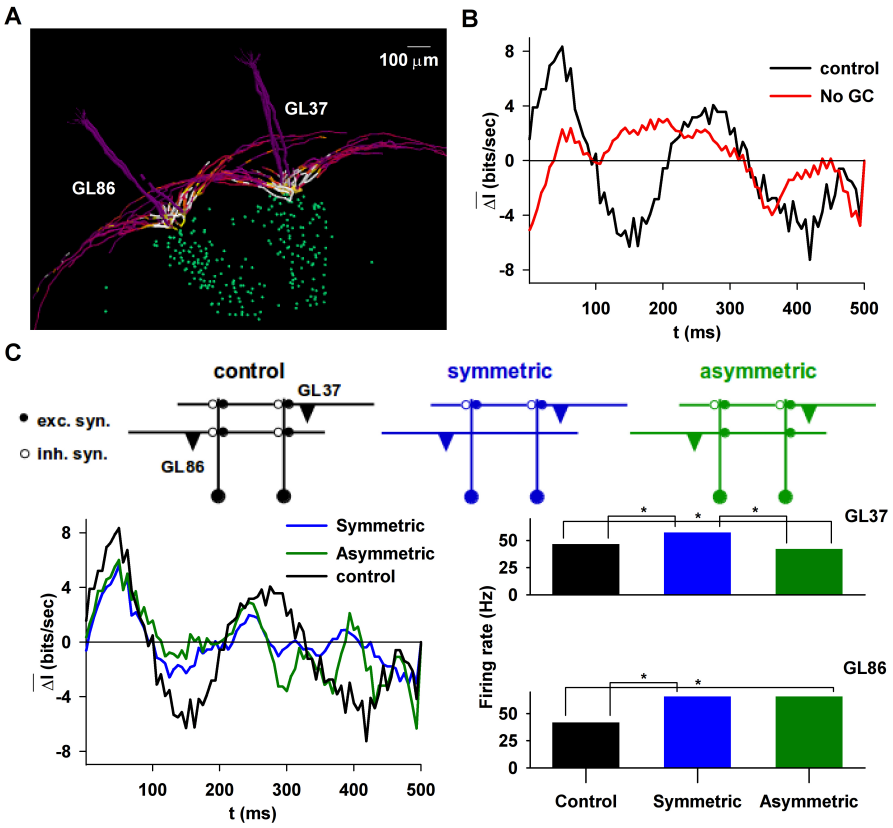

Fig. 7.3 Information content carried by correlated MC spikes during a sniff [105].

from a sniff onset [51]. This time interval must include information passing through other brain regions. The model suggests that most of the information from the OB is transmitted within the first 100ms (with a peak at about 50ms).

Odor input, in principle, can stimulate any glomerulus. This will occur independently from the presence of a column. The lack of a well-formed column in general may result in reciprocal synapses that lack one or both of the excitatory or inhibitory components. These configurations, termed symmetric or asymmetric, were predicted by our model [40] and recently observed experimentally [9]. They are schematically illustrated in the top plot of Fig. 7.3C for the two-glomeruli model used in this case. To test their effect, we calculated the difference in information content from simulations in which only one column was present, below GL37. With re-

spect to control, the information content is significantly lower when there is only one column (Fig. 7.3C, bottom left, compare black with blue/green curves), independently of the presence of symmetric ($p < 0.001$) or asymmetric ($p = 0.011$) synapses on glomerulus 86 (GL86). However, asymmetric synapses can induce lateral inhibition and can affect the spike train in a significant way. As shown in Fig.7.3C (bottom right), in the presence of asymmetric synapses (green bars) GL86 decreased significantly the GL37 firing rate, whereas the opposite (GL37-mediated inhibition on GL86) is not possible (Fig.7.3C, bottom right, compare green and blue bars for GL86). This effect may have functional consequences for odor discrimination, because it would reduce the interaction between glomeruli activated by a relatively new odor (i.e. for example with an asymmetric column) and other glomeruli previously involved with other odors (i.e. with a well-formed, and symmetric, column).

7.3 Discussion

In summary, lateral inhibition through GCL circuits is a basic mechanism for implementing interglomerular communication and shaping synchronous spike distribution across the sniff time course, maximizing the information content carried by spikes. We hypothesize that the GL circuits are not involved in this effect, because it requires a reciprocal lateral inhibitory mechanism. Such a mechanism cannot rely on the GL circuit, which implements a feedforward inhibition. The role of the GL circuit in this process cannot be studied in more detail in this work, where we implemented glomerular microcircuits with an effective set of (experimentally constrained) equations rather than with explicitly interacting cells. When more experimental constraints on morphology, electrophysiology, connectivity, and synaptic plasticity of GL circuits become available, they can be readily introduced into the model and test additional hypotheses.

Chapter 8

The odor operator theory

The previous chapter gives insight into the interactions between MCs and GCs within and between GUs during learning. These interactions continue even after the GC columns are formed, so conditioning the OB output. A mathematical characterization of them allows to estimate several important features regarding the odor representation space.

8.1 The mathematical framework based on the odor operator

We have designed a mathematical framework for analyzing the MC-GC circuit. This is assumed to work as an *operator* that transforms a given input, convergent on the GL, into an output, due to MC activities. By linear algebra, we aim to approximate the highly non-linear interactions between and within GUs to unravel the structure of the odor representation space. This approach, of course, cannot replace the realistic simulations, but would extend it by allowing an analytical and abstract interpretation of their output.

We describe the MC-GC circuit in the form of a square matrix M_{OB}, where an entry i, j describes the overall inhibition on GU_i generated by the activity of GU_j. The operator M_{OB} results of the previous odor experience, then it is related to the configuration of GC columns. Given an input vector I, and an output vector O (cor-

responding to input and output of a generic OB, respectively), the odor processing through the MC-GC circuit can be described as

$$O = I \cdot (\mathbb{1} - M_{\mathrm{OB}}) \tag{8.1}$$

Also, we assume the interaction between GUs can be represented by the combination of the three matrices W^{exc}, W^{inh}, and H:

$$M_{\mathrm{OB}} = W^{\mathrm{inh}} \cdot H \cdot W^{\mathrm{exc}} \tag{8.2}$$

where

- W^{exc} is NxN_{GC} matrix
- W^{inh} is $N_{\mathrm{GC}}xN$ matrix
- H is $N_{\mathrm{GC}}xN_{\mathrm{GC}}$ matrix

N_{GC} and N are the number of GC columns and GUs, respectively. Particularly, each entry in W^{exc}, w_{ij}^{exc}, describes the overall synaptic weight (or excitation) converging from GU_i to j-GC column; conversely, each entry in W^{inh}, w_{ij}^{inh}, is graded with the overall synaptic weight (or inhibition) converging from j-GC column to GU_i. The H matrix is a connectivity matrix describing how the presence of different GC columns is correlated within a given OB. This way suggests a general strategy to study the OB, which can be applied on any specific OB, independently on its size and connectivity.

8.2 Classes of odor operators

To illustrate the usefulness of this approach, we consider one of the simulation findings: the presentation sequence of the learned odors affects the final network configuration (Fig. 8.1). This means that the OB in each individual is different, implying that each individual presumably transforms the same input into different outputs.

How can this be related with the fact that most individuals are able to recognize the same odor independent from their personal history of odor exposure?

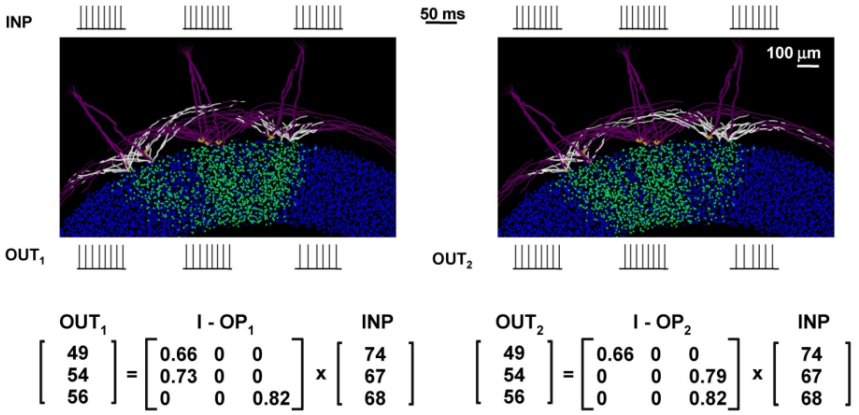

Fig. 8.1 Naive example of different odor operators that return same outputs with same inputs[39].

This question can be turned to how many different classes $\mathscr{C}_{\mathrm{OB}}$ of operators M_{OB} result in the same output with a given input? We have estimated the number of different operator classes by analyzing the structure of M_{OB}. We call $\mathscr{C}^m_{\mathrm{OB}}$ the odor operator class with m non-zero elements on each row of the matrices; k_0 are rows with only zeros, k_1 are rows with only a single non-zero entry, k_2 are rows with two non-zero entries, and so on; N is the number of GUs so that $N = \sum_{j=0}^{m} k_j$. Formally, the problem can be seen as the computation of $|\mathscr{C}_{\mathrm{OB}}|$ under the following condition

$$\exists I, O : \exists M_{\mathrm{OB},i}, M_{\mathrm{OB},j} \in \mathscr{C}_{\mathrm{OB}}, M_{\mathrm{OB},i} \neq M_{\mathrm{OB},j} \Rightarrow M_{\mathrm{OB},i} \cdot I = M_{\mathrm{OB},j} \cdot I$$

For $m = 1$ we have

$$|\mathscr{C}^1_{\mathrm{OB}}| = \sum_{k_0,k_1=0}^{N} \binom{N}{k_0} N^{k_1} \tag{8.3}$$

This is equivalent to the physiological condition in which each GU is able to inhibit only one other GU among the $k_1 = N - k_0$ others. Assuming the inhibition of the k_1 GUs involves only a proportions p of them, we can approximate to

$$|\mathscr{C}^1_{\mathrm{OB}}| = \sum_{k_0,k_1=0}^{N} \binom{N}{k_0} \lfloor p \cdot N \rfloor^{k_1} \tag{8.4}$$

For $m = 2$ we have

$$|\mathscr{C}^2_{\mathrm{OB}}| = \sum_{k_0,k_1,k_2=0}^{N} \binom{N}{k_0} \binom{N-k_0}{k_1} N^{k_1} \binom{N}{2}^{k_2} \tag{8.5}$$

This is equivalent to the physiological condition in which each GU is able to inhibit only one other GU among the $k_1 = N - k_0$ others. Assuming the inhibition of the k_1 GUs involves only a proportions p of them, we can approximate to

$$|\mathscr{C}^2_{\mathrm{OB}}| = \sum_{k_0,k_1,k_2=0}^{N} \binom{N}{k_0} \binom{N-k_0}{k_1} \lfloor p \cdot N \rfloor^{k_1} \binom{\lfloor p \cdot N \rfloor}{2}^{k_2} \tag{8.6}$$

In general, $\forall m \leq N$, the number of classes is

$$\Omega^m_N \left[N^{k_1} \binom{N}{2}^{k_2} \binom{N}{3}^{k_3} \ldots \binom{N}{m-1}^{k_{m-1}} \binom{N}{m}^{k_m} \right] = \Omega^m_N \prod_{i=1}^{m} \binom{N}{i}^{k_i} \tag{8.7}$$

where

$$\binom{N}{k_0} \binom{N-k_0}{k_1} \binom{N-k_0-k_1}{k_2} \ldots \binom{N-\sum_{i=0}^{m-2} k_i}{k_{m-1}} \tag{8.8}$$

then

$$|\mathscr{C}^m_{\mathrm{OB}}| = \sum_{k_0,k_1,k_2,\ldots,k_m=0}^{c} \Omega^m_N \prod_{i=1}^{m} \binom{N}{i}^{k_i} \tag{8.9}$$

If $m = N$, we obtain

$$|\mathscr{C}^N_{\mathrm{OB}}| = 2^{N^2} \tag{8.10}$$

whereas if only a proportion p of total GUs are involved

$$|\mathscr{C}^{\lfloor p \cdot N \rfloor}_{\mathrm{OB}}| = 2^{\lfloor p \cdot N \rfloor^2} \tag{8.11}$$

Finally, if $m \leq \lfloor p \cdot N \rfloor$ and $N = \sum_{j=0}^{m} k_j \leq \lfloor p \cdot N \rfloor$

$$|\mathscr{C}^{\lfloor p \cdot N \rfloor}_{\mathrm{OB}} = \sum_{\substack{k_1,\ldots,k_m=1 \\ k_1+\ldots+k_m \leq \lfloor p \cdot N \rfloor \\ k_0 = N-(k_1+\ldots+k_m)}}^{\lfloor p \cdot N \rfloor} \left[\Omega^m_N \prod_{i=1}^{m} \binom{\lfloor p \cdot N \rfloor}{i}^{k_i} \right] \tag{8.12}$$

with $m = \lfloor p \cdot N \rfloor$

$$|\mathscr{C}_{\mathrm{OB}}^{\lfloor p\cdot N\rfloor}| = 2^{\lfloor p\cdot N\rfloor^2} \tag{8.13}$$

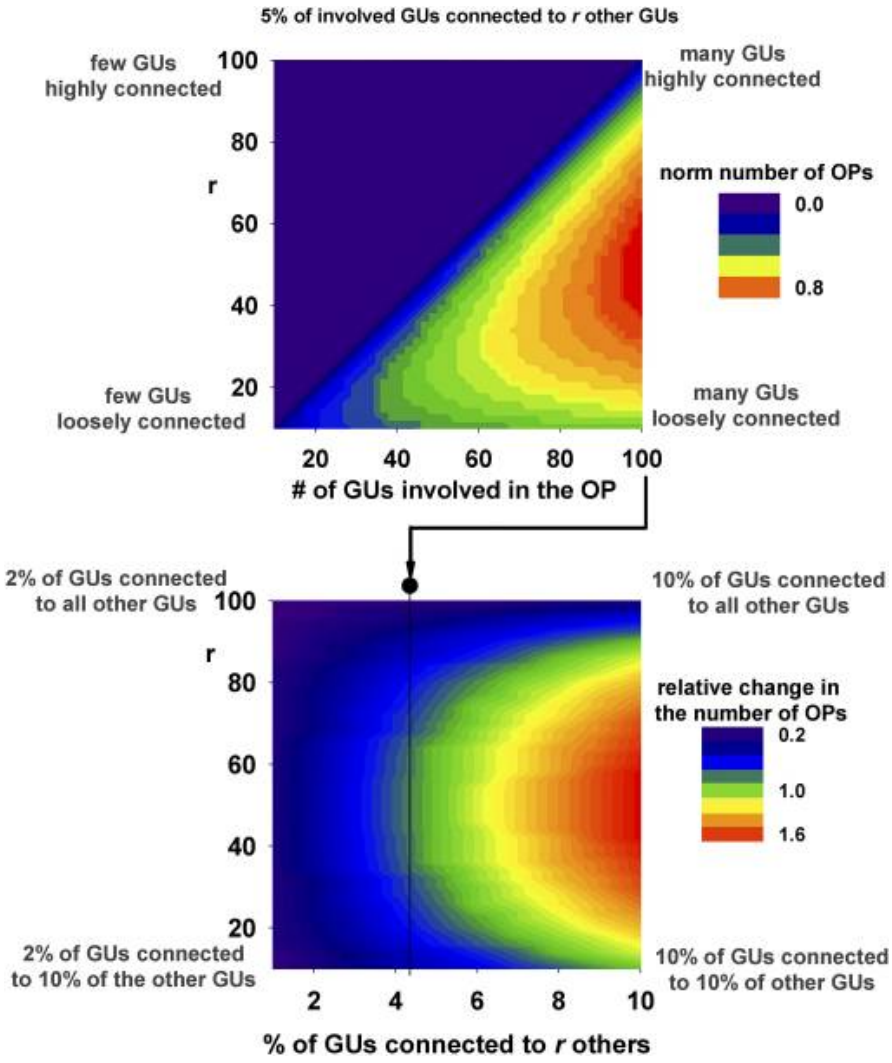

Fig. 8.2 There is a discrete number of operators that operate on a given input to give the same output, in terms of firing rate [39].

Of course, the number of operators changes as a function of the parameters that are the number of involved GUs and the degree of connectivity between them. Fig. 8.2 shows how these paremeters affect the (normalized) number of operators, as-

suming an OB formed by 1,000 GUs. As can be expected, the number of operators increases with the number of involved GUs, whereas it can increase or decrease with their connectivity (Fig. 8.2, top). However, there is a specific combination of size and connectivity for which the number of operators is higher. This optimal number can further increase or decrease with the number of GUs connected to others (Fig. 8.2, bottom). It should be stressed that the actual number of operators will depend on the values of the parameters, such as the number of GUs (which affects the size of the operator) and the connectivity properties (which affect the way in which non-zero elements are distributed in the operator).

8.3 Discussion

A theory based on experiments is necessary to gain insight into a complex system such as the MC-GC network. The mathematical framework introduced in this chapter illustrates how the transformation of an input into a specific output can be described by a square matrix defining an operator corresponding to a specific configuration of OB at any given instant of its life. Operators are commonly used to describe input/output transformation of neuronal signals. Typical examples are those used to model the receptive field of retinal ganglion cells [124], representation of time [125], auditory stimuli [126], and extracellular neural signals [127]. In our case, this seems to be a promising approach that allows one to make general predictions about the properties, number, and structure of the operators representing the odor stimuli. This appears to be the first time to our knowledge that the operations of the OB are represented in this way. General computational models of the OB operations are usually implemented using a pattern recognition approach with artificial or single-point neuron networks, built from scratch according to the kind of problems/hypotheses to investigate. Here, we were instead interested in obtaining an abstract representation of the OB that nevertheless retained a direct link with its physiological components, structure, and properties at the single-cell level.

The odor operator concept thus provides a framework for understanding how the glomerular-based connectivity of the olfactory bulb can mediate non-commutative learning experiences in different individuals that nonetheless can give rise to similar odor perceptions. The degree of similarity can be seen to be a complex but analytical function of both the number of involved GUs and how they are connected. Further development of this approach should lead toward insight into the optimal balance between numbers and sizes of GUs and the uniqueness of individual odor learning experiences.

Chapter 9

A new model of the olfactory receptor neuron response

The ORNs realize the earliest odor representation of the olfactory system, of which they constitute the outermost layer. Each ORN has a simple structure, and even the dynamic underlying its response may be relatively ordinary.

However, no model can predict its response to odor faithfully. Particularly, the existing models are not able to predict *synergistic* or *inhibitory* responses evoked by a binary odor mixture. Some of these models have been built without motivating their equations by a kinetic. Here, we try to fix this shortcoming by defining a new kinetic, verifying its ability in fitting the experimental data.

9.1 The previous kinetic

The ORNs constitute the outermost layer of the olfactory system, so they directly interact with the external environment. They are tiny and morphologically homogeneous neurons that translate the identity and concentration of odor molecules into neural activity. Therefore, they perform the first odor representation of the olfactory system. If the reader wants to know more details about the ORNs, we remaind to section 1.3.1.

An odor receptor is located on top of the ORN. It binds with odor molecules, triggering a complex cascades of reactions that activate G-proteins. The ORNs are in different subtypes, each corresponding to a different odor receptor. Every type

of odor receptor is in turn sensitive to subgroups of odor molecules. This therefore leads to different dose-dependent responses to different odors [128, 129, 130]. The response is a (sigmoidal) Hill function of the odor concentration.

Previously, in order to model the ORN response, the following kinetic was defined for single odor [129]:

$$\mathrm{R} + \mathrm{U} \quad \underset{k_{-1U}}{\overset{k_{1U}}{\rightleftharpoons}} \quad \mathrm{C}_U \quad \underset{k_{-2U}}{\overset{k_{2U}}{\rightleftharpoons}} \quad \mathrm{P}$$

with the conservative law

$$R_0 = R + C_U + P$$

where R is the free receptor, U is the odor, C_U is the complex formed after binding, P is the product, and R_0 is the overall of receptor.

By applying the *Law Mass Model*, and after a several substitutions, one finally obtains the equation of the ORN response as function of the odor concentration:

$$P = \frac{F_U}{1 + \frac{K_U}{U}}$$

The product P is related to the activated G-protein. It is graded with the maximum opening of the receptor-coupled channel. The opening fraction of the channel in turn grades the ORN response. The product P therefore predicts the ORN neural activity in response to an odor at a certain concentration.

In presence of binary mixture (with two odors U and V), the previous kinetic is extended to

$$\mathrm{R} + \mathrm{U} \quad \underset{k_{-1U}}{\overset{k_{1U}}{\rightleftharpoons}} \quad \mathrm{C}_U \quad \underset{k_{-2U}}{\overset{k_{2U}}{\rightleftharpoons}} \quad \mathrm{P}_U$$

$$\mathrm{R} + \mathrm{V} \quad \underset{k_{-1V}}{\overset{k_{1V}}{\rightleftharpoons}} \quad \mathrm{C}_V \quad \underset{k_{-2V}}{\overset{k_{2V}}{\rightleftharpoons}} \quad \mathrm{P}_V$$

with the conservative law

$$R_0 = R + C_U + P_U + P_V$$

Thus, the overall product P for a binary mixture of U and V is

$$P = P_U + P_V = \frac{F_U \left(\frac{U}{K_U}\right)^n + F_V \left(\frac{V}{K_V}\right)^n}{1 + \left(\frac{U}{K_U}\right)^n + \left(\frac{V}{K_V}\right)^n} \tag{9.1}$$

Cruz and Lowe [130] demonstrated how this kinetic holds an ambiguity if one considers a mixture formed by two identical odors, so that $U = V$. Under this condition, the total concentration is $2U$, so the eq. 9.1 is turned to

$$P = P_U + P_U = \frac{F_U \left(\frac{U}{K_U}\right)^n + F_U \left(\frac{U}{K_U}\right)^n}{1 + \left(\frac{U}{K_U}\right)^n + \left(\frac{U}{K_U}\right)^n} = \frac{2F_U \left(\frac{U}{K_U}\right)^n}{1 + 2\left(\frac{U}{K_U}\right)^n}$$

This differs from the response for single odor at double concentration which is

$$2P_U = \frac{2F_U \left(\frac{U}{K_U}\right)^n}{1 + 2\left(\frac{U}{K_U}\right)^n} \neq \frac{F_U \left(\frac{2U}{K_U}\right)^n}{1 + \left(\frac{2U}{K_U}\right)^n} = P_{2U}$$

In order to fix this problem, by several reductions, Cruz and Lowe [130] rewrote the eq. 9.1 as

$$\frac{F_M}{1 + \left[\frac{1 + \frac{U}{K_U} + \frac{V}{K_V}}{\eta_U \frac{U}{K_U} + \eta_V \frac{V}{K_V}}\right]^n} \tag{9.2}$$

while the dose-response curve for single odor is

$$P_U = \frac{F_M}{1 + \frac{1}{\eta_U^n}\left(1 + \frac{K_U}{U}\right)^n}$$

Note that Cruz and Lowe [130] only performed a cascade of algebric manipulations without modifying the original kinetic.

Marasco et al. [36] again extended the eq. 9.2 by constraining the exponent related to a mixture

$$n_{UV} = \frac{n_U \eta_U K_V + n_V \rho \eta_V K_U}{\eta_U K_U + \rho \eta_V K_V}$$

Thus, they eliminated any correspondence between the dose-response equation and the kinetic. They also found the equations of the parameters η_{UV} and K_{UV}:

$$\begin{cases} \eta_{UV} = \frac{\eta_U K_V + \rho \eta_V K_U}{K_U + \rho K_V} \\ K_{UV} = \frac{K_U K_V (1+\rho)}{\rho K_U + K_V} \end{cases}$$

So far, the kinetic are somewhat unreasonable. It indeed assumed the reversibility of the product P, which can turn back to the complex. This would imply that the ligands of odor molecules do not change after binding, which is not realistic.

Taking into account these shortcomings and the results obtained by the previous models, we have built a new kinetic.

9.2 A new kinetic scheme

Biochemical reactions can be modeled through the kinetic of Michaelis and Menten [131]. Here, we find a new kinetic to model the ORN response. We start by defining our kinetic for single odor. It consists of the following reactions:

$$\mathrm{R} + \mathrm{U} \underset{k_{-1U}}{\overset{k_{1U}}{\rightleftharpoons}} \mathrm{R}^*_U \xrightarrow{k_{2U}} \mathrm{D}_U \xrightarrow{k_{3U}} \mathrm{R}$$

$$\mathrm{R}^*_U + \mathrm{U} \underset{k_{-4U}}{\overset{k_{4U}}{\rightleftharpoons}} \mathrm{R}^*_U\,\mathrm{U} \xrightarrow{k_{5U}} \mathrm{D}^*_U + \mathrm{P} \xrightarrow{k_{6U}} \mathrm{R}^*_U + \mathrm{P}$$

$$\mathrm{P} \xrightarrow{\mathrm{k}_P}$$

As usual, we assume that the total receptor is conserved across reactions

$$[R]^0 = [R] + [R^*_U] + [D_U] + [R^*_U U] + [D^*_U] \tag{9.3}$$

The first reaction describes the odor receptor priming. This is the main novelty of our model. Odor molecules with concentration U bind with free receptor R, producing primed odor receptor R^*_U but without making any product P. Therefore, no ORN response is evoked by priming. The receptor priming is typically occuring in metabotropic receptors, wherein the neurotransmitters pre-activate the receptors without triggering any membrane voltage change. The response is subsequently evoked when more neurotransmitters bind with primed odor receptors.

The primed receptor R^*_U can either turn to desensitived receptor D_U, or binding with odor molecules, so causing the second reaction. The desensitived receptor D_U turns back to free receptor R. Instead, in the second reaction, likewise the first re-

action, the primed receptor R_U^* binds with odor molecules U forming the complex R_U^*U. This reaction makes the product P and desensitived receptor D_U^*. Even in our kinetic, the product P grades the ORN response. P is a generic state that may be related to the active G-protein. In accord with calcium-signal imaging of ORN response [12], the concentration of the G-proteins decay with time, as well as the ORN response, which is modeled by the third reaction.

The first and the second reactions constitute a cooperative Michalis-Menten kinetic. It implies that the odor molecules use to bind with several distinct sites of the same receptor (allostery). This kind of kinetic is tipical for synergistic/inhibitory phoenomena. Additionally, in presence of different types of odor molecules, this kinetic is extended by adding competive receptor binding, as explained in the next section.

Next, by applying the *Law Mass Model*, these reactions are translated into a non-linear equation set.

$$\begin{cases} \dot{u} = -k_{1U}ur + k_{-1U}c_1 - k_{4U}uc_1 + k_{-4U}c_2 \\ \dot{r} = -k_{1U}ur + k_{-1U}c_1 - k_{3U}d_1 \\ \dot{c_1} = k_{1U}ur - (k_{-1U} + k_{2U})c_1 - k_{4U}uc_1 + (k_{-4U} + k_{6U})c_2 \\ \dot{d_1} = k_{2U}c_1 - k_{3U}d_1 \\ \dot{c_2} = k_{4U}uc_1 - (k_{-4U} + k_{5U})c_2 \\ \dot{d_2} = k_{5U}c_2 - k_{6U}d_1 \\ \dot{p} = k_{5U}c_2 - k_P p \end{cases} \tag{9.4}$$

with the conservation law (eq. 9.3)

$$\dot{r} + \dot{c_1} + \dot{d_1} + \dot{c_2} + \dot{d_2} = 0 \implies r(t) + c_1(t) + d_1(t) + c_2(t) + d_2(t) = r_0 \tag{9.5}$$

and initial conditions

$$r(0) = r_0, u(0) = u_0, c_1(0) = 0, d_1(0) = 0, c_2(0) = 0, d_2(0) = 0$$

while concentration of the reactants are

$$u=[U], r=[R], c_1=[R^*_U], d_1=[D_U], c_2=[R^*_U U], d_2=[D^*_U], p=[P], p_0=[R]^0$$

Since the odor concentration within a nostril is high compared to the number of receptors, we think that is reasonable to assume the *quasi steady state approximation*. Under this condition, one assumes that the complex formation is fast, so that $\dot{c} \approx 0$. It can be seen as the odor concentration does not significantly change during the initial transient stage, achieving the steady-state very quickly. Its equation can be therefore neglected when we find the solution at equilibrium of the eqs 9.4:

$$\begin{cases} \dot{r} = -k_{1U} ur + k_{-1U} c_1 - k_{3U} d_1 = 0 \\ \dot{c_1} = k_{1U} ur - (k_{-1U} + k_{2U}) c_1 - k_{4U} u c_1 + (k_{-4U} + k_{6U}) c_2 = 0 \\ \dot{d_1} = k_{2U} c_1 - k_{3U} d_1 = 0 \\ \dot{c_2} = k_{4U} u c_1 - (k_{-4U} + k_{5U}) c_2 = 0 \\ \dot{d_2} = k_{5U} c_2 - k_{6U} d_1 = 0 \\ \dot{p} = k_{5U} c_2 - k_P p = 0 \end{cases}$$

For sake of readibility, we prefer to avoid rewriting this equation set as many time as it was manipulated. We rather prefer to briefly describe how it was manipulated: first, we find d_1, d_2, and c_2 that are replaced in the system; second, $\dot{c_1}$ is coincident with $\dot{r}$ which can be therefore ignored; finally, we replace c_1 and c_2. We thus obtain

$$\begin{cases} c_1 = \frac{k_{1U}}{k_{-1U}+k_{2U}} ur \\ d_1 = \frac{k_{2U}}{k_{3U}} \frac{k_{1U}}{k_{-1U}+k_{2U}} ur \\ c_2 = \frac{k_{4U}}{k_{-4U}+k_{5U}} \frac{k_{1U}}{k_{-1U}+k_{2U}} u^2 r \\ d_1 = \frac{k_{5U}}{k_{6U}} \frac{k_{4U}}{k_{-4U}+k_{5U}} \frac{k_{1U}}{k_{-1U}+k_{2U}} u^2 r \\ p = \frac{k_{5U}}{k_P} \frac{k_{4U}}{k_{-4U}+k_{5U}} \frac{k_{1U}}{k_{-1U}+k_{2U}} u^2 r \end{cases}$$

where $K_U = \frac{k_{-1U}+k_{2U}}{k_{1U}}$, $K^*_U = \frac{k_{-4U}+k_{5U}}{k_{4U}}$, $\frac{F_U}{r_0} = \frac{k_{5U}}{k_P}$, $M_U = \frac{k_{2U}}{k_{3U}}$, $M^*_U = \frac{k_{2U}}{k_{3U}}$

$$\begin{cases} c_1 = \frac{ur}{K_U} \\ d_1 = M_U \frac{ur}{K_U} \\ c_2 = \frac{u^2 r}{K_U^* K_U} \\ d_1 = M_U^* \frac{u^2 r}{K_U^* K_U} \\ p = \frac{F_U}{r_0} \frac{u^2 r}{K_U^* K_U} \end{cases} \tag{9.6}$$

The eq. 9.6 is the solution at equilibrium. By replacing all terms of the eq. 9.6 into the eq. 9.5, we obtain

$$r_0 = r + \frac{ur}{K_U} + M_U \frac{ur}{K_U} + \frac{u^2 r}{K_U^* K_U} + M_U^* \frac{u^2 r}{K_U^* K_U} = r\left(1 + \frac{u}{K_U} + M_U \frac{u}{K_U} + \frac{u^2}{K_U^* K_U} + M_U^* \frac{u^2}{K_U^* K_U}\right)$$

In order to find r, the previous equation can be rewritten as

$$r = \frac{r_0}{1 + \frac{u}{K_U} + M_U \frac{u}{K_U} + \frac{u^2}{K_U^* K_U} + M_U^* \frac{u^2}{K_U^* K_U}}$$

By replacing the product p of eqs. 9.6, we obtain

$$p = \frac{F_U}{r_0} \frac{u^2 r}{K_U^* K_U} = \frac{F_U}{r_0} \frac{u^2}{K_U^* K_U} \frac{r_0}{1 + \frac{u}{K_U} + M_U \frac{u}{K_U} + \frac{u^2}{K_U^* K_U} + M_U^* \frac{u^2}{K_U^* K_U}} = \frac{F_U}{\frac{K_U^* K_U}{u^2} + \frac{K_U^*}{u} + M_U \frac{K_U^*}{u} + 1 + M_U^*} = \frac{F_U}{\frac{K_U^* K_U}{u^2} + \frac{K_U^*}{u}(1 + M_U) + 1 + M_U^*}$$

Although this is not a Hill function, it is still a sigmoidal function.

9.2.1 The extended version of our kinetic for binary mixture

Here, we describe our model extended for binary mixtures.

$$\mathrm{R} + \mathrm{U} \underset{k_{-1U}}{\overset{k_{1U}}{\rightleftharpoons}} \mathrm{R}_U^* \xrightarrow{k_{2U}} \mathrm{D}_U \xrightarrow{k_{3U}} \mathrm{R}$$

$$\mathrm{R} + \mathrm{V} \underset{k_{-1V}}{\overset{k_{1V}}{\rightleftharpoons}} \mathrm{R}^*_V \xrightarrow{k_{2V}} \mathrm{D}_V \xrightarrow{k_{3V}} \mathrm{R}$$

$$\mathrm{R}^*_U + \mathrm{U} \underset{k_{-4U}}{\overset{k_{4U}}{\rightleftharpoons}} \mathrm{R}^*_U\,\mathrm{U} \xrightarrow{k_{5U}} \mathrm{D}^*_{UU} + \mathrm{P} \xrightarrow{k_{6U}} \mathrm{R}^*_U + \mathrm{P}$$

$$\mathrm{R}^*_V + \mathrm{V} \underset{k_{-4V}}{\overset{k_{4V}}{\rightleftharpoons}} \mathrm{R}^*_V\,\mathrm{V} \xrightarrow{k_{5V}} \mathrm{D}^*_{VV} + \mathrm{P} \xrightarrow{k_{6V}} \mathrm{R}^*_V + \mathrm{P}$$

$$\mathrm{R}^*_V + \mathrm{U} \underset{k_{-4U}}{\overset{k_{4U}}{\rightleftharpoons}} \mathrm{R}^*_V\,\mathrm{U} \xrightarrow{k_{5U}} \mathrm{D}^*_{VU} + \mathrm{P} \xrightarrow{k_{6U}} \mathrm{R}^*_V + \mathrm{P}$$

$$\mathrm{R}^*_U + \mathrm{V} \underset{k_{-4V}}{\overset{k_{4V}}{\rightleftharpoons}} \mathrm{R}^*_U\,\mathrm{V} \xrightarrow{k_{5V}} \mathrm{D}^*_{UV} + \mathrm{P} \xrightarrow{k_{6V}} \mathrm{R}^*_U + \mathrm{P}$$

$$\mathrm{P} \xrightarrow{\mathrm{k}_P}$$

with the conservation law

$$\begin{aligned}[R]^0 = [R] + [R^*_U] + [D_U] + [R^*_U U] + [D^*_{UU}] + \\ [R^*_V] + [D_V] + [R^*_V V] + [D^*_{VV}] + \\ [R^*_U V] + [D_{UV}] + [R^*_V U] + [D_{VU}]\end{aligned} \tag{9.7}$$

The concentration of reactants are

$$u = [U], r = [R], p = [P], p_0 = [R]^0,$$

$$c_1 = [R^*_U], c_2 = [R^*_V], c_3 = [R^*_U U], c_4 = [R^*_V V], c_5 = [R^*_U V], c_6 = [R^*_V U],$$

$$d_1 = [D_U], d_2 = [D_V], d_3 = [D^*_{UU}], d_4 = [D^*_{VV}], d_5 = [D^*_{UV}], d_6 = [D^*_{VU}]$$

Even for binary mixtures, we apply the *Law Mass Model*, and assume the *quasi steady state approximation*, as well as for single odor. By performing the same substitutions, we obtain

$$\begin{cases} c_1 = \frac{ur}{K_U} \\ c_2 = \frac{vr}{K_V} \\ c_3 = \frac{u^2 r}{K_U^* K_U} \\ c_4 = \frac{v^2 r}{K_V^* K_V} \\ c_5 = \frac{uvr}{K_U^* K_V} \\ c_6 = \frac{uvr}{K_V^* K_U} \\ d_1 = M_U \frac{ur}{K_U} \\ d_2 = M_V \frac{vr}{K_V} \\ d_3 = M_U^* \frac{u^2 r}{K_U^* K_U} \\ d_4 = M_V^* \frac{v^2 r}{K_V^* K_V} \\ d_5 = M_U^* \frac{uvr}{K_U^* K_V} \\ d_6 = M_V^* \frac{uvr}{K_V^* K_U} \\ p = \frac{F_U}{r_0} \frac{u^2 r}{K_U^* K_U} + \frac{F_V}{r_0} \frac{v^2 r}{K_V^* K_V} + \frac{F_U}{r_0} \frac{uvr}{K_U^* K_V} + \frac{F_V}{r_0} \frac{uvr}{K_V^* K_U} \end{cases} \tag{9.8}$$

so the conservation law can be rewritten as

$$r_0 = r + c_1 + c_2 + c_3 + c_4 + c_5 + c_6 + d_1 + d_2 + d_3 + d_4 + d_5 + d_6 =$$

$$r + \frac{ur}{K_U} + \frac{vr}{K_V} + M_U \frac{ur}{K_U} + M_V \frac{vr}{K_V} + \frac{u^2 r}{K_U^* K_U} + \frac{v^2 r}{K_V^* K_V} + \frac{uvr}{K_U^* K_V} + \frac{uvr}{K_V^* K_U} +$$

$$M_U^* \frac{u^2 r}{K_U^* K_U} + M_V^* \frac{v^2 r}{K_V^* K_V} + M_U^* \frac{uvr}{K_U^* K_V} + M_V^* \frac{uvr}{K_V^* K_U} =$$

$$r + \frac{ur}{K_U} + \frac{vr}{K_V} + M_U \frac{ur}{K_U} + M_V \frac{vr}{K_V} + \left(\frac{u}{K_U^*} + \frac{v}{K_V^*} \right) \left(\frac{ur}{K_U} + \frac{vr}{K_V} \right) +$$

$$\left(M_U^* \frac{u}{K_U^*} + M_V^* \frac{v}{K_V^*} \right) \left(\frac{ur}{K_U} + \frac{vr}{K_V} \right) =$$

$$r \left[1 + \frac{u}{K_U} + \frac{v}{K_V} + M_U \frac{u}{K_U} + M_V \frac{v}{K_V} + \left(\frac{u}{K_U^*} + \frac{v}{K_V^*} + M_U^* \frac{u}{K_U^*} + M_V^* \frac{v}{K_V^*} \right) \left(\frac{u}{K_U} + \frac{v}{K_V} \right) \right]$$

The following equation is hence turned to find the equation for receptor r

$$r = \frac{r_0}{1 + \frac{u}{K_U} + \frac{v}{K_V} + M_U \frac{u}{K_U} + M_V \frac{v}{K_V} + \left(\frac{u}{K_U^*} + \frac{v}{K_V^*} + M_U^* \frac{u}{K_U^*} + M_V^* \frac{v}{K_V^*}\right)\left(\frac{u}{K_U} + \frac{v}{K_V}\right)} \tag{9.9}$$

We simplify the equation of the product p (see eq. 9.8)

$$p = \left(\frac{F_U}{r_0}\frac{u^2}{K_U^* K_U} + \frac{F_V}{r_0}\frac{uv}{K_V^* K_U} + \frac{F_U}{r_0}\frac{uv}{K_U^* K_V} + \frac{F_V}{r_0}\frac{v^2}{K_V^* K_V}\right) r = \left(\frac{F_U}{r_0}\frac{u}{K_U^*} + \frac{F_V}{r_0}\frac{v}{K_V^*}\right)\left(\frac{u}{K_U} + \frac{v}{K_V}\right) r \tag{9.10}$$

Next, we replace the eq. 9.9 into the eq. 9.10, so obtaining

$$p = \frac{\left(\frac{F_U}{r_0}\frac{u}{K_U^*} + \frac{F_V}{r_0}\frac{v}{K_V^*}\right)\left(\frac{u}{K_U} + \frac{v}{K_V}\right) r_0}{1 + \frac{u}{K_U} + \frac{v}{K_V} + M_U \frac{u}{K_U} + M_V \frac{v}{K_V} + \left(\frac{u}{K_U^*} + \frac{v}{K_V^*} + M_U^* \frac{u}{K_U^*} + M_V^* \frac{v}{K_V^*}\right)\left(\frac{u}{K_U} + \frac{v}{K_V}\right)} \tag{9.11}$$

By assuming that $v = \rho u$ and $x = u + v$, we obtain u and v as function of x

$$\begin{cases} u = \frac{x}{1+\rho} \\ v = \frac{\rho x}{1+\rho} \end{cases} \tag{9.12}$$

We replace the eq. 9.12 into the eq. 9.11

$$p = \frac{\left(F_U \frac{1}{K_U^*} + F_V \frac{\rho}{K_V^*}\right)\left(\frac{1}{K_U} + \frac{\rho}{K_V}\right)\left(\frac{x}{1+\rho}\right)^2}{1 + \left(\frac{1}{K_U} + \frac{\rho}{K_V} + M_U \frac{1}{K_U} + M_V \frac{\rho}{K_V}\right)\frac{x}{1+\rho} + \left(\frac{1}{K_U^*} + \frac{\rho}{K_V^*} + M_U^* \frac{1}{K_U^*} + M_V^* \frac{\rho}{K_V^*}\right)\left(\frac{1}{K_U} + \frac{\rho}{K_V}\right)\left(\frac{x}{1+\rho}\right)^2}$$

which is then simplified as follow

$$p = \frac{F_U \frac{1}{K_U^*} + F_V \frac{\rho}{K_V^*}}{\left(\frac{1}{K_U^*} + \frac{\rho}{K^* V}\right)} \frac{1}{\frac{(1+\rho)^2}{\left(\frac{1}{K_U^*} + \frac{\rho}{K_V^*}\right)\left(\frac{1}{K_U} + \frac{\rho}{K_V}\right)x^2} + \frac{\left(\frac{1}{K_U} + \frac{\rho}{K_V} + M_U \frac{1}{K_U} + M_V \frac{\rho}{K_V}\right)(1+\rho)}{\left(\frac{1}{K_U^*} + \frac{\rho}{K_V^*}\right)\left(\frac{1}{K_U} + \frac{\rho}{K_V}\right)x} + \frac{\left(\frac{1}{K_U^*} + \frac{\rho}{K_V^*} + M_U^* \frac{1}{K_U^*} + M_V^* \frac{\rho}{K_V^*}\right)}{\left(\frac{1}{K_U^*} + \frac{\rho}{K_V^*}\right)}} =$$

$$\frac{F_U \frac{1}{K_U^*} + F_V \frac{\rho}{K_V^*}}{\frac{1}{K_U^*} + \frac{\rho}{K_V^*}} \frac{1}{\frac{(1+\rho)^2}{\left(\frac{1}{K_U^*} + \frac{\rho}{K_V^*}\right)\left(\frac{1}{K_U} + \frac{\rho}{K_V}\right)x^2} + \frac{\left(\frac{1}{K_U} + \frac{\rho}{K_V} + M_U \frac{1}{K_U} + M_V \frac{\rho}{K_V}\right)(1+\rho)}{\left(\frac{1}{K_U^*} + \frac{\rho}{K_V^*}\right)\left(\frac{1}{K_U} + \frac{\rho}{K_V}\right)x} + 1 + \frac{M_U^* \frac{1}{K_U^*} + M_V^* \frac{\rho}{K_V^*}}{\frac{1}{K_U^*} + \frac{\rho}{K_V^*}}} =$$

$$\frac{F_U \frac{1}{K_U^*} + F_V \frac{\rho}{K_V^*}}{\frac{1}{K_U^*} + \frac{\rho}{K_V^*}} \frac{1}{\frac{1+\rho}{\frac{1}{K_U^*} + \frac{\rho}{K_V^*}} \frac{1+\rho}{\frac{1}{K_U} + \frac{\rho}{K_V}} \frac{1}{x^2} + \frac{1+\rho}{\frac{1}{K_U^*} + \frac{\rho}{K_V^*}}\left(1 + \frac{M_U \frac{1}{K_U} + M_V \frac{\rho}{K_V}}{\frac{1}{K_U} + \frac{\rho}{K_V}}\right)\frac{1}{x} + 1 + \frac{M_U^* \frac{1}{K_U^*} + M_V^* \frac{\rho}{K_V^*}}{\frac{1}{K_U^*} + \frac{\rho}{K_V^*}}}$$

We call its parameters

$$F_{UV} = \frac{F_U \frac{1}{K_U^*} + F_V \frac{\rho}{K_V^*}}{\frac{1}{K_U^*} + \frac{\rho}{K_V^*}}$$

$$K_{UV}^* = \frac{1+\rho}{\frac{1}{K_U^*} + \frac{\rho}{K_V^*}}$$

$$K_{UV} = \frac{1+\rho}{\frac{1}{K_U} + \frac{\rho}{K_V}}$$

$$M_{UV} = \frac{M_U \frac{1}{K_U} + M_V \frac{\rho}{K_V}}{\frac{1}{K_U} + \frac{\rho}{K_V}}$$

$$M_{UV}^* = \frac{M_U^* \frac{1}{K_U^*} + M_V^* \frac{\rho}{K_V^*}}{\frac{1}{K_U^*} + \frac{\rho}{K_V^*}}$$

so obtaining

$$p = \frac{F_{UV}}{\frac{K_{UV}^* K_{UV}}{x^2} + \frac{K_{UV}^*}{x}(1+M_{UV}) + 1 + M_{UV}^*} \tag{9.13}$$

Finally, we have tested our model against the experimental data reported in Marasco et al. (2016) [36]. We have test whether our model fits the experimental data. This is shown in Fig. 9.1

For fitting, we have used a genetic algorithm that finds a configuration of parameters for equations of U and V that minimize the square errors for both equations of U and V, and their mixture X.

9.3 Discussion

In this chapter, we have shown our kinetic that describes the ORN dose-response. This is based on classic mechanisms and incorporate both competition and allosteric interactions.

The previous kinetic [128, 129, 130] of ORN dose-response assumed the reversibility of the product P which grades the ORN response. This implies the odor ligand can rebind with free receptor after reaction. In addition, an extended version of this kinetic was empirically defined by constraining the exponent of the odor mix-

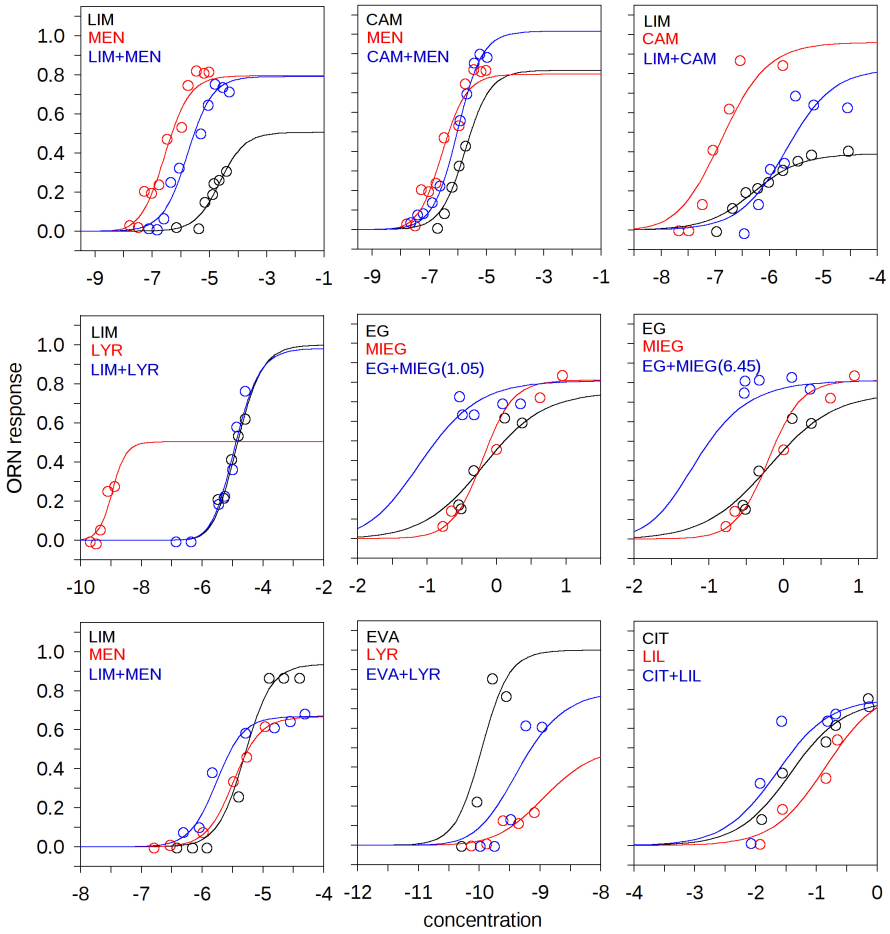

Fig. 9.1 Our model fits the experimental data.

ture, but destroying its relation with kinetic. However, this does not take into account recent suggestions that demonstrate how no synergy or inhibition should be modeled through the exponents [132], since allostery does not seem to rely on multiple binding with a single receptor. The origin of allostery should be rather researched in the structure of the kinetic itself [133]. We have therefore addressed these issues by building an extended version of Michaelis and Menten kinetic [131]. Our kinetic thus incorporates the features of both competitive and cooperative phoenomena, so it predicts both synergistic and inhibitory interactions between different odor

components within a mixture. Our model performs a better qualitative fitting of the experimental data (see Fig. 9.1) compared to previous models [36].

Further extensions, such as the *total steady state approximation*, may improve our model. The *total steady state approximation* was demonstrated to significantly improve the fitting of dose-response curves, especially with competitive kinetic [134]. However, this makes a very complicate equation set that is hard to be interpreted.

Finally, we will aim to a better characterization of the stability of our kinetic to extract the conditions that lead to synergistic and inhibitory interactions.

Chapter 10

Glomerular and Granule cells Layers coordinate temporal and spatial odor representation

A network of neurons in the OB implements information processing functions that are necessary for odor recognition. The network is organized into two layers. In the first layer, the olfactory nerves end in modules called glomeruli, where they connect to the dendrites of M/Ts, and interneurons called juxtaglomerular cells. At the second level, the M/Ts connect to GCs which are modulated by dSACs. The M/Ts connected to a given glomerulus form what we call a GU, that is obviously central to processing the olfactory input.

The results obtained with our 3D model of OB [38] suggest that a complex input signal is processed by the OB in a multistage manner. Each processing layer is independently needed but not sufficient to operate on the input in a specific way in order to obtain an output that will be further decorrelated and recombined over space and time at the next stage, in the OC.

10.1 The microcircuit of Glomerular Layer

There are different neuron populations at the GL level [8]. The current view is that they interact among themselves and with an odor input to implement two major mechanisms: (1) an olfactory bulb-wide odor input normalization, and (2) contrast enhancement generated by a local (intra-glomerular) lateral inhibition [14]. There are not enough experimental constraints to implement a biophysically real-

istic model for each neuron type. The glomerular circuitry in this work was thus represented in terms of a GU that carries out input normalization and lateral inhibition between the glomeruli, rather than in terms of explicit cells and synapses. In practice, we closely followed the approach and equations suggested by experimental and computational findings [14, 32]. A schematic representation of the equivalent microcircuits is presented in Fig. 10.1.

To take into account the olfactory bulb-wide normalization, we normalized the dose-response curves GL_i for glomerular input i (see section 5.5.2) with respect to the mean over all inputs for a given odor using the transformation:

$$\overset{*}{GL_i}(c) = \begin{cases} GL_i(c) - \overline{GL_i(c)}, & \text{if } GL_i(c) > \overline{GL_i(c)} \\ 0, & \text{otherwise} \end{cases} \tag{10.1}$$

where $\overline{GL_i(c)} = \frac{1}{N_G+1}\sum_{i=0}^{N_G} GL_i(c)$ and $\overset{*}{GL_i}(c) \in [0, 1.5]$ for all c.

To model the CE effect, we assumed that the effective activity of the PGs projecting to glomerulus i, PG_i , can be represented as

$$PG_i(c) = \begin{cases} \frac{a}{1+b\left(\frac{1}{\overset{*}{GL_i}(c)}-1\right)}, & \text{if } \overset{*}{GL_i}(c) > 0 \\ 0, & \text{otherwise} \end{cases}$$

where a and b are positive constants that are 0.6 and 0.01, respectively, the $PG_i(c)$ value will be in the range $\left[0, \frac{a}{1-\frac{b}{3}}\right]$ $\forall c$.

The resulting excitatory signal on MC tufts dendrites was finally calculated as

$$\overset{**}{GL_i}(c) = \begin{cases} \overset{*}{GL_i}(c) - PG_i(c), & \text{if } \overset{*}{GL_i}(c) > PG_i(c) \\ 0, & \text{otherwise} \end{cases} \tag{10.2}$$

The synaptic conductance in each MC described by the eqs. 5.4 and 5.5 takes into account only the (presynaptic) ORN response to a given odor concentration (eq. 5.6). To take into account the (postsynaptic) modulation due to the GL (eq. 10.1-10.2), these equations has been then extended by replacing the term $\mathrm{GL}(c)$ of

eq. 5.5 with $\overset{**}{GL_i}(c)$:

$$g(t) = \tilde{g} + \overline{g_{max}} \cdot \overset{**}{GL_i}(c) \cdot S_{ORN}(t) \tag{10.3}$$

where all terms were already explained in the section 5.5.1.

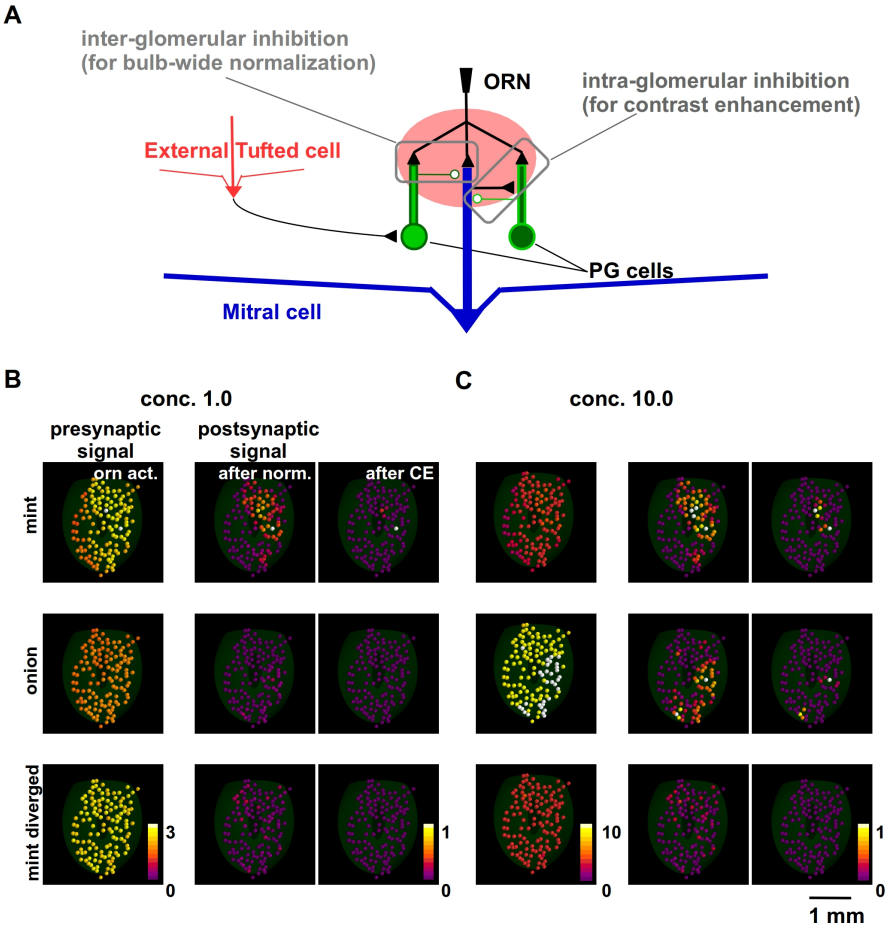

Fig. 10.1 Modeling how juxtaglomerular circuits transform natural odor inputs [105].

Based on these assumptions about the inputs, we next focused on competing mechanisms acting on the several neuron populations at the GL level [32]. In Fig. 10.2A we schematically summarize their actions. The olfactory bulb-wide odor in-

put normalization is obtained through the combined action of eTCs, SAs, and the PGs network (implemented by eq. 10.2). The CE is generated by a local (intra-glomerular) lateral inhibition mediated by periglomerular (PG) cell dendrodendritic interactions (implemented by eq. 10.2).

To illustrate the consequences of each mechanism on the input, we start with the complex input by the ORN activation levels of 127 glomeruli [53] at one arbitrary concentration ($c = 1$) of mint (top panels) and onion (middle panels). For the purpose of this analysis, a third (artificial) odor was built by randomly redistributing the mint inputs over all glomeruli (bottom panels). It should be noted that, in all panels of Fig. 10.2B, each glomerulus is color-coded using the average normalized synaptic input on the tuft dendrites of the 5 MCs belonging to it.

Their overall effect is to implement a kind of winner-take-all effect (Fig. 10.1B, right panels). The actual value of the peak synaptic conductance was chosen in such a way that the activation of the strongest input in our data (GL_i^{mint}), during an odor presentation at a relatively high concentration, was able to elicit APs in the MCs at a firing rate consistent with experimental observations (up to $\approx$100Hz). The same effect also occurs at a ten-fold higher odor concentration (Fig. 10.1C). Note that this contrast-enhancement effect is at the GL input level, and it will be reflected in the MC output.

Taken together these results support the hypothesis that GL processing generates a non-topographic contrast enhancement [14]. The spatial distribution of inputs from natural odors ends up in a configuration of MC inputs in which most of the glomeruli are inhibited below threshold, with a winner-takes-all effect that tends to isolate very few strongly active glomeruli. In agreement with experiments [49], stronger inputs (corresponding to higher odor concentrations) will progressively activate additional glomeruli, which will still be bulb-wide normalized by the GL circuit action. Note that, under these conditions, a random divergent input will not activate any glomerulus even at a relatively high concentration (Fig. 10.1 B and C, bottom panels).

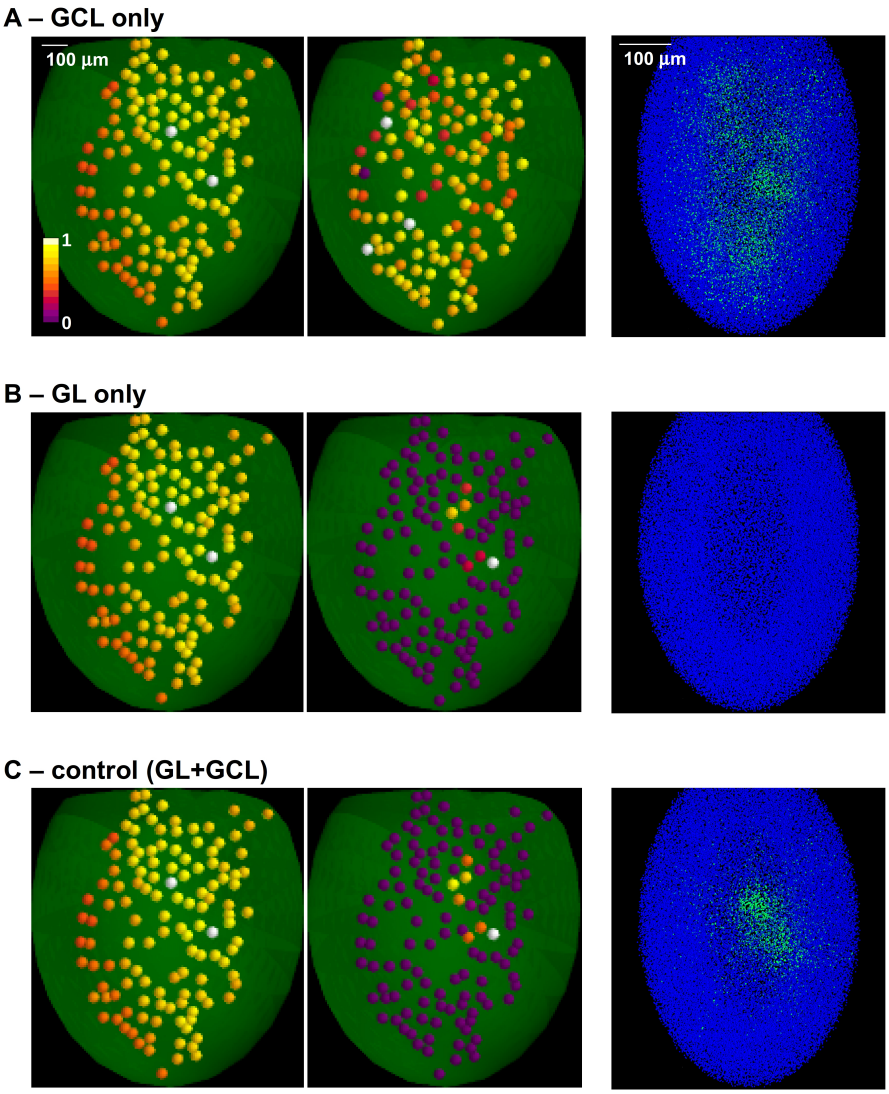

Fig. 10.2 The role of glomerular and granule cells layers in contrast enhancement [105].

In Fig. 10.2 we show the different effects of the two layers. Learning natural odor inputs with the GCL alone (Fig. 10.2A), i.e. without the GL mechanisms, would lead to a diffuse and rather uniform distribution of inhibitory GCs weights with practically no CE effect (Fig. 10.2A, right panel). This occurs because natural odors exhibit a spatially dense glomerular activation [53]. It is easy to see that,

in addition to generating a distribution of inhibitory synapses inconsistent with experimental findings [58], this spatially diffuse network configuration would prevent an effective CE action on MCs output. The GL alone would transform a dense odor representation into a sparse and contrast-enhanced one (Fig. 10.2B), but cannot generate GCL columns; both layers (Fig. 10.2C) will finally result in narrow, sparse, and segregated columns, in agreement with experimental findings [58, 29].

10.2 Natural odor learning and its consequence on the mitral cells firing

In the previous sections we have studied the interactions between isolated glomerular units. Complex odors however require interactions among many units. We have therefore used our full model, which has led to new insights into mechanisms related to learning of natural odors.

We first note that, since a column can form only below the glomeruli which are strongly active during odor training [80], the presence of a column in a particular spatial location in the olfactory bulb can be related to odor identity and concentration. Furthermore, a column can also affect information propagation and decorrelation of other columns [39]. Experimentally, the most important mechanism from this point of view seems to be the decorrelation that an odor pattern undergoes after a few hundred milliseconds from a sniff onset [42]. It is therefore important to explore this issue in more detail, starting from the process of column formation following training with different odors in the full model.

For each natural odor we fixed a concentration level to have at least one glomerular unit sufficiently activated to form a column. Odors mint, kiwi, and cloves were thus sequentially presented as inputs. In all simulations, every odor lasted for 7 and 5 sec during the learning or testing phase, respectively, whereas all glomeruli were activated every second to reproduce a sniffing frequency of 1 Hz. The column configuration after each odor presentation is illustrated in Fig. 10.3, where we plot the

spatial distribution of the inputs on the MC tufts (Fig. 10.3, top), the network configuration in terms of GCs with strong synapses (Fig. 10.3, middle), and the column distribution that would be observed with different slices (Fig. 10.3, bottom). Interestingly, the shape, size, and distribution of the columns reproduce the same features observed in experiments [58, 29]; new, relatively well-demarcated, columns were formed after every odor learned.

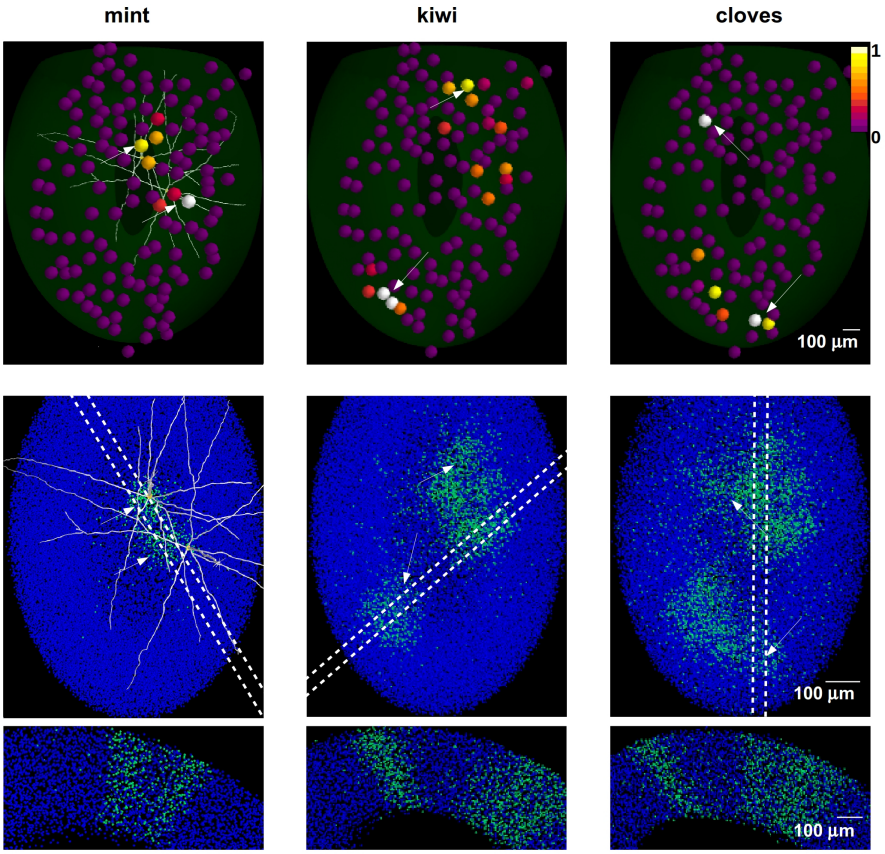

Fig. 10.3 Mitral-granule cell network configuration after learning different odors [105].

To see how this network configuration affects unknown odor inputs, we studied, with and without the GL, the MC firing pattern and evoked by three odors: mint (known), pineapple (unknown), and chocolate (unknown). The results are shown in

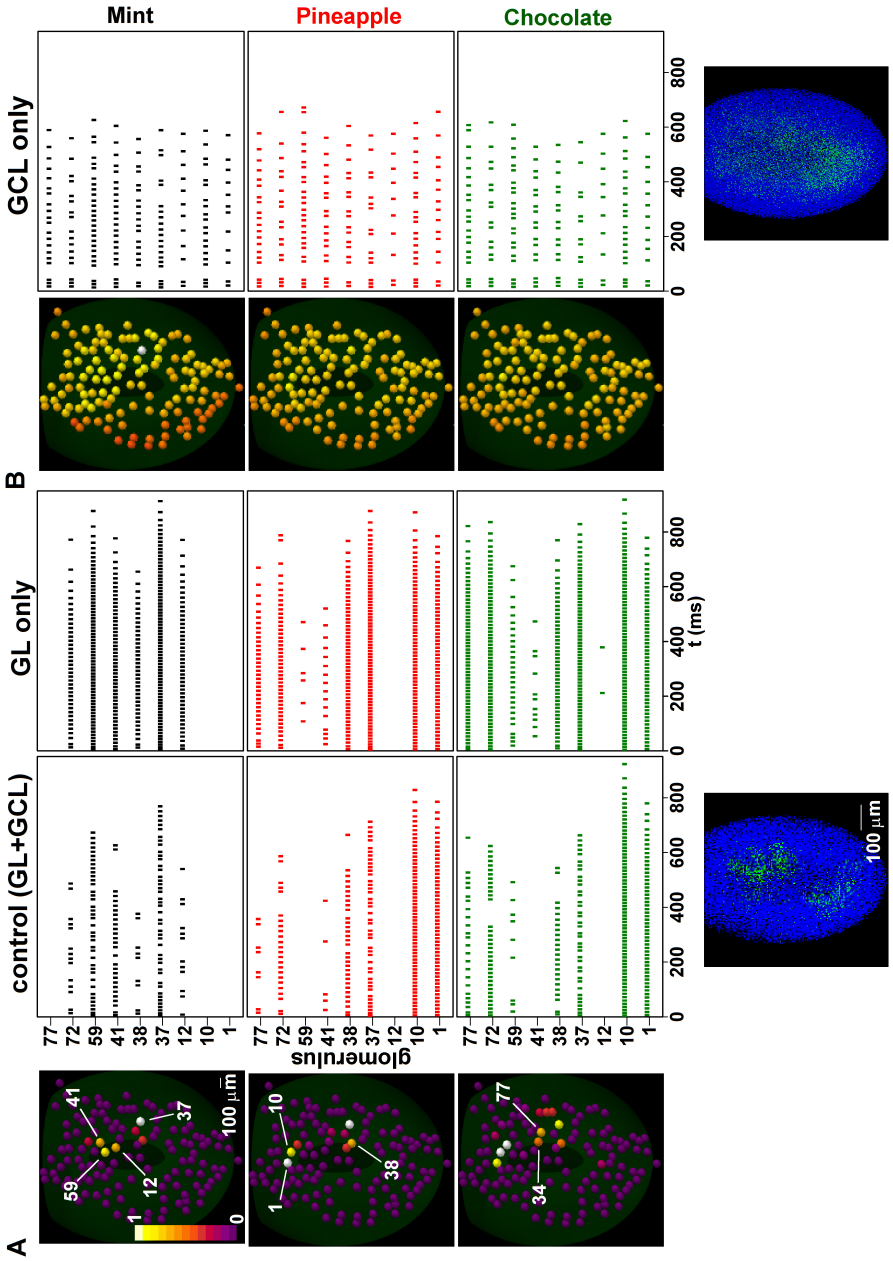

Fig. 10.4 Learning increases spatial decorrelation of inputs [105].

Fig.10.4. We chose these odors because of their somewhat overlapping glomerular activation, schematically represented in the left panels of Fig. 10.4A. Training with both layers (Fig. 10.4A, center panels), resulted in most glomeruli responding with different patterns for different odors, and well defined columns (Fig. 10.4A, plot below control panels). This effect was clearly correlated with both lateral and feedback inhibition. Although MCs not involved in the training period (e.g. 1 and 10, activated by Pineapple and Chocolate) did not show any significant change, as they did not have any associated column, most of the other MCs showed some sign of interaction, in the form of change in the spiking temporal distribution. From this point of view, an entire repertoire of features can be distinguished already with this relatively simple configuration, from complete inhibition of glomerular unit activity (e.g. 12, 59, 41) to characteristic bursting properties (e.g. 12, 38, and 72) that depend on the specific spatial interaction among active glomerular units and could be used to identify an odor input. Overall, these patterns were similar to what has been observed experimentally [47]. Moreover, those MCs associated with a column exhibited a burst-like activity during the ORN stimulus time course, due to the feedback inhibition evoked from the connected GCs. This is consistent with experimental results, which show a burst-like activity when a current was injected during the simulated ORN response pattern [13]. Without the GCL (Fig. 10.4A, right panels), all odors evoked a rather strong activity. Many glomerular units were more or less activated by all three odors, with spiking patterns that lasted for the entire time course of the MC tuft response to ORN activation (see section 5.5.2 and fig. 5.8). Without the GL processing, odor presentation evoked a dense glomerular activity (Fig. 10.4B, left panels). Under this condition, training formed a diffuse cloud of inhibitory GCs weights (Fig. 10.4B, bottom left) that resulted in all glomerular units substantially responding to all odors in a similar way (Fig. 10.4B, right panels). Taken together, these results demonstrate why both layers are needed to process natural odors.

10.3 Spatio-temporal odor representation after learning

10.3.1 The spatial overlap over time

For a more quantitative measure of the effects on glomerular unit interactions during a sniff, we analyzed how the spatial activity patterns were affected by training at different time windows from the sniff onset (0-40, 40-80 and 80-120 ms). For this purpose, we calculated the spatiotemporal overlap, between any given odor pair (Fig. 10.5, bottom), as the cosine between the vectors formed by the average spike number of the MCs belonging to each glomerulus within each time window. Because glomeruli have a fixed spatial location, these vectors can represent the spatial activity pattern of the olfactory bulb. Each pair exhibited a distinct level of spatial overlap, depending on their spatial and temporal activation.

Before training (Fig. 10.5A), odors exhibited more or less overlap that depended on the spatial distribution of the active glomeruli. Chocolate was relatively less overlapping with mint with respect to pineapple during the entire observed period (compare overlap table for mint-choc and pine-choc in Fig. 10.5A). Mint and pineapple instead exhibited a time dependent overlap that was maximum in the 40-80 ms window. These values were entirely dependent on the relative strength and time course of the glomerular input for each odor. It should be noted that this configuration corresponds to an OB in which there are only GL circuits.

Training (Fig. 10.5B) resulted in an overall activity reduction in nearly all glomeruli, especially those activated by an odor already known to the network (such as mint), and thus with well-formed columns (see the right panel of Fig. 10.2C and the left panels of Fig. 10.3). Although this reduction was already evident in the time window just after the stimulus onset, the overlap among odor pairs (especially for those unknown to the network) was not affected during the same period. However, it was systematically reduced in all odor pairs during the time course of the stimulus. It should be stressed that this effect cannot be obtained without the GL circuit (Fig. 10.6). These results suggest that the GCs can strongly change the spatiotemporal

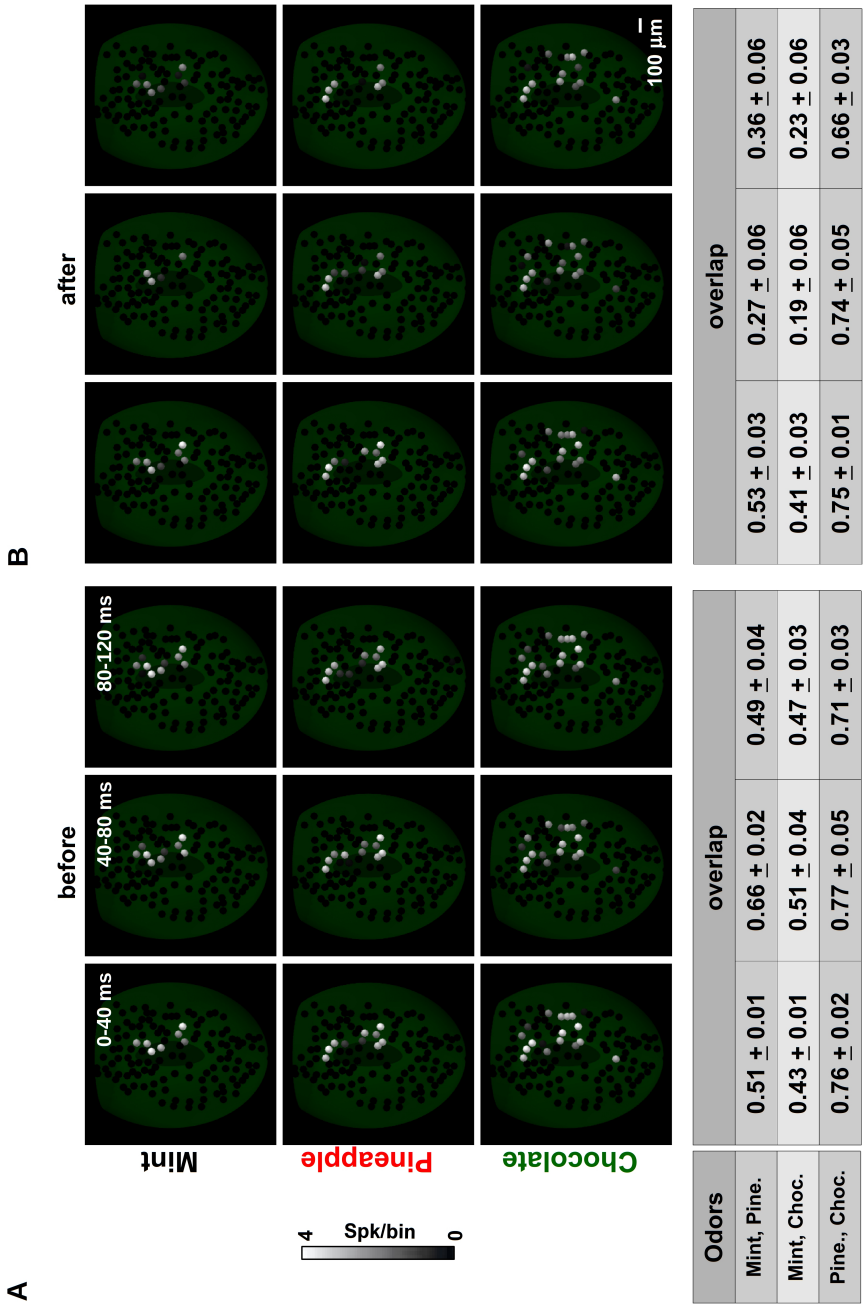

Odors			overlap
Mint, Pine.	0.51 ± 0.01	0.66 ± 0.02	0.49 ± 0.04
Mint, Choc.	0.43 ± 0.01	0.51 ± 0.04	0.47 ± 0.03
Pine., Choc.	0.76 ± 0.02	0.77 ± 0.05	0.71 ± 0.03

			overlap
	0.53 ± 0.03	0.27 ± 0.06	0.36 ± 0.06
	0.41 ± 0.03	0.19 ± 0.06	0.23 ± 0.06
	0.75 ± 0.01	0.74 ± 0.05	0.66 ± 0.03

Fig. 10.5 Spatial mitral cell activity decorrelates over time after learning [105].

structure of the MC spikes in such a way as to disambiguate similar input patterns. The overall effect is consistent with experimental findings [6, 42], and our model predicts that it will be stronger for odor pairs containing a known component (mint, in this case) and lower for unknown odors.

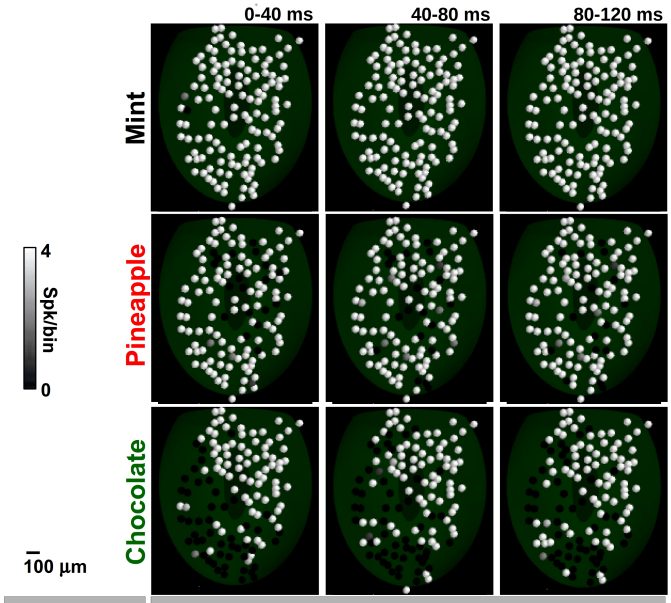

Odors	overlap		
Mint, Pine.	0.793 ± 0.037	0.913 ± 0.012	0.901 ± 0.007
Mint, Choc.	0.731 ± 0.037	0.891 ± 0.019	0.898 ± 0.015
Pine., Choc.	0.854 ± 0.028	0.948 ± 0.012	0.929 ± 0.011

Fig. 10.6 GCL alone cannot decorrelate mitral cell activity over time [105].

In summary, odor learning reduced the relative overlap between each odor couple, therefore enhancing the differences between the related spatial activity patterns and the odor discrimination abilities of the olfactory bulb. This is in accord with cognitive testing that has revealed that odor learning gives significantly improved discrimination accuracy in rats [19, 44, 22].

The overlap reduction is dependent on the presence of well-formed columns, which are essential for this mechanism to work. Columns with an inhibitory action

that is not spatially segregated or strong enough will not work well to reduce the input overlap. A columns size, shape, and overall effect on action potential back-propagation depend on the peak inhibitory synaptic conductance [39] and, more generally, on the balance between excitation and inhibition [62]. The control conditions used in our model can be considered as balanced, from this point of view.

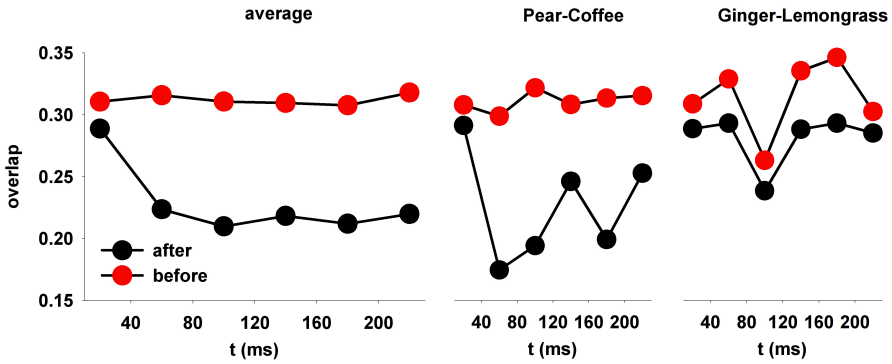

Fig. 10.7 After learning, the spatial overlap in average firing rate decreases over time [105].

We then tested how a column can change the input overlap using peak inhibitory conductance values half or double compared with control. After training, the same odors were presented to compare the relative overlap average between each odor couple. The results reported in Table 1 show how significant deviation from a balanced (control) condition results in a worse and less stable reduction of the overlap between input patterns, suggesting an impaired discrimination of odors.

The average change in the overlap, obtained after testing the model trained with 3 odors, was calculated from all possible pairs of 19 natural odors (Fig. 10.7). Before training (Fig. 10.7, red symbols), the overlap was relatively high and constant throughout the sniff. After training, it was significantly reduced within 80 ms ($p < 0.001$) within all time windows for each odor couple. This was observed for many (but not all) pairs, as shown in the middle and right panels of Fig. 10.7.

In summary, these results show what computations are performed by the GCs during odor learning. GCs decorrelate the odor representation by glomerular units over time. For this to occur, well-formed columns are necessary. These results help

to explain why the olfactory cortical representation of odors exhibits a reduced overlap compared to the GL [48], and why zero-noise correlation occurs between the neurons of the anterior pyriform cortex during odor recognition [41].

Table 1 Overlap in average firing rate for different peak inhibitory conductances.

	0-40 (ms)	**40-80 (ms)**	**80-120 (ms)**
Control	0.57 ± 0.15	0.40 ± 0.25	0.42 ± 0.19
half inh.	0.57 ± 0.15	0.47 ± 0.21	0.44 ± 0.18
double inh.	0.56 ± 0.14	0.37 ± 0.30	0.46 ± 0.18

10.3.2 The relative spatial overlap between odor pairs

We finally consider that with learning of an increasing number of odors, it may be predicted that the columns will gradually merge into a large, structurally undefined, set of strongly potentiated synapses. This could be especially true for complex natural odors, as those explored in this work.

To study this effect, the difference in the correlation between odor pairs before and after training with different odors was calculated (Fig. 10.8B). Brighter pixels indicate a progressively larger decorrelation. As can be gathered by the increasing number of brighter pixels, odors were more and more decorrelated with training. However, after training with all 19 odors the decorrelation appeared to be much reduced or absent. In Fig. 10.8C we plot the average change in correlation between any two odors as a function of the number of trained odors. Taken together these results suggest that there may be an optimal number of odors on which the olfactory bulb can operate at any given time.

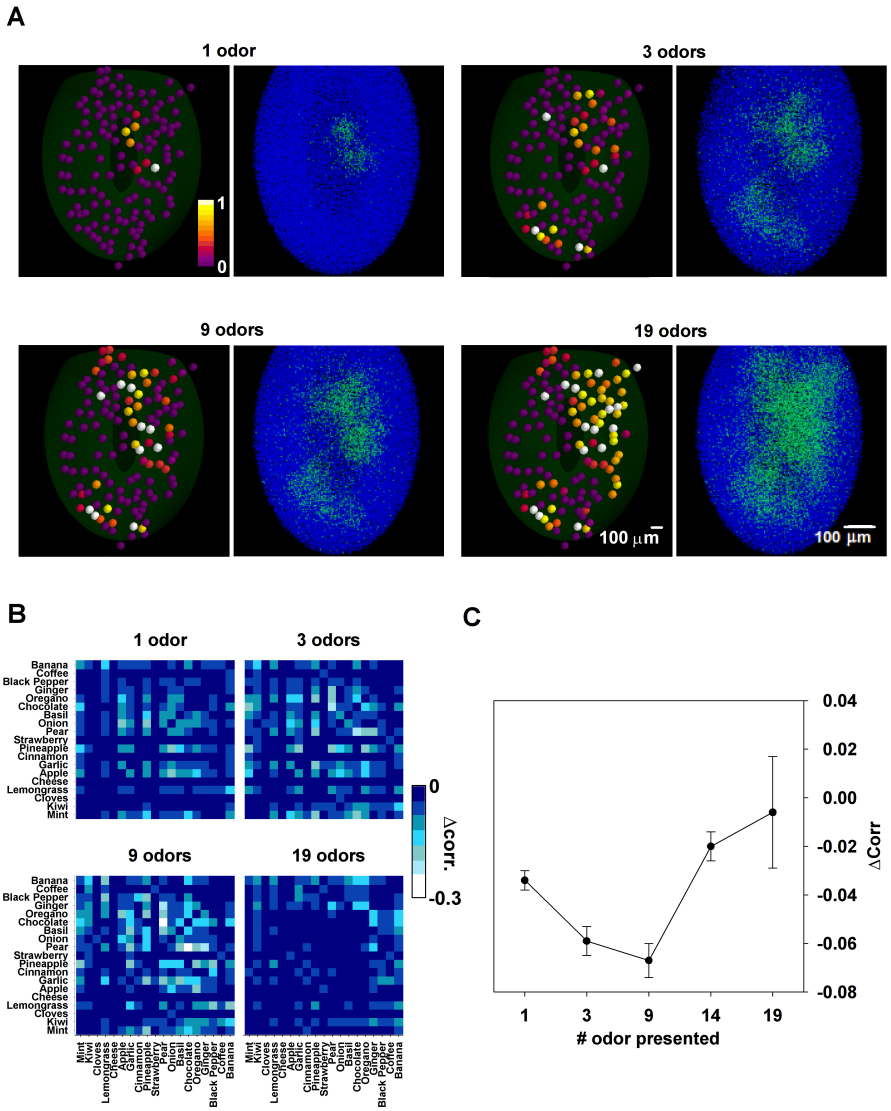

Fig. 10.8 Odor learning affects the relative spatial overlap between odor pairs [105].

10.4 Discussion

The overall picture emerging from the results of this study is one in which a complex odor signal is processed in a multistage manner, at the GL and GCL. Each processing layer is independently needed (but not sufficient) to operate on the input

in a specific way. We summarize the findings and their interrelation with regard to contrast enhancement in the GL and temporal decorrelation in the GCL.

To begin, an initial preparatory stage takes place in the olfactory neuron input. As summarized in Fig. 10.9, natural odor molecules have a dense input representation in terms of populations of activated glomeruli [53], even at relatively low concentrations. In contrast, monomolecular odor molecules activate only few glomeruli. Representing this natural odor distribution is novel in our 3D model [38]. We show here that it is key to the sequence of operations.

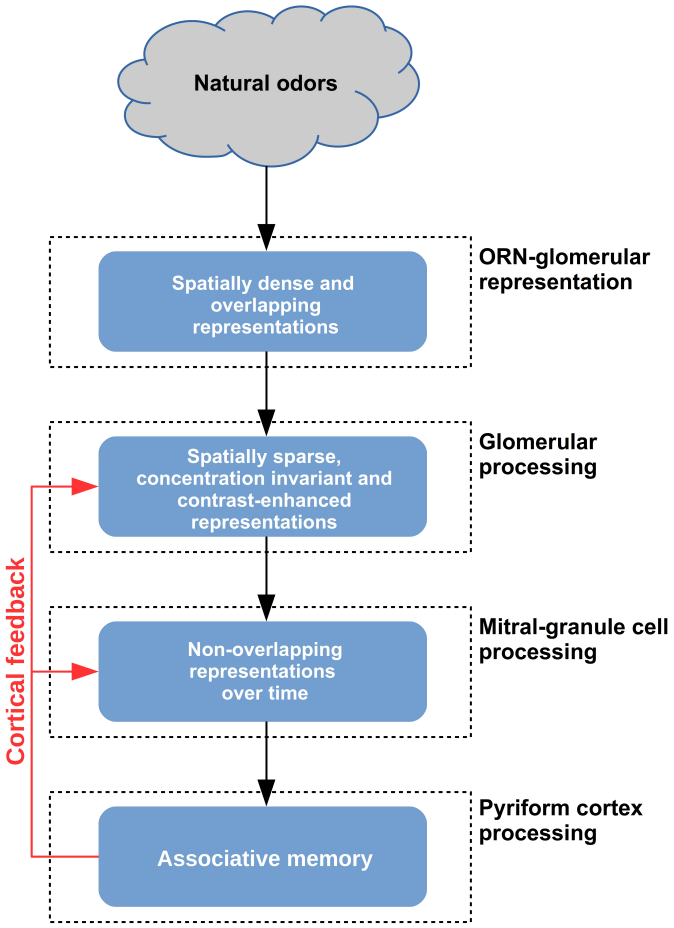

Fig. 10.9 Schematic representation of the functional consequences of glomerular and granule cell layers in the olfactory bulb [105].

At the next stage (Fig. 10.9, second layer), the fundamental role of the GL is to make the input spatially decorrelated and sparse. This is accomplished through a winner-takes-all processing that selects only strongly active glomeruli (Fig. 10.1). We have shown that this process cannot be implemented by the GCL in the presence of the dense input activated by natural odors (Fig. 10.2 and 10.3B). The effect of this mechanism, mainly operating through juxtaglomerular cells, was shown in a reduced network of the GL with simplified artificial inputs [33]. Here we extended its validity and scope by applying it in our realistic 3D model.

At the final stage (Fig. 10.9) in the GCL we show that several critical operations take place. GCL processing is needed for column formation and interaction, during learning, and to add temporal processing and additional spatial decorrelation, during odor presentation. These mechanisms operate following the odor-dependent activation of the MCs and their reciprocal synapses within the GC network; according to the columns present at any given time, the MC output in the presence of different inputs is spatially sparse and decorrelated over time (Fig. 10.5B). We show that the process cannot be properly implemented without a GL preprocessing (Fig. 10.6).

The model suggests that this interaction can be especially important during odor learning, which relies on synaptic plasticity at the mitral-granule circuit level. We stress that, although synaptic plasticity has not been directly observed in the reciprocal mitral-granule cell synapses, there are several indirect experimental findings suggesting its occurrence in the olfactory bulb [35] and in the mitral [17, 34] and GCs [20, 7]. This is an important issue, and we plan to investigate alternative hypotheses in a future work.

Our approach makes it possible to put into this same framework a number of theoretical and experimental findings. Juxtaglomerular cells in the GL act through interglomerular and local interaction with the mitral cells [32, 14]. By contrast, GCs in the GCL operate on MCs through feedback and lateral inhibition over time and a larger spatial domain. This temporal processing and synchronization was predicted in the original description of the dendrodendritic interactions [87, 86]. Their concurrent action is such that, within $\approx$150 ms from the stimulus onset [51], the output

of the olfactory bulb is temporally morphed [42] and spatially organized to form a code that is theoretically sufficient to explain all of the human and rodent abilities to discriminate odors [30].

The model results especially highlight the fundamental role of GL circuits for processing natural odors. Under the evoked dense spatial activation of glomeruli [53], the GCs cannot form the narrow and well-defined columns that are needed to decrease the relative overlap between odor representations after learning. The overall picture is consistent with experimental findings suggesting that the lateral inhibition relies more on the GL circuits, whereas the relatively lower GC inhibition is likely to implement MC synchronization [57].

An interesting prediction of the model is the limitation on the number of odors that can be learned by the olfactory bulb before reaching its computational limit. Although we did not test low odor concentrations, which can result in column erasure [40], it should be clear that presentation of a number of odors at concentrations high enough to form a column will eventually overwhelm the sparse and distributed glomerular column organization. We hypothesize that external mechanisms, such as neurogenesis, cortical feedback [43], or neuromodulatory inputs from other brain regions, may help to expand this limit. These results have all been obtained with a model based on the glomeruli in the dorsal region representing approximately 10% of the olfactory bulb. Obviously the rest of the olfactory bulb greatly expands the numbers of odors that can be discriminated.

Finally, the model results in decorrelation of odor pairs, suggesting the behavioral prediction that specific odors pair may be discriminated according to individual recent odor experience. The direct use of experimental data on natural odors allows specific predictions, assuming that the distribution of the inputs in the dorsal part of the olfactory bulb is a good representation of the odor. Thus, for example, in the model, recent odor learning of mint, kiwi, and cloves should result in a better discrimination between pear and coffee, and a much more confused discrimination between ginger and lemongrass. The next step will be to extend this approach to the entire olfactory bulb.

References

1. Koch, K. (2005). Biophysics of Computation: Information Processing in Single Neurons. Oxford University Press.
2. Street, S.E., Manis, P.B. (2007). Action potential timing precision in dorsal cochlear nucleus pyramidal cells. J Neurophysiol. 97(6):4162-4672.
3. Torkkeli, P.H., Panek, I. (2002). Neuromodulation of arthropod mechanosensory neurons. Microsc Res Tech. 58(4):299-311.
4. Shepherd, G. M., Chen, W. R., and Greer, C. A. (2004). Olfactory bulb, in The Synaptic Organization of the Brain, 5th Edn., ed. G. M. Shepherd (New York, NY: Oxford University Press), 165-216. doi: 10.1093/acprof:oso/9780195159561.001.1
5. Hodgkin, A.L., Huxley, A.F. (1952). Currents carried by sodium and potassium ions through the membrane of the giant axon of Loligo. The Journal of Physiology. 116(4):449-72. doi:10.1113/jphysiol.1952.
6. Abraham, N. M., Spors, H., Carleton, A., Margrie, T. W., Kuner, T., and Schaefer, A. T. (2004). Maintaining accuracy at the expense of speed: stimulus similarity defines odor discrimination time in mice. Neuron 44, 865876. doi: 10.1016/j.neuron.2004.11.017
7. Arenkiel, B. R., Hasegawa, H., Yi, J. J., Larsen, R. S., Wallace, M. L., Philpot, B. D., et al. (2011). Activity-induced remodeling of olfactory bulb microcircuits revealed by monosynaptic tracing. PLoS ONE 6:e29423. doi: 10.1371/journal.pone.0029423
8. Aungst, J. L., Heyward, P. M., Puche, A. C., Karnup, S. V., Hayar, A., Szabo, G., et al. (2003). Centre-surround inhibition among olfactory bulb glomeruli. Nature 426, 623629. doi: 10.1038/nature02185
9. Bartel, D. L., Rela, L., Hsieh, L., and Greer, C. A. (2015). Dendrodendritic synapses in the mouse olfactory bulb external plexiform layer. J. Comp. Neurol. 523, 11451161. doi: 10.1002/cne.23714
10. Benjaminsson, S., Herman, P., and Lansner, A. (2013). Performance of a computational model of the mammalian olfactory system, in Neuromorphic Olfaction, Chapter 6, eds K. C. Persaud, S. Marco, and A. Gutirrez-Glvez (Boca Raton, FL: CRC Press, Taylor and Francis), 174207.
11. Buck, L. B. (1993). Receptor diversity and spatial patterning in the mammalian olfactory system. Ciba Found. Symp. 179, 5164.
12. Carey, R. M., Verhagen, J. V., Wesson, D. W., Prez, N., and Wachowiak, M. (2009). Temporal structure of receptor neuron input to the olfactory bulb imaged in behaving rats. J. Neurophysiol. 101, 10731088. doi: 10.1152/jn.90902.2008
13. Chen, W. R., and Shepherd, G. M. (1997). Membrane and synaptic properties of mitral cells in slices of rat olfactory bulb. Brain Res. 745, 189196. doi: 10.1016/S0006-8993(96)01150-X

14. Cleland, T. A., and Sethupathy, P. (2006). Non-topographical contrast enhancement in the olfactory bulb. BMC Neurosci. 7:7. doi: 10.1186/1471-2202-7-7
15. Destexhe, A., Mainen, Z. F., and Sejnkowski, T. J. (1998). Kinetic models of synaptic transmission, in Methods in Neuronal Modeling, eds C. Koch and I. Segev (Cambridge, MA: MIT Press), 1214.
16. Destexhe, A., Rudolph, M., Fellous, J. M., and Sejnowski, T. J. (2001). Fluctuating synaptic conductances recreate in vivo-like activity in neocortical neurons. Neuroscience 107, 1324. doi: 10.1016/S0306-4522(01)00344-X
17. Ennis, M., Linster, C., Aroniadou-Anderjaska, V., Ciombor, K., and Shipley, M. T. (1998). Glutamate and synaptic plasticity at mammalian primary olfactory synapses. Ann. N.Y. Acad. Sci. 855, 457466. doi: 10.1111/j.1749-6632.1998.tb10606.x
18. Fantana, A. L., Soucy, E. R., and Meister, M. (2008). Rat olfactory bulb mitral cells receive sparse glomerular inputs. Neuron 59, 802814. doi: 10.1016/j.neuron.2008.07.039
19. Fletcher, M. L., and Wilson, D. A. (2002). Experience modifies olfactory acuity: acetylcholine-dependent learning decreases behavioral generalization between similar odorants. J. Neurosci. 22, RC201.
20. Gao, Y., and Strowbridge, B. W. (2009). Long-term plasticity of excitatory inputs to granule cells in the rat olfactory bulb. Nat. Neurosci. 12, 731733. doi: 10.1038/nn.2319
21. Giridhar, S., Doiron, B., and Urban, N. N. (2011). Timescale-dependent shaping of correlation by olfactory bulb lateral inhibition. Proc. Natl. Acad. Sci. U.S.A. 108, 58435848. doi: 10.1073/pnas.1015165108
22. Gschwend, O., Abraham, N. M., Lagier, S., Begnaud, F., Rodriguez, I., and Carleton, A. (2015). Neuronal pattern separation in the olfactory bulb improves odor discrimination learning. Nat. Neurosci. 18, 14741482. doi: 10.1038/nn.4089
23. Gschwend, O., Beroud, J., and Carleton, A. (2012). Encoding odorant identity by spiking packets of rate-invariant neurons in awake mice. PLoS ONE 7:e30155. doi: 10.1371/journal.pone.0030155
24. Hines, M., and Carnevale, N. T. (1997). The NEURON simulation environment. Neural Comput. 9, 11791209. doi: 10.1162/neco.1997.9.6.1179
25. Isaacson, J. S., and Vitten, H. (2003). GABA(B) receptors inhibit dendrodendritic transmission in the rat olfactory bulb. J. Neurosci. 23, 20322039
26. Jaynes, E. T. (1963). Information theory and statistical mechanics, in Statistical Physics, ed K. Ford (New York, NY: Benjamin), 181.
27. Johnson, B. A., and Leon, M. (2007). Chemotopic odorant coding in a mammalian olfactory system. J. Comp. Neurol. 503, 134. doi: 10.1002/cne.21396
28. Kepecs, A., Uchida, N., and Mainen, Z. F. (2007). Rapid and precise control of sniffing during olfactory discrimination in rats. J. Neurophysiol. 98, 205213. doi: 10.1152/jn.00071.2007

29. Kim, D. H., Phillips, M. E., Chang, A. Y., Patel, H. K., Nguyen, K. T., and Willhite, D. C. (2011). Lateral connectivity in the olfactory bulb is sparse and segregated. Front. Neural Circuits 5:5. doi: 10.3389/fncir.2011.00005
30. Koulakov, A., Gelperin, A., and Rinberg, D. (2007). Olfactory coding with all-or-nothing glomeruli. J. Neurophysiol. 98, 31343142. doi: 10.1152/jn.00560.2007
31. Labarrera, C., London, M., and Angelo, K. (2013). Tonic inhibition sets the state of excitability in olfactory bulb granule cells. J. Physiol. 591, 18411850 doi: 10.1113/jphysiol.2012.241851
32. Linster, C., and Cleland, T. A. (2009). Glomerular microcircuits in the olfactory bulb. Neural Netw. 22, 11691173. doi: 10.1016/j.neunet.2009.07.013
33. Linster, C., and Cleland, T. A. (2010). Decorrelation of odor representations via spike timing-dependent plasticity. Front. Comput. Neurosci. 4:157. doi: 10.3389/fncom.2010.00157
34. Ma, T. F., Zhao, X. L., Cai, L., Zhang, N., Ren, S. Q., Ji, F., et al. (2012). Regulation of spike timing-dependent plasticity of olfactory inputs in mitral cells in the rat olfactory bulb. PLoS ONE 7:e35001. doi: 10.1371/journal.pone.0035001
35. Mandairon, N., and Linster, C. (2009). Odor perception and olfactory bulb plasticity in adult mammals. J. Neurophysiol. 101, 22042209. doi: 10.1152/jn.00076.2009
36. Marasco, A., De Paris, A., and Migliore, M. (2016). Predicting the response of olfactory sensory neurons to odor mixtures from single odor response. Sci Rep. 6:24091. doi: 10.1038/srep24091
37. McTavish, T. S., Migliore, M., Shepherd, G. M., and Hines, M. L. (2012). Mitral cell spike synchrony modulated by dendrodendritic synapse location. Front. Comput. Neurosci. 6:3. doi: 10.3389/fncom.2012.00003
38. Migliore, M., Cavarretta, F., Hines, M. L., and Shepherd, G. M. (2014). Distributed organization of a brain microcircuit analyzed by three-dimensional modeling: the olfactory bulb. Front. Comput. Neurosci. 8:50. doi: 10.3389/fncom.2014.00050
39. Migliore, M., Cavarretta, F., Marasco, A., Tulumello, E., Hines, M. L., and Shepherd, G. M. (2015). Synaptic clusters function as odor operators in the olfactory bulb. Proc. Natl. Acad. Sci. U.S.A. 112, 84998504. doi: 10.1073/pnas.1502513112
40. Migliore, M., Hines, M. L., McTavish, T. S., and Shepherd, G. M. (2010). Functional roles of distributed synaptic clusters in the mitral-granule cell network of the olfactory bulb. Front. Integr. Neurosci. 4:122. doi: 10.3389/fnint.2010.00122
41. Miura, K., Mainen, Z. F., and Uchida, N. (2012). Odor representations in olfactory cortex: distributed rate coding and decorrelated population activity. Neuron 74, 10871098. doi: 10.1016/j.neuron.2012.04.021
42. Niessing, J., and Friedrich, R. W. (2010). Olfactory pattern classification by discrete neuronal network states. Nature 2465, 4752. doi: 10.1038/nature08961

43. Otazu, G. H., Chae, H., Davis, M. B., and Albeanu, D. F. (2015). Cortical feedback decorrelates olfactory bulb output in awake mice. Neuron 86, 14611477. doi: 10.1016/j.neuron.2015.05.023

44. Rokni, D., Hemmelder, V., Kapoor, V., and Murthy, V. N. (2014). An olfactory cocktail party: figure-ground segregation of odorants in rodents. Nat. Neurosci. 17, 12251232. doi: 10.1038/nn.3775

45. Schoppa, N. E., Kinzie, J. M., Sahara, Y., Segerson, T. P., and Westbrook, G. L. (1998). Dendrodendritic inhibition in the olfactory bulb is driven by NMDA receptors. J. Neurosci. 18, 67906802.

46. Shannon, C. E. (1948). A mathematical theory of communication. Bell Syst. Tech. J. 27, 379423. doi: 10.1002/j.1538-7305.1948.tb01338.x

47. Shusterman, R., Smear, M. C., Koulakov, A. A., and Rinberg, D. (2011). Precise olfactory responses tile the sniff cycle. Nat. Neurosci. 14, 10391044. doi: 10.1038/nn.2877

48. Stettler, D. D., and Axel, R. (2009). Representations of odor in the piriform cortex. Neuron 63, 854864. doi: 10.1016/j.neuron.2009.09.005

49. Strauch, M., Ditzen, M., and Galizia, C. G. (2012). Keeping their distance? Odor response patterns along the concentration range. Front. Syst. Neurosci. 6:71. doi: 10.3389/fnsys.2012.00071

50. Sullivan, S. L., Ressler, K. J., and Buck, L. B. (1994). Odorant receptor diversity and patterned gene expression in the mammalian olfactory epithelium. Prog. Clin. Biol. Res. 390, 7584.

51. Uchida, N., and Mainen, Z. F. (2003). Speed and accuracy of olfactory discrimination in the rat. Nat. Neurosci. 11, 12241229. doi: 10.1038/nn1142

52. Urban, N. N., and Sakmann, B. (2002). Reciprocal intraglomerular excitation and intra- and interglomerular lateral inhibition between mouse olfactory bulb mitral cells. J. Physiol. 542, 355367. doi: 10.1113/jphysiol.2001.013491

53. Vincis, R., Gschwend, O., Bhaukaurally, K., Beroud, J., and Carleton, A. (2012). Dense representation of natural odorants in the mouse olfactory bulb. Nat. Neurosci. 15, 537539. doi: 10.1038/nn.3057

54. Vizcay, M. A., Duarte-Mermoud, M. A., and Aylwin Mde, L. (2015). Odorant recognition using biological responses recorded in olfactory bulb of rats. Comput. Biol. Med. 56, 192199. doi: 10.1016/j.compbiomed.2014.10.010

55. Wachowiak, M., and Cohen, L. B. (2001). Representation of odorants by receptor neuron input to the mouse olfactory bulb. Neuron 32, 723735. doi: 10.1016/S0896-6273(01)00506-2

56. Wachowiak, M., and Shipley, M. T. (2006). Coding and synaptic processing of sensory information in the glomerular layer of the olfactory bulb. Semin. Cell. Dev. Biol. 17, 411423. doi: 10.1016/j.semcdb.2006.04.007

57. Whitesell, J. D., Sorensen, K. A., Jarvie, B. C., Hentges, S. T., and Schoppa, N. E. (2013). Inter-glomerular lateral inhibition targeted on external tufted cells in the olfactory bulb. J. Neurosci. 33, 15521563. doi: 10.1523/JNEUROSCI.3410-12.2013

58. Willhite, D. C., Nguyen, K. T., Masurkar, A. V., Greer, C. A., Shepherd, G. M., and Chen, W. R. (2006). Viral tracing identifies distributed columnar organization in the olfactory bulb. Proc. Natl. Acad. Sci. U.S.A. 103, 1259212597. doi: 10.1073/pnas.0602032103

59. Woolf, T. B., Shepherd, G. M., and Greer, C. A. (1991). Serial reconstructions of granule cell spines in the mammalian olfactory bulb. Synapse 7, 181192. doi: 10.1002/syn.890070303

60. Xu, F., Liu, N., Kida, I., Rothman, D. L., Hyder, F., Shepherd, G. M., et al. (2003). Odor maps of aldehydes and esters revealed by functional MRI in the glomerular layer of the mouse olfactory bulb. Proc. Natl. Acad. Sci. U.S.A. 100, 1102911034.

61. Yokoi, M., Mori, K., and Nakanishi, S. (1995). Refinement of odor molecule tuning by dendrodendritic synaptic inhibition in the olfactory bulb. Proc. Natl. Acad. Sci. U.S.A. 92, 33713375. doi: 10.1073/pnas.92.8.3371

62. Yu, Y., Migliore, M., Hines, M. L., and Shepherd, G. M. (2014). Sparse coding and lateral inhibition arising from balanced and unbalanced dendrodendritic excitation and inhibition. J. Neurosci. 34, 1370113713. doi: 10.1523/JNEUROSCI.1834-14.2014

63. Cang, J., and Isaacson, J. S. (2003). In vivo whole-cell recording of odor-evoked synaptic transmission in the rat olfactory bulb. J. Neurosci. 23, 41084116.

64. Chen, W. R., Shen, G. Y., Shepherd, G. M., Hines, M. L., and Midtgaard, J. (2002). Multiple modes of action potential initiation and propagation in mitral cell primary dendrite. J. Neurophysiol. 88, 27552764. doi: 10.1152/jn.00057.2002

65. Cleland, T. A., and Linster, C. (2005). Computation in the olfactory system. Chem Senses. 30, 801813. doi: 10.1093/chemse/bji072

66. Cleland, T. A., and Linster, C. (2012). On-center/inhibitory-surround decorrelation via intraglomerular inhibition in the olfactory bulb glomerular layer. Front. Integr. Neurosci. 6:5. doi: 10.3389/fnint.2012.00005

67. Cuntz, H., Forstner, F., Borst, A., and Husser, M. (2010). One rule to grow them all: a general theory of neuronal branching and its practical application. PLoS Comput Biol. 6:8. doi: 10.1371/journal.pcbi.1000877

68. Davison, A. P., Feng, J., and Brown, D. (2003). Dendrodendritic inhibition and simulated odor responses in a detailed olfactory bulb network model. J. Neurophysiol. 90, 19211935. doi: 10.1152/jn.00623.2002

69. Debarbieux, F., Audinat, E., and Charpak, S. (2003). Action potential propagation in dendrites of rat mitral cells in vivo. J. Neurosci. 23, 55535560.

70. Donohue, D. E., and Ascoli, G. A. (2008). A comparative computer simulation of dendritic morphology. PLoS Comput Biol. 4:e1000089. doi: 10.1371/journal.pcbi.1000089

71. Egaa, J. I., Aylwin, M. L., and Maldonado, P. E. (2005). Odor response properties of neighboring mitral/tufted cells in the rat olfactory bulb. Neuroscience 134, 10691080. doi: 10.1016/j.neuroscience.2005.04.027

72. Elsaesser, R., and Paysan, J. (2007) The sense of smell, its signalling pathways, and the dichotomy of cilia and microvilli in olfactory sensory cells. BMC Neurosci. 8(Suppl. 3):S1. doi: 10.1186/1471-2202-8-S3-S1

73. Hines, M., Kumar, S., and Schrmann, F. (2011). Comparison of neuronal spike exchange methods on a Blue Gene/P supercomputer. Front. Comput. Neurosci. 5:49. doi: 10.3389/fncom.2011.00049

74. Hines, M. L., Markram, H., and Schrmann, F. (2008). Fully implicit parallel simulation of single neurons. J. Comput. Neurosci. 25, 439448. doi: 10.1007/s10827-008-0087-5

75. Hovis, K. R., Padmanabhan, K., and Urban, N. N. (2010). A simple method of in vitro electroporation allows visualization, recording, and calcium imaging of local neuronal circuits. J. Neurosci. Methods 191, 110. doi: 10.1016/j.jneumeth.2010.05.017

76. Igarashi, K. M., Ieki, N., An, M., Yamaguchi, Y., Nagayama, S., Kobayakawa, K., et al. (2012). Parallel mitral and tufted cell pathways route distinct odor information to different targets in the olfactory cortex. J. Neurosci. 32, 79707985. doi: 10.1523/JNEUROSCI.0154-12.2012

77. Junek, S., Kludt, E., Wolf, F., and Schild, D. (2010). Olfactory coding with patterns of response latencies. Neuron 67, 872884. doi: 10.1016/j.neuron.2010.08.005

78. Luo, S. X., Axel, R., and Abbott, L. F. (2010). Generating sparse and selective third-order responses in the olfactory system of the fly. Proc. Natl. Acad. Sci. U.S.A. 107, 1071310718. doi: 10.1073/pnas.1005635107

79. Migliore, M., Cavarretta, F., Hines, M. L., and Shepherd, G. M. (2013) Functional neurology of a brain system: a 3D olfactory bulb model to process natural odorants. Funct. Neurol. 28, 241243. doi: 10.11138/FNeur/2013.28.3.241

80. Migliore, M., Inzirillo, C., and Shepherd, G. M. (2007). Learning mechanism for column formation in the olfactory bulb. Front. Integr. Neurosci. 1:12. doi: 10.3389/neuro.07.012.2007

81. Migliore, M., and Shepherd, G. M. (2008). Dendritic action potentials connect distributed dendrodendritic microcircuits. J. Comput. Neurosci. 24, 207221. doi: 10.1007/s10827-007-0051-9

82. Mori, K., and Takagi, S. F. (1975). Spike generation in the mitral cell dendrite of the rabbit olfactory bulb. Brain Res. 100, 685689. doi: 10.1016/0006-8993(75)90170-5

83. Mori, K., Takahashi, Y. K., Igarashi, K. M., and Yamaguchi, M. (2006). Maps of odorant molecular features in the Mammalian olfactory bulb. Physiol Rev. 86, 409433. doi: 10.1152/physrev.00021.2005

84. Murthy, V. N. (2011). Olfactory maps in the brain. Annu. Rev. Neurosci. 34, 233258. doi: 10.1146/annurev-neuro-061010-113738

85. O'Connor, S., Angelo, K., and Jacob, T. J. (2012). Burst firing versus synchrony in a gap junction connected olfactory bulb mitral cell network model. Front. Comput. Neurosci. 6:75. doi: 10.3389/fncom.2012.00075

86. Rall, W., and Shepherd, G. M. (1968). Theoretical reconstruction of field potentials and dendrodendritic synaptic interactions in olfactory bulb. J. Neurophysiol. 31, 884915.

87. Rall, W., Shepherd, G. M., Reese, T. S., and Brightman, M. W. (1966). Dendrodendritic synaptic pathway for inhibition in the olfactory bulb. Exp Neurol. 14, 4456. doi: 10.1016/0014-4886(66)90023-9

88. Royet, J. P., Souchier, C., Jourdan, F., and Ploye, H. (1988). Morphometric study of the glomerular population in the mouse olfactory bulb: numerical density and size distribution along the rostrocaudal axis. J. Comp. Neurol. 270, 559568. doi: 10.1002/cne.902700409

89. Sholl, D. A. (1953). Dendritic organization in the neurons of the visual and motor cortices of the cat. J. Anat. 87, 387406.

90. Smear, M., Shusterman, R., O'Connor, R., Bozza, T., and Rinberg, D. (2011). Perception of sniff phase in mouse olfaction. Nature 479, 397400. doi: 10.1038/nature10521

91. Soucy, E. R., Albeanu, D. F., Fantana, A. L., Murthy, V. N., and Meister, M. (2009). Precision and diversity in an odor map on the olfactory bulb. Nat. Neurosci. 12, 210220. doi: 10.1038/nn.2262

92. Whitman, M. C., and Greer, C. A. (2007). Synaptic integration of adult-generated olfactory bulb granule cells: basal axodendritic centrifugal input precedes apical dendrodendritic local circuits. J. Neurosci. 27, 99519961. doi: 10.1523/JNEUROSCI.1633-07.2007

93. Wolf, S., Grein, S., and Queisser, G. (2013). Employing NeuGen 2.0 to automatically generate realistic morphologies of hippocampal neurons and neural networks in 3D. Neuroinformatics 11, 137148. doi: 10.1007/s12021-012-9170-1

94. Yu, Y., McTavish, T. S., Hines, M. L., Shepherd, G. M., Valenti, C., and Migliore, M. (2013) Sparse distributed representation of odors in a large-scale olfactory bulb circuit, PLoS Comput Biol. 9:e1003014. doi: 10.1371/journal.pcbi.1003014

95. Zubler, F., and Douglas, R. (2009). A framework for modeling the growth and development of neurons and networks. Front. Comput. Neurosci. 3:25. doi: 10.3389/neuro.10.025.2009.

96. Shepherd GM. (1991). Computational structure of the olfactory system. In: Davis JL, Eichenbaum H, editors. Olfaction: A model system for computational neuroscience. The MIT Press; Cambridge, MA: pp. 341.

97. Girardin CC, Kreissl S, Galizia CG. (2013). Inhibitory connections in the honeybee antennal lobe are spatially patchy. J Neurophysiol. 109(2):332343.

98. Cleland TA. (2014). Construction of odor representations by olfactory bulb microcircuits. Prog Brain Res. 208:177203.

99. Stewart WB, Kauer JS, Shepherd GM. (1979). Functional organization of rat olfactory bulb analysed by the 2-deoxyglucose method. J Comp Neurol. 185(4):715734.

100. Kauer JS, Cinelli AR. (1993). Are there structural and functional modules in the vertebrate olfactory bulb? Microsc Res Tech. 24(2):157167.

101. Lowe G. (2002). Inhibition of backpropagating action potentials in mitral cell secondary dendrites. J Neurophysiol. 88(1):6485.

102. Ghosh K, Sarkar S, Bhaumik K. (2013). A possible mechanism of stochastic resonance in the light of an extra-classical receptive field model of retinal ganglion cells. Biol Cybern. 2009;100(5):351359.

103. Mori, K., Kishi, K., Ojima, H. (1983). Distribution of dendrites of mitral, displaced mitral, tufted, and granule cells in the rabbit olfactory bulb. J Comp Neurol 219:339-355.

104. Orona, E., Rainer, E.C., Scott, J.W. (1984). Dendritic and axonal organization of mitral and tufted cells in the rat olfactory bulb. J Comp Neurol, 226:346-356

105. Cavarretta, F., Marasco, A., Hines, M.L., Shepherd, G.M., and Migliore, M. (2016). Glomerular and Mitral-Granule Cell Microcircuits Coordinate Temporal and Spatial Information Processing in the Olfactory Bulb. Front. Comput. Neurosci. 10:67. doi: 10.3389/fncom.2016.00067

106. Kim, D.H., Chang, A.Y., McTavish, T.S., Patel, H.K., Willhite, D.C. (2012). Center-surround vs. distance-independent lateral connectivity in the olfactory bulb. Front Neural Circuits 6:34. doi: 10.3389/fncir.2012.00034.

107. Alle, H., Roth, A., Geiger, J.R. (2009). Energy-efficient action potentials in hippocampal mossy fibers. Science 325 (5946): 1405-1408.

108. Nagayama S, Enerva A, Fletcher ML, Masurkar AV, Igarashi KM, Mori K, Chen WR. (2010). Differential axonal projection of mitral and tufted cells in the mouse main olfactory system. Front Neural Circuits 4:120.

109. Lopez F, Delgado R, Lopez R, Bacigalupo J, Restrepo D. (2014). Transduction for pheromones in the main olfactory epithelium is mediated by the Ca2+ -activated channel TRPM5. J Neurosci, 34(9):3268-3278.

110. Zhang X, Firestein S. (2002). The olfactory receptor gene superfamily of the mouse. Nat Neurosci 5(2):124-133.

111. Zhou Z, Belluscio L. (2008). Intrabulbar projecting external tufted cells mediate a timing-based mechanism that dynamically gates olfactory bulb output. J Neurosci, 28(40):9920-9928.

112. Zhou Z, Belluscio L. (2012). Coding Odorant Concentration Through Activation Timing Between the Medial and Lateral Olfactory Bulb. Cell Rep, 2(5):1143-1150.

113. Pressler RT, Strowbridge BW. (2006). Blanes cells mediate persistent feedforward inhibition onto granule cells in the olfactory bulb. Neuron, 49(6):889-904.

114. Burton SD, Urban NN. (2015). Rapid Feedforward Inhibition and Asynchronous Excitation Regulate Granule Cell Activity in the Mammalian Main Olfactory Bulb. J Neurosci 35(42):14103-14122.

115. Breton-Provencher V, Bakhshetyan K, Hardy D, Bammann R, Cavarretta F, Snapyan M, Cot D, Migliore M, Saghatelyan A. (2016). Principal cell activity induces spine relocation of adult-born interneurons in the olfactory bulb. Nature Comm.

116. Parsa PV, D'Souza RD, Vijayaraghavan S. (2015). Signaling between periglomerular cells reveals a bimodal role for GABA in modulating glomerular microcircuitry in the olfactory bulb. PNAS, 112(30):9478-9483

117. Doucette W, Gire DH, Whitesell J, Carmean V, Lucero MT, Restrepo D. (2011). Associative cortex features in the first olfactory brain relay station. Neuron, 69(6):1176-87. doi: 10.1016/j.neuron.2011.02.024.

118. Thompson JA, Salcedo E, Restrepo D, Finger TE. (2012). Second-order input to the medial amygdala from olfactory sensory neurons expressing the transduction channel TRPM5. J Comp Neurol. 520(8):1819-30. doi: 10.1002/cne.23015.

119. Codling, E.A., Plank, M.J., Benhamou, S. (2008). Random walk models in biology. J R Soc Interface 5, 813-834 doi:10.1098/rsif.2008.0014.

120. Cuntz, H., Mathy, A., Husser, M. (2012). A scaling law derived from optimal dendritic wiring. Proc Natl Acad Sci U S A. 109(27):11014-8. doi: 10.1073/pnas.1200430109.

121. Scorcioni, R., Polavaram, S., Ascoli, G.A. (2008). L-Measure: a web-accessible tool for the analysis, comparison and search of digital reconstructions of neuronal morphologies. Nat Protoc. 3(5):866-76. doi: 10.1038/nprot.2008.51.

122. Maynard, K.R., Stein, E. (2012). DSCAM contributes to dendrite arborization and spine formation in the developing cerebral cortex. J Neurosci.32(47):16637-50. doi: 10.1523/JNEUROSCI.2811-12.2012.

123. Tadros W, Xu S, Akin O, Yi CH, Shin GJ, Millard SS, Zipursky SL. (2016). Dscam Proteins Direct Dendritic Targeting through Adhesion. Neuron. 89(3):480-93. doi: 10.1016/j.neuron.2015.12.026.

124. Ghosh K, Sarkar S, Bhaumik K. (2009). A possible mechanism of stochastic resonance in the light of an extra-classical receptive field model of retinal ganglion cells. Biol Cybern. 100(5):351359.

125. Shankar KH, Howard MW. A scale-invariant internal representation of time. Neural Comput. 24(1):134193.

126. Si X, Angelaki DE, Dickman JD. Response properties of pigeon otolith afferents to linear acceleration. Exp Brain Res. 117(2):242250.

127. Kim KH, Kim SJ. A wavelet-based method for action potential detection from extracellular neural signal recording with low signal-to-noise ratio. IEEE Trans Biomed Eng. 50(8):9991011.

128. Rospars JP, Lansky P, Chaput M, Duchamp-Viret P. (2008). Competitive and noncompetitive odorant interactions in the early neural coding of odorant mixtures. J Neurosci. 28(10):2659-2666. doi: 10.1523/JNEUROSCI.4670-07.2008.

129. Lnsk P, Rospars JP. (1998). Odorant concentration and receptor potential in olfactory sensory neurons. Biosystems. 48(1-3):131-138.

130. Cruz G, Lowe G. (2013). Neural coding of binary mixtures in a structurally related odorant pair. Sci Rep. 3:1220. doi: 10.1038/srep01220.

131. Michaelis L, Menten ML. (1913). Die Kinetik der Invertinwirkung. Biochem Z. 49:333-369

132. Prinz, H. (2010). Hill coefficients, dose-response curves and allosteric mechanisms. J Chem Biol. 3(1): 37-44. doi: 10.1007/s12154-009-0029-3

133. Seo MH, Park J, Kim E, Hohng S, Kim HS. (2014). Protein conformational dynamics dictate the binding affinity for a ligand. Nat Commun. 5:3724. doi: 10.1038/ncomms4724.

134. Pedersen MG, Bersani AM, Bersani E. (2007). Quasi steady-state approximations in complex intracellular signal transduction networks - a word of caution. J Math Chem 43(4):1318-1344

135. H. Brezis. *Functional Analysis, Sobolev Spaces and Partial Differential Equations*, Universitext, Springer-Verlag New York, pp. XIV-600, 2011.

136. P. Colli. *Mathematical study of a nonlinear neuron multi-dendritic model*, Quart. Appl. Math., vol. 52, n.4, pp. 689–706, 1994.

137. V. Comincioli, D. Funaro, A. Torelli, E. D'Angelo, P. Rossi. *A mathematical model of potential spreading along neuron dendrites of cerebellar granule cells*, Appl. Math. Comput., vol. 59, n.1, pp. 73–87, 1993.

138. J.D. Evans. *Analysis of a multiple equivalent cylinder model with generalized taper*, IMA J. Math. Appl. Med. Biol. 17, pp. 347–377, 2000.

139. L. Lamberti. *Solutions to the Hodgkin-Huxley equations*, Appl. Math. Comput., vol. 18 n.1, pp. 43–70, 1986.

140. M. Mascagni. *An initial-boundary value problem of physiological significance for equations of nerve conduction*, Comm. Pure Appl. Math., vol. 42 n. 2, pp. 213–227, 1989.

141. M. Mascagni. *The backward Euler method for numerical solution of the Hodgkin-Huxley equations of nerve conduction*, SIAM J. Numer. Anal., vol. 27 n. 4, pp. 941–962, 1990.

142. W. Rall. Perspectives on neuron modeling. In M.D. Binder and L.M. Mendell (eds.), *The Segmental Motor System, Oxford University Press, Oxford, pp. 129–149, 1990.*

143. S. Salsa. *Partial Differential Equations in Action*, Universitext, Springer-Verlag New York, pp. XV-556, 2009.

144. H.C. Tuckwell. *Introduction to Theoretical Neurobiology, Volume 1. Linear Cable Theory and Dendritic Structure*. Cambridge University Press, New York, 1988.

Appendix A

The algorithm for generating synthetic neurons

initialize the list L of dendritic extremities that would be grown

for i = 0 to ITERATIONS do
  if length(L) = 0 then
    break
  end if

  for each l in L
    for j = 0 to MAXGROWTHATTEMPTS do
      $\overline{\phi_{i+1}}$, $\overline{\theta_{i+1}}$ = *bias*(p_i, ϕ_i, θ_i)
      $\phi_{i+1} = \overline{\phi_{i+1}} + \Delta\phi$
      $\theta_{i+1} = \overline{\theta_{i+1}} + \Delta\theta$
      $p_{i+1} = xyz(\phi_{i+1}, \theta_{i+1}, p_i)$
      if feasible(p_{i+1}, ϕ_{i+1}, θ_{i+1}) *then*
        l.extends(*p*, ϕ_{i+1}, θ_{i+1})
        break
      end if
    end for

    if l.canBeDeleted() or j > *MAXGROWTHATTEMPTS then*

```
            l.delete()
        else if l.canBifurcate() then
            e1, e2 = l.bifurcate()
            L.append(e1, e2)
            l.delete()
        end if
    end for
end for
```